PhD Thesis

Developing Tools to Optically Map the Functional Connectivity of Neuronal Microcircuits in the Prefrontal Cortex

Navjeevan Singh Soor

Imperial College London, Department of Bioengineering

Supervisors:

Professor Stephen Brickley, Professor Simon Schultz, Professor Mark Neil,
Dr Amanda Foust.

EPSRC
Centre for Doctoral Training in
NEUROTECHNOLOGY
for life and health

ABSTRACT.

This overarching goal of my PhD was to develop optical microscopy tools to study the functional connectivity of neuronal microcircuits. I first conduct dynamic clamp recordings of putative pyramidal neurons in the Prefrontal Cortex to study the effects of intrinsic conductance and synaptic drive of Action Potential (AP) waveform properties. In the set of measured neurons, I find that an increasing, non-linear Goldman-Hodgkin-Katz Cl^- leak conductance or an increasing input AMPA conductance have no effect on AP Full Width, Half Maximum (FWHM). However, I observe that increasing AMPA conductance decreases AP latency and peak voltage. Crucially, the latter has implications on optical functional connectivity assays.

I then develop, characterise, and validate a light patterning microscope for optical functional connectivity assays with single neuron precision. I show reliable generation of photostimulation spots with biologically relevant diameters of 5 ± 0.2 μm and 10 ± 0.2 μm, pulse durations of 2 – 10 ms, errors of 20 ± 10 μs, and latencies of 180 ± 10 μs. I demonstrate lateral spatial confinement of photostimulation spots by photostimulating laterally displaced locations relative to a ChR2 expressing neuron and observing an elimination of photocurrents as the spots move away from the cell soma. I attempt single neuron precision functional mapping between Inter-Telencephalic (IT) and non-IT neurons, finding no evidence of single neuron precision functional connections in the samples tested- but do verify that functional connectivity amongst these populations exists.

Finally, I demonstrate the first reported all-optical, crosstalk-free neurophysiology strategy using Chronos, a blue-light sensitive opsin, and CaSiR-1, a red-light emitting calcium dye. I show red light suitable for CaSiR-1 imaging evokes no photocurrents in CHO cells transfected with Chronos, before demonstrating high signal-to-noise, crosstalk-free imaging of CaSiR-1 red fluorescence whilst photostimulating Chronos in acute brain slices at stimulation frequencies up to 20 Hz.

DECLARATION OF ORIGINALITY.

I, Navjeevan Singh Soor, declare that the work presented in this PhD thesis is my own, and all else is acknowledged and referenced as appropriate.

COPYRIGHT DECLARATION.

The copyright of this thesis rests with the author. Unless otherwise indicated, its contents are licensed under a Creative Commons Attribution-Non Commercial 4.0 International Licence (CC BY-NC).

Under this licence, you may copy and redistribute the material in any medium or format. You may also create and distribute modified versions of the work. This is on the condition that: you credit the author and do not use it, or any derivative works, for a commercial purpose.

When reusing or sharing this work, ensure you make the licence terms clear to others by naming the licence and linking to the licence text. Where a work has been adapted, you should indicate that the work has been changed and describe those changes.

Please seek permission from the copyright holder for uses of this work that are not included in this licence or permitted under UK Copyright Law.

CONTENTS.

LIST OF FIGURES.

LIST OF TABLES.

LIST OF ABBREVIATIONS.

aCSF = artificial Cerebrospinal Fluid

AMPA = α-amino-3-hydroxy-5-methyl-4-isoxazolepropionic acid

AP = Action Potential

CC = Current Clamp

CHO = Chinese Hamster Ovary

ChR2 = Channelrhodopsin-2

DCC = Dynamic Current Clamp

DMD = Digital Micromirror Device

FoV = Field of view

FWHM = Full Width, Half-Maximum

GFP = Green Fluorescent Protein

GHK = Goldman-Hodgkin-Katz

GUI = Graphical User Interface

IR = Infrared

mEPSC = mini Excitatory Post-Synaptic Current

VC = Voltage Clamp

ACKNOWLEDGEMENTS.

"My predominant feeling is one of gratitude."
-Oliver Sacks

To Mathi, your journey spanned 3 continents and 9 decades, but your story is far from over. We'll remember you until the end.

To Mum, for showing me what strength actually means.

To Esh and Avi, for more than can be written.

To Simran and Kiran, for being the most annoying siblings imaginable.

To the Nandos collective, for keeping me grounded.

To Hayden, who helped me keep sight of who I am and who I want to be- even when the days were too dark to see anything.

To the cheesiest flat in existence: Nick and Margs. We survived a pandemic together and I'm sincerely grateful we got to share a home these last few years. Thank you, from the bottom of my heart.

To Sheera, I could fill another thesis for you. Won't do it though- this one took long enough.

To Tunvez: Thank you for standing by me through it all.

To the 25C crew: Rashid, Joel, Sheera. Ahab spent all that time looking for his whale, but we found ours when we stopped for a beer. Who knows what other adventures are out there waiting for us?

Praise to the Cult: Sheera, Biyi, Rachel- to many more trips to the Butts and beyond.

To Adam and Priyank. Priyank, you may not be great at pool but you're great company at least.

To the Dogula folk: Arinder, Harpreet, Bobby, and Anca. Arinder- a jillion days will go by, and I'll still remember to roast you for it.

To Lotte, for being such a great friend. Send my best to Mr. Mistoffelees.

To Kaja, the powerhouse.

To the Din-Dins crew: Nick, Tunvez, Sihao.

To Kate Hobson, for everything you've done for our CDT.

To Martin Holloway, for your kindness and support.

To my CDT cohort: how lucky were we to have shared this journey? Thank you for everything. I'll look back on our times together with great fondness.

To Tom and Marina- we don't see each other nearly as often as we should.

To Sophie, who I will one day get to be my Karate Sensei.

To my lab mates and beyond: Sihao, Florian, Gerry, Phatsimo, Gema, Peter, Aimee, Deyl, and Faith. I sincerely hope to hear of all the great things you go on to do.

To a long string of therapists, psychiatrists, surgeons, and hospital staff: thank you for all of your tireless work keeping my mind and body in one piece. A special shout out to Kei.

To Oliver Sacks, Murakami, Vonnegut, Ted Chiang, Cixin Liu, Ken Liu, Atwood, Stanisław Lem, Camus, and so on.

To the Wolf and Owl.

To my Supervisors, Stephen, Simon, Amanda, and Mark, for your patience and guidance over the years. With a special mention:

To Stephen. Your enthusiasm, kindness, and passion for science kept me here until the finish line. Thank you, sincerely.

The simple truth is that I wouldn't be here if it were not for countless people. Countless opportunities afforded to me, countless hours of support, guidance.

Thank you.

CHAPTER 1

INTRODUCTION

1.1 FOREWORD

Underlying the vast information processing capabilities of the brain are elaborate functional and structural architectures of neuronal networks. If we are to have any hope in understanding how these architectures give rise to computation, cognition, behaviour, thoughts, emotions, or even (at risk of getting too philosophical) our sense of self, it is imperative that we develop our understanding of the principles which govern the construction and behaviour of these networks.

Indeed, when we take a step back and consider the brain one of the first things we can't help but be is humbled by its sheer complexity. Where do we begin? One axis (of many) that we can look at is order of magnitude. We can look at the dizzying array of molecular pathways or transcriptomic and proteomic landscapes. We can look at single neurons, glia. We can start to look at microcircuits of neurons. Maybe how these smaller architectures interact with one another to form larger functional regions. How about how these regions interact with one another across cortical and sub-cortical regions to give rise to even more complex computation and behaviours? and what of the brain's interaction with the world around it? How external stimuli feed in, like David Hume's impressions, to influence the structural and functional architectures we began with? And what about time's effect on all the above? Development, aging? What can the evolutionary history of the brain tell us? Or pathology?

In my view, one of the greatest yet burdensome tools we have on this journey is reductionism. To understand the brain we must reduce it, understand its story at each level of abstraction before we attempt to resynthesise the information and form a coherent view of the whole. Yet paradoxically, we can never lose sight of this 'whole' for fear of losing the forest for the trees.

One lasting lesson of this PhD is the value of being both a bird and a frog. The physicist and mathematician Freeman Dyson once gave a speech for the American Mathematical Society[1] in which he described two kinds of mathematician: frogs, who 'delight in the details of particular objects', and birds who 'delight in concepts that unify our thinking and bring together diverse problems'.

Though speaking of mathematicians, and though it's perhaps a false dichotomy, I do think that there is an element of truth in the above. This PhD was my attempt at adding a few small details to the picture of neuroscience research, while still gliding around for a while, enjoying the landscape from above.

1.2 SCIENTIFIC AND ENGINEERING CONTEXT

The overarching aim of this PhD was to develop and implement optical microscopy tools to study the functional connectivity of neuronal microcircuits. In Section 1.3, I will discuss functional connectivity in the brain at the level of neuronal microcircuits-circuits of 10s to 100s of neurons. In Section 1.4, I will dicuss optical neurophysiology. I will begin with opsins- the light sensitive ion channels being used to optically perturb neural activity- before moving on to optical activity reporting by giving a general overview of voltage and calcium imaging. I will then discuss the optical microscopy tools being developed to fully utilise the optogentic toolkit, before finally moving on to contextualising these three topics in the light of functional connectivity mapping.

1.3 FUNCTIONAL CONNECTIVITY IN NEURONAL MICROCIRCUITS

The functional architectures of neuronal microcircuits contribute to larger scale information processing in the brain[2]. Patch clamp electrophysiology, a gold standard for neuronal activity control and readout in terms of is high spatial precision, high temporal precision, and high signal-to-noise (SNR) readout of activity[3], has elucidated many curious features of these networks. Before discussing this further, I will make a couple of brief detours to put the level of abstraction I focus on in this PhD into perspective: first to structural connectivity, and then to scales of connectivity in the brain.

1.3.1 STRUCTURAL VS. FUNCTIONAL CONNECTIVITY

Structural connectivity is a crucial ingredient to understanding the architectures of neuronal networks[4]. Taking the long view, structural connectivity mapping could be seen to date back to the early 19th century when Cajal conjectured that the brain of a bird was broken down in to discrete units- neurons[5]. Then came the discovery of synapses- connection points between neurons. If neurons share a pair of synapses they are said to be structurally connected. There are various experimental techniques one could use to determine this kind of structural connectivity including electron microscopy[4], GFP reconstitution across synaptic partners (GRASP, or mGRASP for the mammalian nervous system)[6], 2-photon microscopy[7], and trans-synaptic viral tracing[8–10]. However, the presence of synaptic partnering between neurons doesn't necessary imply a functional connection. Not all synapses are functional. In principle, one could map out the entire nervous system in exquisite detail- with nanometre spatial precision afforded by electron microscopy, but we would still be missing crucial information which would help us understand the principles governing information processing in the brain. Though one could infer a functional connection by pinpointing synaptic vesicles in pre-synaptic boutons, this is not necessarily a definitive answer to whether the two neurons are connected. Electron microscopy is an inherently destructive process and takes single temporal snapshots of tissue structure. Hence, an active synapse 'caught' in one moment during and electron microscope image could be non-existent in the hypothetical moments after. The phrasing of this statement is perhaps superlative, but it has been shown that synapses themselves are transient structures which form and disappear with the winds of experience[11].

In reality, structure and function are intertwined concepts when it comes to network connectivity. They are also time, experience[12–15], and pathology[16–18] dependent concepts. It seems evident that one must pair structural and functional assays to understand network behaviour. One can't estimate the strength of a connection, or the change in connectivity without bringing a discussion of functional assays to the table. Indeed, these concepts if connection strength and change are crucial pieces of the puzzle. Similarly, structure clearly plays a role in function- where for instance synapse geometry affects AMPA channel expression[19].

1.3.2 SCALES OF CONNECTIVITY

Considering the brain as a whole, imaging modalities such as Magnetic Resonance Imaging (MRI)[20], Diffusion weighted MRI[21] or Computed Tomography (CT)[22] are able to discern the brain's macrostructure at increasingly high resolutions. Similarly, functional imaging modalities such as functional MRI (fMRI)[23] or Positron Emission Tomography (PET)[24] can elucidate how different cortical and subcortical anatomical regions behave under different conditions, providing and insight in to concepts such as aging[25,26] or pathology[27]. Furthermore, correlating signal in disparate regions using these techniques can begin to paint a picture of the underlying functional connectivity between them, with increasingly sophisticated analytical techniques [28]. However, these modalities, while yielding exquisite detail of neuroanatomy and physiology, are focussed on relatively large regions and not able to give an insight into the underlying structural and functional of neuronal architectures at a cellular resolution. Furthermore, functional measures such as the Blood Oxygen Level Dependent (BOLD) signal arising from fMRI studies or the signal arising from PET scans show a *proxy* of underlying neural activity: they measure blood oxygenation or metabolism, respectively. Hence, this leaves us with the question: what's happening at the neuronal microcircuit level?

Furthermore, though it is out of scope for this thesis I argue that connectivity does not begin and end with the previously mentioned scales. In my view, connectivity extends from subcellular processes and anatomical features to the world at large. The crux of this latter argument stems from the idea that the brain does not exist in isolation; it is constantly barraged with information from the organism's body and environment which are arguably connected to the brain- if not by synapse then by photoreceptors, mechanoreceptors, thermoreceptors and so on. But I digress- back to our level of abstraction.

1.3.3 NEURONAL MICROCIRCUITS IN THE CEREBRAL CORTEX

As we see, the concept of connectivity- be it structural or functional- is a curious one. More so is measuring it. If we now focus on neuronal microcircuits the gold standard methodology for studying the functional connectivity within such networks is patch clamp electrophysiology [3]. It offers a high signal to noise activity readout and control of single neurons- able to capture minute sub-threshold membrane depolarisations and currents, as well as sub millisecond synaptic events. It can also be scaled to multiple recordings to begin charting the shifting functional architectures of neuronal microcircuits [29–31].

Many such studies have detailed functional features in the circuits comprising the sensory and motor cortices with the view of learning the principles governing how these regions process continual flows of information[2,32,33]. As is happens, it seems that there were similar principles which appear across the cortex. For instance, though sensory cortices are made up of diverse cell types, different regions share common types of cells with similar intrinsic properties and functional connectivity motifs[2]. The network topology of microcircuits are non-random[30], with connection probability relying on pre- and post- synaptic cell type[34–36]; functional purpose of the neurons, with neurons similar functions more likely to be functionally connected to one another[37–39]; long range projections[40,41]; or the origin of afferent information streams, with neurons that receive information from similar locations more likely to be connected[34,42]. Patching has also been used to study the principles governing the *change* in functional architectures of neural networks[14,15,43,44]. Such plasticity rules are crucial in our goal of understanding information processing in the brain.

Though patch-clamp electrophysiology has clearly proved to be a highly useful tool in neuroscience, it is not without its shortcomings. Unfortunately, it is very difficult to scale-often paired recording are used with extreme examples having 12 simultaneous recordings. this physical restraint means that often time networks are randomly sampled to gain data (though genetic targeting of fluorescent proteins to guide patching experiments can help to offer cell-class information from recorded neurons), and we can only yield information regarding a handful of neurons at a time. Ultimately, if we would like study the functional architectures of microcircuits with larger scales and throughput, we turn to the photon.

1.4 OPTICAL NEUROPHYSIOLOGY

Optical neurophysology has the potential to revolutionise our understanding of neural network structure and function[45–48]. Neurons can be made to ectopically express light-sensitive ion channels or pumps (opsins) to control their activity[49–51]. Furthermore, they can be synthetically[52] or genetically labelled[53,54] with activity reporters that convert biophysical markers of cellular activity such as changes in intracellular calcium concentration[55,56] or membrane potential[53] into a change in fluorescent signal (paragraph adapted from[57]). Altogether, the optogenetic toolkit allows optical access to 10s – 100s of neurons in concert, with single neuron precision and millisecond temporal resolution. Further, the ability to genetically or functionally target specific neuronal sub-populations yields cell-class, location and structural connectivty information which make optogenetic mapping a promising avenue for for studying the complex functional architectures of neuronal microcircuits not achievable using electrophysiological or large scale imaging methodologies such as fMRI, CT, or EEG.

1.4.4 OPTOGENETICS: PERTURBING NEURONAL ACTIVITY WITH LIGHT

Opsins are light sensitive ion channels or pumps which upon photon absorption undergo a conformational change to allow the passage of ions across the cell membrane. This flow of ions can be comprised of positively or negatively charged ions depending on the opsin, hence opsins can either actuate or silence neuronal activity. Since the first demonstration of single component optogenetics [49], there has been a plethora of opsins both discovered[50,58] and engineered[51,59–62], each with different biophysical properties [50,63]. What're more, the toolkit of opsins is forever growing given the potency of molecular engineering methodologies[64].

1.4.5 OPTICALLY READING OUT NEURONAL ACTIVITY

Optically reporting neural activity relies on converting biophysical markers of cellular activity into a change in fluorescent signal or transmitted light. The two main methods for optically reading out neural activity in contemporary optical neurophysiology experiments are reporting changes in membrane potential or changes in intracellular calcium (Ca^{2+}) concentration.

Optically reporting membrane potential using contemporary synthetic dyes or genetically encoded reporters offers high temporal resolution readout of relative changes in voltage, though the signal to noise ratio (SNR) obtained is often low[53]- with newer reporters showing marked improvement in these areas[65,66]. Many voltage reporters also suffer from large amounts of photobleaching and can be toxic to their host cells. In addition, voltage reporters are localised to the cell membrane. As such, this results in lower SNR relative to Ca^{2+} imaging which can integrate signal from the neuron's intracellular volume where the calcium reporter resides. Furthermore, membrane localisation of reporter molecules can make disentangling signals from neighbouring cells impossible given the densely packed nature of neural networks (however, this can be partially solved by sparse labelling of cells, or precise light patterning on to the sample). Finally, the optical systems used in conjunction with the reporters must be capable of imaging fast enough to be able to make use of the temporal fidelity of the reporter. New voltage reporters are being developed to overcome many of these issues[65,67] though as yet, they are still difficult to implement experimentally.

Calcium reporters offer an attractive alternative to the voltage reporters. They have a high SNR relative to voltage reporters, though they offer a much lower temporal precision readout of activity. This is due to the kinetics of the reporters themselves, as well as the buffering of calcium in the host cell. Mechanistically, calcium reporters chelate calcium as it enters a cell following an action potential. This leads to a change in fluorescent signal when the cell fires an action potential. Their dissociation constant, k_d, determines the binding strength of the calcium which in turn determines the temporal precision of the activity reporter and SNR. Though calcium reporters offer less information about the cellular activity (the presence of action potential(s) as opposed to any sub-threshold activity discernible by voltage reporters) they are significantly easier to implement in experimental neuroscience and are still powerful tools in studying neural networks. Hence, this project will focus primarily on using calcium reporters. To close the loop and enable causative studies of neural networks, these reporters can be paired with opsins which can actuate transmembrane currents in targeted neurons.

1.4.6 OPTICAL MICROSCOPY TOOLS FOR OPTOGENETICS: A GENERAL OVERVIEW

Optical microscopy systems are rapidly being developed which can fully utilise the optogenetic tool kit. To realise the potential of optical neurophysiology experiments in studying the functional connectivity neural networks, such systems must be able to deploy light or correct wavelengths efficiently and selectively on to neurons to actuate the activity of 10s to 100s of neurons with single cell spatial resolution, and millisecond temporal precision with the view of orchestrating naturalistic neural activity with light. Furthermore, if an all-optical strategy is required, these systems must be able to simultaneously readout neural activity at sampling rates equivalent to or greater than the Nyquist rate to avoid aliasing of sub-millisecond neural activity. The Nyquist rate is defined as a sampling frequency which is twice the highest frequency within the sampled signal. It should be noted that these systems would need to be paired with reporters which can effectively convert fast neural activity in to fast optical signals with sufficient signal-to-noise: in other words, voltage imaging.

There are three primary strategies of deploying light on to neurons to actuate or report their activity[68–70]. The first is single photon (1P), widefield illumination. This method can actuate neurons with high temporal resolution though lacks spatial precision as it illuminates all cells within the field-of-view simultaneously. Furthermore, widefield illumination has no optical sectioning capabilities as the light extends throughout the volume of targeted tissue. This low spatial resolution can be mitigated by genetically targeting opsins or activity reporters to specific cell types[53,54]. However, this method lacks the ability to illuminate sequences of neurons with spatiotemporal patterns which mimic natural activity, and moreover the broad illumination of the sample together with the scattering properties of brain tissue[71] leads to a large background fluorescent signal due to broad activation of reporter fluorophores. Alternatively, 2 Photon (2P) point scanning has a high spatial precision due to two reasons. Firstly, 2P absorption is dependent on the square of the illumination intensity, thus confining 2P excitation to a femtolitre volume[72]. Secondly, the near-infrared wavelengths used in 2P illumination are more robust to scattering than the shorter wavelengths used in single-photon widefield illumination, increasing the depth at which neurons can be stimulated[71]. Unfortunately, this high spatial precision comes at the cost of temporal precision as the 2P excitation volume must be scanned over each individual target neuron to either summate sufficient opsin-induced membrane current to generate action potentials or excite sufficient reporter fluorescence to gain a detectable activity readout signal. However, this is not the end of the story for 2P illumination, as we will see shortly.

The third illumination strategy is to shape light over the brain tissue. This can be achieved in two ways. The first is to modulate the amplitude of the illumination wavefront, for example with a Digital Micromirror Device (DMD)[73] or micro Light Emitting Diode (LED) array[74]. This can increase the lateral spatial resolution of 1P illumination strategies by only illuminating the sample plane in areas dictated by the DMD or micro-LED array. With the case of the DMD, illumination light is cast onto the micromirror array which itself relays the light down to the sample plane by adjusted the pitch or yaw of each individual micromirror. In this way, defined subsets of the entire array can be cast light down to the sample plane- effectively illuminating defined areas of the sample. However, this does not improve the optical sectioning or axial confinement of 1P illumination and in the case of the DMD is inefficient as it 'throws away' light which limits the number of neurons which can be illuminated in parallel.

To return to 2P illumination, the second method of patterning light on to a sample is to modulate the phase of a coherent light source- which is the basis for Computer Generated Holography (CGH) and Generalised Phase Contrast (GPC)[75]. Both light patterning methods have been previously reviewed[68,69,76] though CGH is most flexible in terms of spatial patterning and amplitude modulation. In brief, a Spatial Light Modulator (SLM) imposes a computed phase mask on to the wavefront of a laser beam[77], which is then conjugated to the back aperture of the microscope objective. This produces a custom amplitude pattern at the sample plane of the microscope via the Fourier transform properties of the objective[78].

CGH can sculpt light to target specific subsets of neurons in the microscope Field of View (FOV) with high spatial precision, especially in 2P excitation mode. However, the axial confinement of a CGH illumination pattern increases with lateral pattern size[79]. This can be remedied by the implementation of temporal focussing (TF), which disperses the spectral components of an ultrashort laser pulse and refocuses them at the focal plane of the microscope[80,81]. This increases the axial confinement and optical sectioning of the illumination pattern, as demonstrated by[79] who achieved an axial confinement of 3 µm and stimulation depths up to 250 µm- which for most slice experiments encompasses the entire usable axial depth of tissue when we discount the first dozen or so microns on the top and bottom of the slices which are usually damaged from the slicing procedure.

A further and more recent improvement of CGH for optogenetics is graded intensity holograms[82]. Importantly, this method allows the relative intensity of the illumination pattern to be adjusted per target neuron, compensating for the variable expression of opsin (or activity reporter) between cells. Furthermore, though TF-CGH primarily patterns light in 2D, recently developed systems have demonstrated the generation of 3D photostimulation patterns[83–90]. These systems are capable of high spatial precision activation of neurons in a volume of tissue[90] and could theoretically be used to excite fluorescent signals from activity reporters. Ultimately, no matter how fanciful or elaborate the optical system, the spatial resolution and temporal precision of neuronal activation or activity readout depends critically on the choice of opsin and activity reporter. Furthermore, though phase modulation of a coherent light source combined with 2P illumination light could prove a potent tool in experimental neuroscience, they have a higher 'entry-fee' to the experimental arena when we consider the cost of the high repetition rate, high average-power and pulse-energy lasers required for 2P illumination, as well as the relative experimental complexity when put next to amplitude modulation strategies.

1.5 FUNCTIONAL CONNECTIVITY MAPPING: FROM ELECTRONS TO PHOTONS

Returning to the general aim of this of this PhD- optically mapping the functional connectivity of neuronal microcircuits- I will now discuss the current methodologies of optical functional mapping in literature before moving on to my own strategy for the thesis. Broadly speaking, we can split the idea of optical mapping in to two sections: neurotransmitter uncaging and optogenetics.

1.5.7 NEUROTRANSMITTER UNCAGING

Neurotransmitter uncaging entails the photolysis of 'caged' compounds, which are essentially neurotransmitter molecules that are bound via a photo-scissile bond to a caging moiety. Upon photon absorption the neurotransmitter is released from the moiety and left to interact with endogenous receptors in the tissue preparation. In this way, one can illuminate a sample infused with these bound neurotransmitters, and lookout for downstream effects of the released neurotransmitter; neurons within the vicinity of the uncaged neurotransmitter would in principle be stimulated to fire APs, which means that any functionally connected neurons downstream would consequentially exhibit Excitatory Post-Synaptic Currents (EPSCs) or APs due to afferent connections from the stimulated cells. Thus, by readout the activity of these downstream neurons one can build an image of the functional architecture of neuronal networks[91]. The resolution of such paradigms is limited by the Point Spread Function (PSF) of the photostimulation light- that is, the response of an optical system to a point source of light, or intuitively how blurred or spread the image of a point source becomes when using the particular imaging system. Using a 1P illumination strategy, inter- laminar functional connectivity in the cortex can be assayed[92–95], as well as the functional connectivity between distinct cytoarchitectural regions of the cortex[96]. The approach can further be combined with 2P scanning or patterned illumination to gain higher levels of spatial precision and anatomical specificity of photostimulation steps.

However, neurotransmitter uncaging does carry with it certain drawbacks. In principle, any neuron(s) within the vicinity of release with complementary receptors to the neurotransmitter would be stimulated, making any precise knowledge of pre-synaptic neurons difficult to ascertain. Further, the spatial resolution is limited in the sense that if the post-synaptic neuron has complementary receptors within the vicinity of illumination, this could create a confounding, large response which could dilute the signal. On balance, once can achieve knowledge of postsynaptic neurons- altogether showing that neurotransmitter uncaging can yield a good knowledge of the distribution of functional connections between different areas of a circuit, though precludes single neuron precision maps.

1.5.8 OPTOGENETIC STIMULATION

Optogenetic mapping is similar to neurotransmitter uncaging, but instead relies on photostimulating neurons expressing opsin and looking out for subsequent downstream responses in the network. This approach utilises 1P widefield or light patterning illumination, as well as 2P scanning methodologies for even greater spatial precision and anatomical specificity of photostimulation. Generally speaking, moving in this direction of illumination strategy increases experimental complexity – as discussed in Section 1.4.3.

For the functional mapping experiments of this PhD, I aimed use a DMD to pattern 1P illumination light over an opsin expressing sample to get single cell resolution functional maps. As discussed, it is a relatively easy to implement strategy, providing one can account for the lack of axial confinement. The particular animal model and scientific context to these mapping experiments will be discussed in more detail in Sections 5.2.1-2, and is a promising model for the proposed methodology. I will combine this light patterning optogenetic approach with patch clamp electrophysiology to report the activity of the post-synaptic neurons, as this affords a high-resolution readout of subthreshold activity.

CHAPTER 2

MATERIALS AND METHODS

Note: this chapter contains a compilation of materials and methods used throughout my PhD. Whilst many items are included, the majority of experimental methodologies pertinent to individual chapters are not included- these are instead detailed in the relevant chapters for ease of reference.

2.1 ANIMALS

All animal experiments were performed under institutional guidelines, were approved by the United Kingdom (UK) Home Office and were in accordance with the UK Animals (Scientific Procedures) Act of 1986 and associated guidelines.

Animals used for Chapters 3, 4, and 5 were female C57BL/6 mice ordered from Charles River. The requested ages were 3-4 weeks postnatal; this was the youngest age we could order, and precise ages were not available to us. These animals were either experimented on as wild-type models, or virally injected to express ChR2-GFP in Inter-Telencephalic (IT) neurons (methodology detailed in section 2.2.1). Animals used in Chapter 6 were triple transgenic mice- the details of which are detailed in Section 2.2.2, transgenic methods.

2.1.1 ANIMAL CARE

All animals were housed in cages on a reverse day/night cycle prior to experimentation. Animal wellbeing was constantly monitored and kept in line with Home Office regulation. For mice in Chapters 3, 4, and 5 animals were handled in the weeks prior to being sacrificed. This acclimatised them to me picking them up, with the rationale that this would decrease animal stress at the point of sacrifice which would in turn maximise animal welfare and improve slice quality. Handling here refers to me leaving my hand in the cage and allowing the mice to gradually get used to me, at which point I would hold them for a minute or two just above the cage to ensure they could safely drop back in if they wanted.

2.2 TRANSGENIC STRATEGIES

This PhD utilised two transgenic strategies for expressing opsin in neurons. The first was unilateral stereotaxic retroviral injections into Prefrontal Cortex of C57BL/6 mice to express ChR2-GFP in Inter-Telencephalic (IT) neurons, and the second was via a triple transgenic mouse line to express Chronos-GFP in cortical excitatory neurons.

2.2.1 CHR2 EXPRESSION STRATEGY AND STEREOTAXIC VIRAL INJECTIONS

To express ChR2 in IT neurons in the PFC, we injected a retrovirus containing a ChR2-GFP payload unilaterally in to the PFC of wild type, C57BL/6 mice (further animal information discussed in section 2.1). Retroviruses travel retrogradely from axon terminals to cell bodies, hence unilateral injection in the PFC would transfect IT neurons in the contralateral hemisphere relative to the injection site- as well as any other neurons which have axons terminals in the vicinity of the injection site.

The specific viral construct utilised was pAAV-Syn-ChR2(H134R)-GFP (Addgene), and the injection coordinates were ML 0.33, AP 2.10, DV -2.13 (mediolateral, anterior-posterior, and dorsal-ventral respectively). All coordinates were relative to the bregma point of the particular animal undergoing surgery. Mice were typically injected 2-4 weeks post-natal, with precise ages unknown due to this information being unknown from the supplier. Animals were sacrificed for experiments minimally 2 weeks following injections to ensure sufficient time for opsin expression. Please note, injection surgeries were carried out by Dr Yu Liu with my assistance where possible.

2.2.2 CHRONOS EXPRESSION USING A TRIPLE TRANSGENIC MOUSE LINE

A triple transgenic mouse line (Ai90[TITL-Chronos]-D/Camk2a-tTA/Rasgrf2- 2A-dCre [54] was used to broadly express Chronos-GFP in L2/3 excitatory cortical neurons. Mouse breeding and genotyping was carried out by Dr Yu Liu. Intrapleural (IP) injections of Trimethoprim (T7883, Sigma) were made minimally two weeks prior to animal sacrifice and experimentation to drive stabilise the dCRE and drive robust expression of Chronos.

2.3 SOLUTIONS

This section outlines the various solutions used for tissue preparation and electrophysiology experiments. Note, during specific experiments in Chapter 5, pharmacological additions were made to intracellular and aCSF solutions; for ease of reference, these changes are noted – both in terms of rationale of use and precise experimental protocol- in the Section 5.3.

2.3.1 INTRACELLULAR SOLUTIONS

Data from Chapters 3, 4, and 5 used either a K-Gluconate based internal solution or a Caesium Chloride based solution. The compositions (in mM) were as follows:

K-Gluconate intracellular solution:

K-gluconate	145
NaCl	4
$CaCl_2$	0.5
HEPES	10
EGTA	5
MG-ATP	4
Na-GTP	0.3

Table 2-1 *K-Gluconate based internal solution in mM*

The pH was adjusted to 7.3 using a 1M KOH solution, and osmolarity was checked to ensure it was within 270 - 280 mOsm/kg. This solution was used for both voltage and current clamp recordings.

Caesium Chloride intracellular solution:

CsCl	140
NaCl	4
$CaCl_2$	0.5
HEPES	10
EGTA	5
MG-ATP	2

Table 2-2 *Caesium Chloride based internal solution in mM*

The pH was adjusted to 7.3 using a 1M CsOH solution, and osmolarity was checked to ensure it was within 270 - 280 mOsm/kg. This solution was used for voltage clamp recordings. Internal solution was made in 50 ml batches, aliquoted into 1 ml vials, and frozen ahead of experiments.

CHO cell K-Gluconate intracellular solution:

Chapter 6 used a K-Gluconate based solution optimised for Chinese Hamster Ovary (CHO) cell electrophysiology.

K-gluconate	150
$MgCl_2$	2
HEPES	5
EGTA	*1.1*

Table 2-3 *CHO cell K-Gluconate based internal solution in mM*

The pH was adjusted to 7.3 using a 1M KOH solution, and osmolarity was adjusted to 290 mOsm/kg. This solution was used for both voltage and current clamp recordings of CHO cells.

2.3.2 ACSF SOLUTIONS

The composition of artificial cerebrospinal fluid (aCSF) used for chapters 3, 4, and 5 s shown table 2-4. aCSF was made fresh on the morning of each experiment and oxygenated by bubbling it with 95% O2/ 5% CO2 gas for a minimum of half an hour before use. The osmolarity was checked to ensure it was between 290 - 310 mOsm/kg.

NaCl	125
KCl	2.5
$CaCl_2$	2
$MgCl_2$	1
NaH_2PO_4	1.25
$NaHCO_3$	26
Glucose	11

Table 2-4 *aCSF composition in mM, for chapters 3, 4, and 5.*

The composition of artificial Cerebrospinal Fluid (aCSF) used for Chapter 6 was (in mM):

NaCl	125
KCl	2.5
$CaCl_2$	2
$MgCl_2$	2
NaH_2PO_4	1.25
$NaHCO_3$	25
Glucose	20

Table 2-5 *aCSF composition in mM, for chapter 6.*

Once again, aCSF was made fresh on the morning of each experiment and oxygenated by bubbling it with 95% O_2/ 5% CO_2 gas for a minimum of half an hour before use. The osmolarity was checked to ensure it was between 300 - 310 mOsm/kg, and the pH buffered to 7.3-7.4 using 1 M NaOH.

2.3.3 NMDG SOLUTIONS

The N-Methyl-D-glucamine (NMDG) slicing solution used for chapters 3, 4, and 5 was comprised of the following (in mM):

NMDG	92
KCl	2.5
NaH_2PO_4	1.25
$NaHCO_3$	30
HEPES	20
Glucose	25
Thiourea	2
Na-Ascorbate	5
Na-Pyruvate	3
$CaCl_2$	0.5
$MgSO_4$	10

Table 2-6 *N-Methyl-D-glucamine (NMDG) slicing solution composition in mM, chapters 3, 4, and 5.*

The osmolarity was checked to ensure it was between 290 mOsm – 310 mOsm. Ideally it would match the aCSF solution used to minimise the shock to brain tissue when transferring between solutions. Finally, the solution was kept ice cold when used and bubbled with 95% O2/ 5% CO2 gas for a minimum of half an hour before use.

The N-Methyl-D-glucamine (NMDG) slicing solution used for chapter 6 was comprised of the following (in mM):

NMDG	110
KCl	2.5
NaH_2PO_4	1.2
$NaHCO_3$	25
Glucose	25
$CaCl_2$	0.5
$MgCl_2$	10

Table 2-7 *N-Methyl-D-glucamine (NMDG) slicing solution composition in mM, chapter 6.*

The osmolarity was checked to ensure it was between 300 mOsm – 310 mOsm.

All NMDG solutions were used experimentally at most 2 days after they were made. Their pH was carefully adjusted to between 7.3 – 7.4 with 5 M HCl solution.

2.3.4 EXTRACELLULAR SOLUTION FOR CHINESE HAMSTER OVARY (CHO) CELL ELECTROPHYSIOLOGY

The composition of extracellular solution used for Chinese Hamster Ovary (CHO) cell electrophysiology in Chapters 6 was (in mM):

NaCl	140
KCl	5
$CaCl_2$	10
$MgCl_2$	2
NaH_2PO_4	0.3
$NaHCO_3$	4
KH_2PO_4	0.4
Glucose	5
HEPES	5

Table 2-8 *Extracellular solution composition in mM for CHO cell electrophysiology, chapter 6.*

The solution was made fresh the beginning of the experiment week and replaced every week. The osmolarity was checked to ensure it was between 300 - 310 mOsm/kg using a 1 M sucrose solution; the pH was adjusted to 7.3 ±0.01 with 1 M KOH solution.

2.4 TISSUE PREPARATION

This section describes the different Tissue preparation strategies used throughout this PhD. Broadly speaking, the protective recovery method [97,98] was adapted in some capacity to maximise neuronal cell health at point of experiment. This is true for all tissue slice preparation methodologies described below.

Chapters 3, 4, and 5:

On the day of experiment, ice cold NMDG solution (section 2.2.4) and room temperature (aCSF section 2.2.3) would be bubbled with 95% O_2/ 5% CO_2 gas for a minimum of half an hour before animal sacrifice. Two slice chambers were then prepared: one for resting the slices immediately after dissection, and the second for resting the slices for the time before experimentation. The former chamber contained NMDG solution warmed to 37°C, and the second contained room temperature aCSF. Both chambers were constantly bubbled with 95% O_2/ 5% CO_2 gas to ensure maximum oxygen saturation of both solutions.

Mice were then sacrificed via cervical dislocation, followed by immediate decapitation in accordance with UK Home Office guidance. The brain was rapidly removed and immersed in oxygenated, ice cold NMDG solution. A coronal dissection was made to remove the caudal end of the brain- including the cerebellum. This side was then glued to the slicing chamber and immersed in fresh oxygenated ice-cold NMDG. This chamber was then placed within the vibratome live tissue slicer (Campden Instruments) for sectioning. As we were primarily focussed on PFC slices for this project, we sliced 3-5 coronal sections from the rostral end of brain (not including the olfactory bulb); slices were 300 µm thick, and the quantity of slices would depend on dissection quality.

After each slice was produced, it was carefully placed within the first resting chamber as described above. Each slice remained in this chamber for 12 minutes, before being transferred to the second aCSF containing chamber for a minimum of 45 minutes before experimentation.

Chapter 6:

Mice were anaesthetised with isofluorane and decapitated in accordance with Home Office guidelines. The brain was immediately removed and placed into ice-cold aCSF (section 2.2.3). I then prepared 400 µm coronal brain slices with a Microtome 7000 (Campden Instruments) whilst the brain was immersed in ice-cold aCSF. Once produced, brain slices were placed into NMDG solution (section 2.2.4) heated to 39°C for a 12-minute recovery period. The slices were then placed back into aCSF of the same composition of that used during slicing for a 1-hour resting period before experimentation. All solutions were constantly bubbled with 95% O_2/ 5% CO_2 gas to ensure maximum oxygen saturation. Note, tissue slicing for this chapter was done in the dark to minimise excitotoxity to neurons; Chronos is a highly light-sensitive opsin variant and as such we took efforts to mitigate the effects of ambient light actuating any superfluous photocurrents. We used red LED torches to see what we were doing as Chronos is not sensitive to these wavelengths.

2.5 ELECTROPHYSIOLOGICAL RECORDINGS

This section details the various methods used for slice and cell electrophysiology over the course of this PhD.

2.5.1 WHOLE-CELL RECORDINGS IN ACUTE BRAIN SLICES

Chapters 3, 4, and 5:

Acute coronal brain slices were placed in the recording chamber of the microscope and held in place using a platinum iridium slice harp. The harp strings were made of nylon threads. Slices were continually perfused with room temperature aCSF which was constantly being oxygenated with 95% O_2/ 5% CO_2 gas. Slices were visualised using our fixed-stage upright microscope (BX51W1, Olympus and Scientifica SliceScope, described fully in section 4.2.2). Navigating using the Allen Brain atlas and neuron morphology, I targeted putative L5 pyramidal neurons for electrophysiological recordings as these were to be the primary targets for functional connectivity mapping paradigms. A 4x magnification was first used to navigate to the approximate anatomical region, and a 40x magnification was then used to resolve individual neurons.

Once target neurons were identified, a patch pipette filled with a K-gluconate or Caesium Chloride based internal solution (current and voltage clamp experiments, respectively; described in section 2.2.2) was used to obtain whole-cell recordings of the neuron. Membrane potential and current was measured using a CV-7B head stage (Axon Instruments) attached to a Multiclamp 700B amplifier (Molecular Devices). They were then digitised using a Power1401 digitiser (Cambridge Electronic Design) sampling at 50 kHz, and controlled using Signal (V6.05b, Cambridge Electronic Design). This set up was suitable for current clamp, dynamic current clamp, and voltage clamp experiments.

Patch pipettes were pulled from borosilicate glass capillaries (0.86 mm internal diameter, 1.5 mm outer diameter, Harvard Apparatus) using a vertical heated filament puller (PC-10, Narishige). Pipette resistances when filled with internal solution were between 6 – 8 MOhm; this was generally observed to be the range at which successful recordings were made for the L5 pyramidal neurons. Higher or lower resistances often yielded large leak currents or low break-in success, respectively.

To break into the cell membrane after achieving a giga-seal, 10 mV stepping voltages were imposed on the neuron whilst in voltage clamp. Negative pressure was applied until the recording 'broke in', as noted when the indicative capacitance transients were seen on the recording.

Current Clamp recordings were made whilst injecting zero current into the patched neuron; if the resting membrane potential was not within physiological ranges (-50 mV to -80 mV), the recording was thrown away. The same is true for dynamic current clamp recordings.

Voltage Clamp recordings were made by holding the resting membrane potential at -70 mV, and sometimes lightly adjusted to minimise the leak current. However, the holding potential was always kept within physiological ranges as stated above.

All recordings were made at room temperature, and no treatment of liquid junction potentials were made.

2.5.2 CHINESE HAMSTER OVARY (CHO) CELL ELECTROPHYSIOLOGY

Once cultured and transfected, GHF positive Chinese Hamster Ovary (CHO) cells were whole-cell voltage- clamped using a Multiclamp 700B amplifier (Axon Instruments, Molecular Devices). Membrane currents were digitised with a Power1401 (Cambridge Electronic Design) at a sampling rate of 40 kHz and controlled by Spike2 software (V5, Cambridge Electronic Design).

Coverslips with adhered transfected cells were bathed at room temperature in an external solution (section 2.2.5). The patch pipette was filled with an artificial intracellular solution (section 2.2.3).

Patch pipettes were pulled from glass capillaries (PG10150-4, World Precision Instruments) to tips with resistances between 4 - 8 MOhm. Voltage was clamped at -40 mV. Cells with leak currents of a magnitude greater than 100 pA were excluded from the analysis. The access and input resistances were monitored between photostimulation epochs to ensure recordings remained healthy.

CHAPTER 3

INVESTIGATING THE EFFECTS OF NON-LINEAR LEAK CONDUCTANCES AND AMPA CONDUCTANCES ON ACTION POTENTIAL PROPERTIES

3.1 ABSTRACT

Action Potential (AP) properties such as AP height, Full Width Half-Maximum (FWHM), and Latency to spike following synaptic input are heterogenous properties within and across neurons. A factor affecting these properties is input conductance. Together, these variables have implications on larger scale information processing in the brain, as well as processes such as aging and pathology. Crucially, in the context of functional connectivity mapping paradigms these AP properties could be confounding variables for connectivity metrics.

This chapter sought to experimentally investigate the effects of realistic AMPA conductances and non-linear GHK (Cl^-) leak conductances on AP properties using the Dynamic Current Clamp (DCC) method. The former has implications on functional connectivity mapping paradigms- specifically how synaptic drive on to a pre-synaptic neuron could affect post-synaptic response.

I first show that recording quality, as measured by series resistance, has little to no correlation with AP latency, peak, or FWHM across a range of resistances from 12 – 50 MOhm- with Spearman's Correlation Coefficient values of 0.433, -0.354, 0.395 respectively. This discounted the recording quality as a confounding variable for further measurements of AP properties.

Next, I show that the AP FWHM is not affected by increasing the maximum AMPA conductance or non-linear GHK leak current. In the same set of neurons, I show that increasing the maximum AMPA conductance decreases the AP latency and AP height. Crucially, the latter findings suggest implications for optogenetic functional connectivity mapping paradigms and provided insights into future experimental plans. Specifically, these data suggested that given the intrinsic variability of opsin expression, one must be mindful of photostimulation paradigms when attempting optogenetic functional mapping; variable charge-transfer responses (analogous to the variable AMPA conductances) from opsin expressing neurons could result in variable AP responses, which could have knock-on effects on functional connectivity metrics.

3.2 INTRODUCTION

In this introduction, I first discuss how Action Potential (AP) properties are affected by intrinsic conductance properties of neurons. I then discuss how synaptic drive can affect these same properties, and then as a consequence how both of these factors can affect information processing at a network level. Next, I detail two such conductances: non-linear GHK leak conductances and AMPA conductances which are the experimental focus of this chapter and examples of intrinsic and synaptic drive conductances respectively. Intrinsic conductances are conductances which arise from the neuron's own physiology, whereas synaptic drive conductances are those which arise as a response to a synaptic event (e.g., an AMPA release from a functionally connected neuron). I finally introduce the Dynamic Current Clamp (DCC) method before detailing the specific chapter aims.

3.2.1 THE ACTION POTENTIAL (AP)

Intrinsic neuronal conductance properties

Action Potential (AP) properties such as AP height, Full Width Half-Maximum (FWHM), and Latency to spike following synaptic input are heterogenous properties within and across neuronal subtypes. Relative to the two voltage-dependent conductances underlying the AP of a giant squid axon, mammalian neurons express multiple flavours of sodium currents, voltage-dependent calcium and potassium currents, and a range of other conductances which contribute to an AP waveform[99].

Though the AP of a squid axon serves a different function to that of mammalian neuron soma, when we consider the above point alongside the fact that the squid axon is a relatively poor encoder of information only able to fire under a narrow range of input frequencies[100], it is not a surprise that mammalian neuron soma have a far larger repertoire of AP behaviour and hence information processing capabilities. If we consider the time, activity, and pathology varying expression of different conductances, we start to question how the shifting conductance landscapes of individual neurons affect information processing at the individual neuron and network level- and vice-versa.

Synaptic drive

Synaptic drive has also been shown to affect AP properties. The intrinsic conductances underlying an AP (for instance, the transient voltage-dependent sodium current and potassium currents) are liable to inactivation following sub- or supra- threshold voltages. Consequently, the membrane voltage preceding a spike- which is itself affected by synaptic drive- significantly alter AP properties such as height and FWHM in layer 2/3 pyramidal neurons [101].

Furthermore, it has been shown that the membrane potential and spiking activity of a neuron in time windows prior to a measured AP has an effect on the measured AP's properties. For instance, somatic AP waveforms in pyramidal neurons are markedly affected by spiking activity within a time window of 50 ms prior to the measured AP, suggesting a short term encoding of information within a neuron's AP waveform[102]. Similarly, fast rates of membrane potential change in hippocampal neurons prior to an AP yields a relatively hyperpolarised AP threshold, whilst a spiking activity in the same neurons 1 s prior to the measured AP yields a relatively depolarised AP threshold [103].

Altogether, the variability in AP waveforms discussed above suggest that within a single neuron, the intrinsic excitability and synaptic drive can both contribute to some form of information processing. This becomes even more interesting when we consider the variability and change in both intrinsic excitability and synaptic drive given time, activity, and pathology- but even more so when we remember the neuron doesn't exist in isolation; there are downstream consequences of AP waveform variability.

Synaptic transmission and connectivity metrics

Synaptic transmission is affected by the presynaptic AP voltage [99,104]. Studies of the Calyx of Held, a large synapse in the auditory cortex in mammalian nervous systems, have shown multiple dependencies of synaptic transmission on AP waveform. First, voltage-gated Ca^{2+} channels are activated with high efficiency by APs [105], the waveforms of which dictate the timing of Ca^{2+} flux dependent on voltage-gated Na^+ and K^+ channels[106]. Further, it was seen that the broader the AP waveform (measured by it's FWHM), the larger the Ca^{2+} influx[107]. Indeed, this broadening evokes highly sensitive changes in neurotransmitter release; it was seen that a 30% increase in AP width lead to a 190% increase in postsynaptic current[108]. Interestingly, it has been shown that different subtypes of voltage-gate K^+ channels seem to serve the purpose of modulating the presynaptic AP, likely with the purpose of regulating synaptic release [109].

Altogether, though one should note that these were studies of a specific synapse of the mammalian nervous system, it seems reasonable to view synaptic transmission as a process which is highly dependent on presynaptic AP waveforms. What's more, the dependence on postsynaptic response on presynaptic AP waveform is one which could likely be propagated throughout a network: a wide AP in the presynaptic neuron could evoke a large depolarising current in the post synaptic neuron, which in turn could evoke a slower or larger magnitude AP waveform and so on. Though it is unclear how big the downstream effects are, it is still something to bear in mind.

In the context of my project, this is an important consideration. Photostimulating neurons generates large depolarising currents- often without being quantified experimentally. The consequence of this- together with what we have discussed on the effects of synaptic drive on AP waveform- indicates that for functional connectivity mapping paradigms which rely on synaptic transmission and post-synaptic current readouts, one should be mindful that photostimulation could itself prove to be a confounding variable for functional connectivity assays. The variable nature of opsin expression and photocurrent response could have a tangible effect on functional response timings and magnitudes in the post-synaptic neurons, thereby biasing metrics of functional connectivity.

In this chapter, I sought to determine the effects of a particular intrinsic conductance and synaptic drive on AP waveform properties. The intrinsic conductance I tested was a non-linear Goldman-Hodgkin-Katz (GHK) leak conductance, which could in theory alter AP FWHM. The synaptic drive I sought to test was a naturalistic AMPA conductance. This latter conductance was chosen as it would provide insight into how charge transfer over the course of a synaptic event could affect AP waveform properties. This measure could then be compared to ChR2 mediated photocurrents to gain and insight in to how photostimulation could affect AP waveforms and hence, connectivity metrics.

3.2.2 DYNAMIC CURRENT CLAMP (DCC)

To study the effects of biophysically realistic conductances on neuronal physiology, I utilised the whole-cell Dynamic Current Clamp method[110,111] (DCC). It is a variant of the regular Current Clamp (CC) method, but with the added functionality of injecting voltage dependent currents in to the current-clamped neuron. It achieves this via rapid sampling of the membrane voltage (typically at rates of 50 kHz or more), the information of which it utilises to impose a voltage-dependent feedback conductance. These conductances can follow a large range mathematical models and hence the utility of this method is clear; one can mimic and impose biophysically realistic conductances on neurons (or any cell recording) which regular CC cannot achieve. For instance, DCC has been shown to make HEK-293 cells ‘spike’ by modelling a voltage-gated sodium conductance on the cells[112], alongside recombinant expression of TREK-1 and TASK-3 potassium channels which generate a hyperpolarising leak current. Remarkably, just these two conductances were enough to generate AP like behaviour in a cell that itself does not spike. Indeed, by replacing the TREK-1 and TASK-3 conductances with a singular synthetic potassium leak conductance, I was able to recreate these results on a model cell which is essentially just a resistor attached to the head stage of a regular patch-clamp setup.

3.2.3 NON-LINEAR GHK LEAK

The specific non-linear leak conductance I focussed on for this chapter was a non-linear Cl^- modelled by the Goldman-Hodgkin-Katz (GHK) [113–115] equation. The equation models a passive leak current derived from passive ionic diffusion across a cell membrane with an intra- and extra- cellular concentration gradient of said ionic species. The equation modelled by our DCC protocol is shown by Equation 3-1.

$$I = -V \frac{G_{ghk}}{c_{out}} \left(\frac{c_{in} - c_{out} e^{\frac{-VFZ}{RT}}}{1 - e^{\frac{-VFZ}{RT}}} \right) \tag{EQUATION 3-1}$$

Where I is the leak current, V is the membrane voltage, G_{ghk} is the slope conductance at minimum membrane potential, c_{in} and c_{out} are the intracellular and extracellular ionic concentrations respectively, F is Faraday's constant, R is the universal gas constant, Z is the ion's valence, and T is the absolute temperature.

3.2.4 AMPA CONDUCTANCES

The AMPA model conductance selected was an exponential synapse with an instantaneous rise-time and single exponential decay. The model is shown by equation 3-2.

$$g(t) = G_{max} e^{\frac{-t}{\tau_{decay}}} \tag{EQUATION 3-2}$$

Where $g(t)$ time-dependent conductance, G_{max} is the maximum conductance, t is the time, and τ_{decay} decay constant.

3.2.5 SPECIFIC CHAPTER AIMS

This chapter sought to experimentally investigate the effects of realistic AMPA conductances and a non-linear GHK (Cl^-) leak conductances on AP properties using the Dynamic Current Clamp (DCC) method. The scientific goals were as follows:

1) To investigate if varying non-linear leak conductances could have an effect on AP FWHM.
2) To understand if increasing input conductance could have an effect on AP properties.
3) To gain insight into the implications of the above results in the context of functional connectivity mapping.

3.3 MATERIALS AND METHODS

For this chapter, animal and animal care information is detailed in Section 2.1. The ChR2 transgenic strategy and stereotaxic viral injection strategy are detailed in Section 2.2.2. Solutions used for electrophysiology and tissue preparation are described in Sections 2.3.4-6; tissue slice preparation Section 2.4; and whole-cell electrophysiology procedures in Section 2.5.1. Note, the intracellular solution used in this chapter was the K-Gluconate based solution. Further, all electrophysiological recordings were taken from putative pyramidal neurons (as determined by discernible cell morphology and approximate anatomical region) within the Prefrontal Cortex (PFC) of C57BL/6 wild-type animals.

3.3.1 DYNAMIC CURRENT CLAMP – AMPA MODEL VERIFICATION AND IMPLEMENTATION

Model verification

Verification of the modelled AMPA conductance described in Section 3.2.4 was done by current clamping a model cell (PATCH-1U MODEL CELL, Axon Instruments). AMPA conductances were programmed into Signal (V6.05b, Cambridge Electronic Devices), the electrophysiology software, with the following parameters: τ_{decay}= 2 ms, and E_r, reversal potential = -10 mV. The set of maximum conductances G_{max} ranged from 25 – 70 nS in 5 nS increments. These conductances were chosen to give a set of minimal single events which could evoke Action Potentials in neurons. Note, the equation being modelled by Signal was that described in section 3.2.4. Once programmed in, the conductances were imposed on to the model cell whist reading out the current through the cell. The cell was then held had a range of ‘membrane’ voltages using the Multiclamp Command UI, at a range between -75 mV to -50 mV in 5 mV increments; these voltages were chosen to represent the physiological ranges one might find in real electrophysiology experiments. At each voltage, the set of AMPA conductance states were run to determine the effect of membrane voltage on AMPA conductance.

Model implementation

Implementing the set of model AMPA conductances was done as follows: neurons were whole-cell patched and held in current clamp as described in Section 2.5.1. Once the recording was deemed stable (as noted by a stable leak current less than $\pm$ 10 pA), the set of model conductance states as described above were randomly imposed on to the neuron, with 500 milliseconds between n = 5 trials. There was a 200 ms time window between states-trial sets. The recoding was checked after the whole set was run to ensure it was still healthy.

3.3.2 DYNAMIC CURRENT CLAMP – GHK MODEL VERIFICATION AND IMPLEMENTATION

Model verification

Verification of the modelled GHK conductances described in Section 3.2.3 was done by current clamping a model cell (PATCH-1U MODEL CELL, Axon Instruments) as with the AMPA model verification, but with the additional step of connecting the command voltage of a secondary Power1401 (Cambridge Electronic Design) amplifier channel into the model cell. In this way, this secondary command voltage could impose a saw-tooth voltage command to the model cell, in effect simulating a smooth range of 'membrane' voltages from -100 mV to + 50 mV.

GHK conductances were programmed in to Signal (V6.05b, Cambridge Electronic Devices) with the following parameters: c_{in} = 6 mM, c_{out} = 131.5 mM, $Temp$ = 22°C (the approximate lab temperature), $Valency$ = -1, and the set of maximum conductances G_{ghk} = [0.03, 0.3, 1, 2, 3] nS. Each of this conductances were set as a separate current clamp protocol in Signal, and within protocol I programmed the set of AMPA conductance as described above in Section 3.3.1. Note once again, the equations being modelled 'behind the scenes' of the Signal GUI was those described in Sections 3.2.3-4.

Once programmed in, each GHK conductance protocol was run on the model cell as with whilst the command voltage from the secondary Multiclamp channel imposed the voltage range described above. In this way we could get a reading of the current through the model cell at varying 'membrane' voltages to see how the conductance varies with voltage. This validation step sought to check the range of G_{ghk} values we could use such that we ensure GHK conductance-mediated currents were within physiological limits over the range of membrane voltages that one might see over the course of a real whole-cell recording.

Model implementation

Implementing the set of model GHK conductances was done similarly to the AMPA model implementation: neurons were whole-cell patched and held in current clamp as described in Section 2.5.1. Once the recording was deemed stable (as noted by a stable leak current magnitude less than 10 pA), the set of GHK conductance protocols as described above were randomly imposed on to the neuron, with each protocol running the set of AMPA conductances as described in section 3.3.1. In this way, we could yield multi-dimensional datasets describing how AMPA conductance and GHK leak affect AP properties. The recording was checked after each protocol was run to ensure it was still healthy. Finally, to assess the effect of the GHK leak on neuronal resting potential (RMP), patched neurons were current clamped whilst injecting zero current, and

3.3.3 DETERMINING WHOLE-CELL RECORDING PARAMETERS AND DEFINING AP HEIGHT, LATENCY, AND FULL WIDTH, HALF-MAXIMUM

Whilst under voltage clamp and before breaking in to the cell membrane, a 10 mV stepping current was applied across the cell membrane. From this, the membrane capacitance was calculated as the area under the capacitance transient current curve shaded in grey on Figure 3-1 **a**, divided by the 10 mV voltage step. The series resistance was calculated using Ohm's law, specifically series resistance, $R = {}^{V}/_{\Delta I}$, where V = 10 mV and corresponds to the stepping voltage used during the patching procedure, and ΔI is the maximum current response as shown in Figure 3-1 **a**.

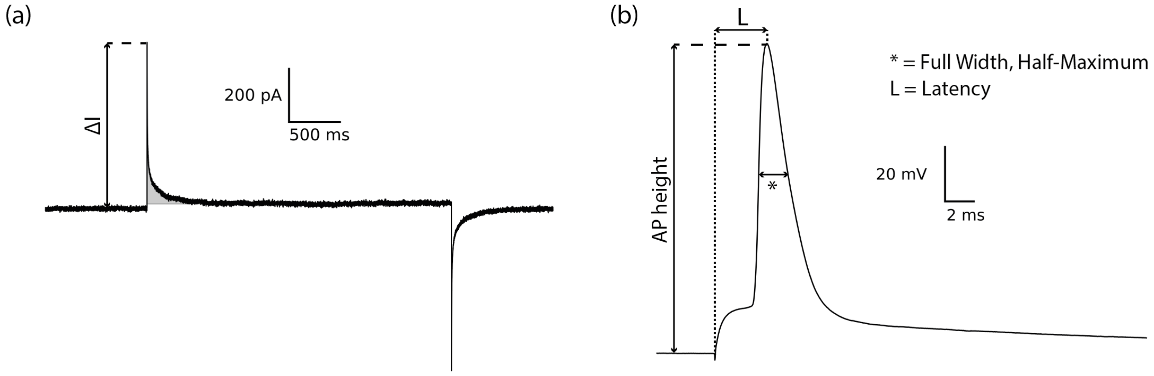

Figure 3-1 Whole- cell recording quality and action potential parameters were recorded systematically across all experiments. a *Whilst under voltage clamp, a 10 mV stepping current was applied across the cell membrane. From this, series resistance was calculated using Ohm's law, specifically R = V / (ΔI) where V = 10 mV corresponding to the stepping voltage used during the patching procedure. The Action Potential (AP) height, latency, and Full Width, Half-Maximum were calculated based on the annotations shown in* ***b****. Note, the beginning of the latency window corresponds to the stimulus onset, and this example trace was taken whilst the neuron was under current clamp and an AMPA conductance was imposed with a peak conductance of 35 nS- full methodology described in Section 3.3.1.*

The Action Potential (AP) height, latency, and Full Width, Half-Maximum were calculated based on the annotations shown in Figure 3-1 **b**. Note, the beginning of the latency window corresponds to the stimulus onset. Qualitatively, the AP peak voltage (or height) was determined as the maximum voltage of the AP itself, minus the baseline voltage which was taken as the average membrane voltage in the 50 ms preceding the stimulus; the AP latency was the time between stimulus onset and AP peak; and finally, the FWHM, illustrated by the asterisk in Figure 3-1 **b**, as determined as the Full Width at Half Maximum of the AP curve between the threshold point and the point at which the membrane returns to this threshold voltage. Note, the description and methodology for finding this threshold point can be found in section 3.3.4, and Figure 3-2.

3.3.4 CUSTOM DATA ANALYSIS PIPELINES WERE DEVELOPED TO SYSTEMATICALLY DETERMINE ACTION POTENTIAL (AP) PARAMETERS

To ensure that AP parameters were systematically and reliably determined across all recordings, I wrote custom data analysis pipelines in python to process all electrophysiological records. Figure 3-2 shows an outline of this pipeline, as well as an illustration of how the AP threshold was determined, which crucially determines how the AP FWHM was determined.

Raw electrophysiological data was first fed into the pipeline (Figure 3-2 **a**), segmented into events using *a priori* knowledge of current clamp stimulus times, and then filtered using a 50 Hz long pass filter to remove any line noise in the signal. Next, each AP event was manually checked to ensure it was properly segmented before characterising each to find the AP height, latency, and FWHM. This manual checking was to minimise the effect of rouge software bugs in our analysis. These data were finally aggregated and passed on for further statistical analysis.

A key part of the process was detecting the AP threshold; this was found taking the second derivative of the neuron's membrane current over the course of the AP (Figure 3-2 **b**). Time t=0 corresponds to the stimulus onset (in this case an AMPA conductance using the Dynamic Current Clamp method described in 3.3.2). The vertical dashed red line represents the AP threshold, determined by the first peak in bottom plot. Physically, this peak represents the moment the neuron reaches its AP threshold. Using this same process for all AP events ensured systematic analysis of all data.

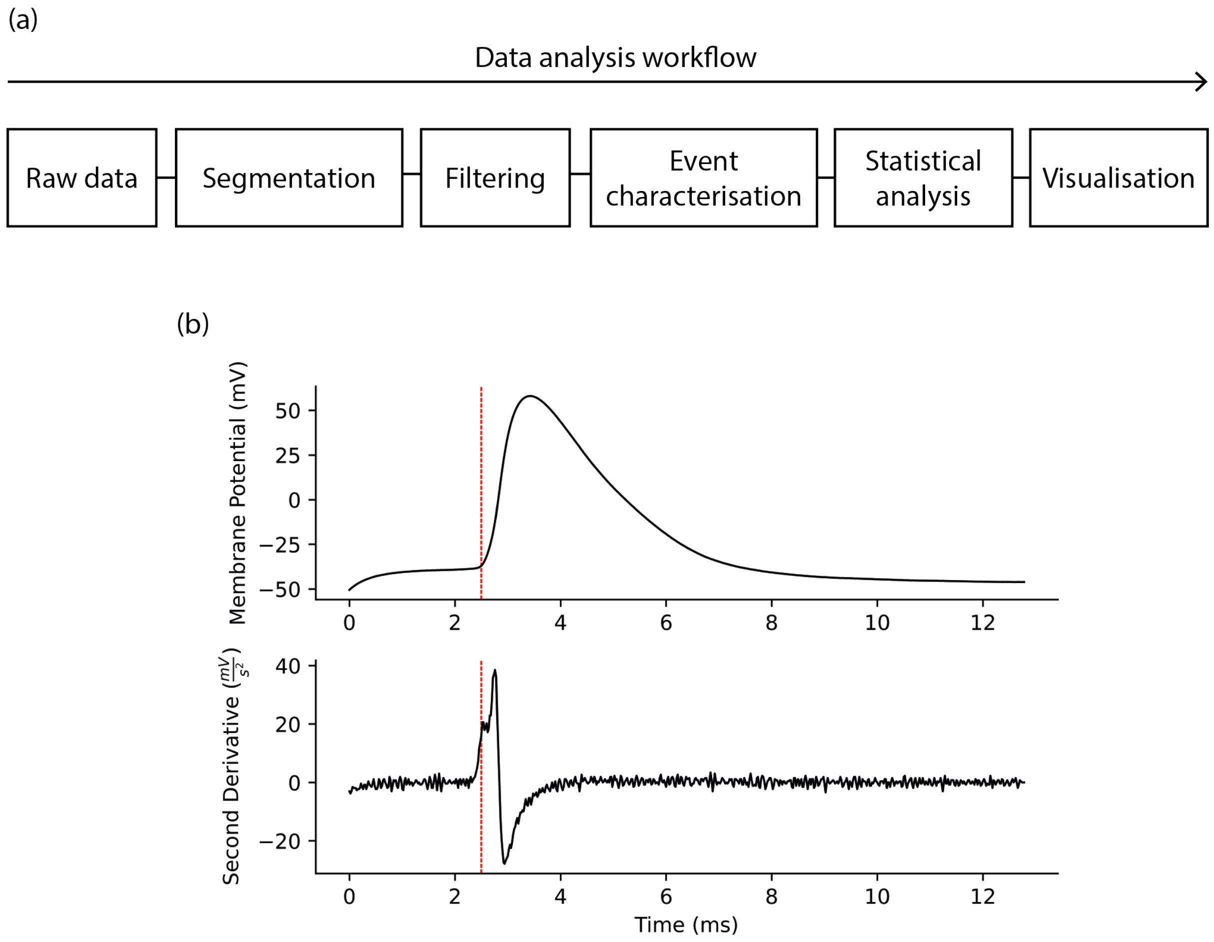

Figure 3-2 Custom data analysis pipelines were developed to systematically determine Action Potential (AP) parameters*.* ***a*** *Data pipelines took in raw electrophysiological data from Signal (V6.05b, Cambridge Electronic Devices) and then followed robust segmentation, filtering, characterisation, and statistical analysis steps before being visualised.* ***b*** *Top: an example of a segmented AP taken from a current clamp recording of a prefrontal cortex neuron. Bottom: the corresponding second derivative of the neuron's membrane current over the same time course. Time t=0 corresponds to the stimulus onset (in this case an AMPA conductance using the Dynamic Current Clamp method described in section 3.3.1). The vertical dashed red line represents the AP threshold, determined by the first peak in bottom plot. Physically, this peak represents the moment the neuron reaches its AP threshold. For each recording and trial, I used the same data analysis pipeline to find the threshold and subsequent AP parameters. This ensured systematic analysis across all experiments. Statistical analysis encompassing averages, standard deviations, regression analysis, Kernel Density Estimates were done using open source python packages- specifically SciPy, Seaborn, and NumPy.*

3.4 RESULTS

3.4.1 WHOLE-CELL RECORDING SERIES RESISTANCE BREAKDOWN

To ascertain the role of the series resistance, and by extension whole- cell recording quality on AP properties, I first quantified the range of series resistances used for this study. Figure 2-3 shows range and distribution of series resistances used: across 23 recordings the mean value was 24.67 ± 1.92 MOhm (± Standard Error of the Mean). The standard deviation was 9.03 MOhm. Note, these values were calculated by the method described in section 3.3.3.

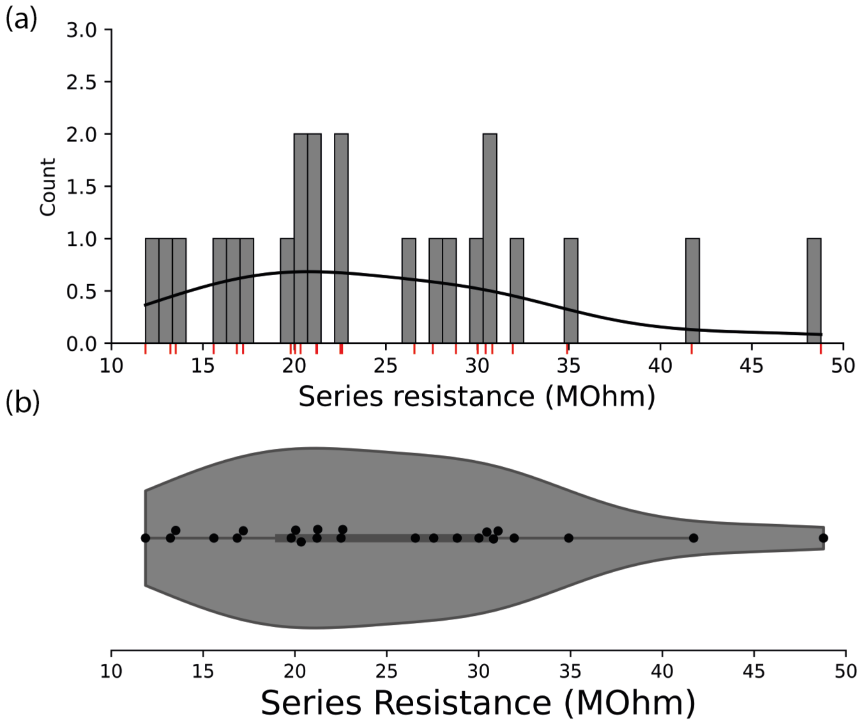

***Figure 3-3 Whole-cell recording series resistance breakdown**. **a** Histogram showing the distribution of series resistances across n = 23 whole-cell recordings. Red ticks on the x-axis represent the series resistances of individual neurons which were each calculated by averaging over n = 5 trials using the methodology outline in section 3.3.1. The black plotted curve represents the kernel density estimate (KDE) with a gaussian kernel and bin width of 0.3. I chose this bin width to ensure each sample point was taken in to account when estimating the KDE; higher or lower values under and overestimated the curve respectively. The average series resistance was 24.67 ± 1.92 MOhm (± Standard Error of the Mean). The standard deviation was 9.03 MOhm.*

***b** A violin plot of the same data in a. Each black dot represents a sample point, and the shaded region represents the KDE of the data.*

3.4.2 Action Potential (AP) latency and whole- cell recording series resistance have a weakly positive correlation

Across the same 23 neurons, it was seen that there was a weakly positive correlation (Spearman's Correlation Coefficient = 0.433) between AP latency and recording series resistance. Furthermore, the average latency was 4.76 ± 1.03 ms (± Standard Error of the Mean), and the standard deviation was 4.87 ms. Note, this large standards deviation can be explained by the two neurons in the dataset which had latencies above 15 ms. They were left in and not excluded as the recordings were deemed healthy based of the recording series resistance.

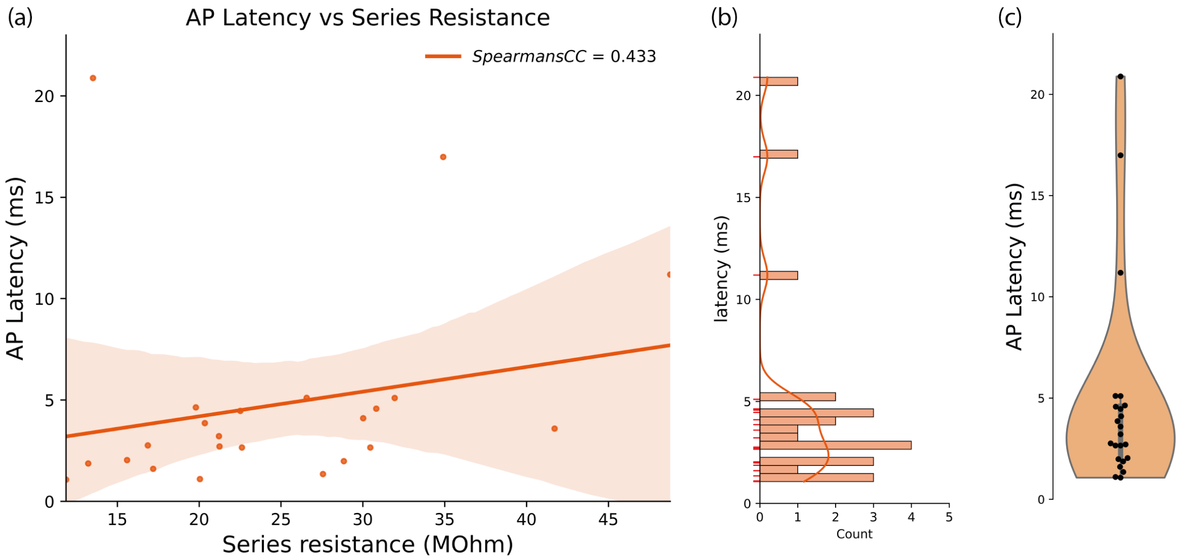

***Figure 3-4 Action Potential (AP) latency and whole- cell recording series resistance have a weakly positive correlation**. **a** Linear regression showing the AP latency of n = 23 neurons versus their respective recording series resistance. Each latency was calculated by averaging over n = 5 trials where each trial corresponded to an AP which fired under the lowest AMPA conductance input tested on that particular neuron, i.e., this data represents the average AP which is evoked with the minimal current input to each neuron. The Spearman's Correlation Coefficient value was 0.433, suggesting a weak correlation between latency and series resistance. The dark orange line represents the linear regression, and the shaded orange area represents the*

95% confidence interval. ***b*** *Histogram showing the distribution of latencies. Red ticks on the y-axis represent the average latency of individual neurons. The orange plotted curve represents the kernel density estimate (KDE) with a gaussian kernel and bin width of 0.3. The average latency was 4.76 ±1.03 ms (±Standard Error of the Mean). The standard deviation was 4.87 ms.* ***c*** *A violin plot of the same data in b. Each black dot represents a sample point, and the shaded region represents the KDE of the data.*

3.4.3 ACTION POTENTIAL (AP) PEAK AND WHOLE- CELL RECORDING SERIES RESISTANCE HAVE A WEAKLY NEGATIVE CORRELATION

Following AP latency, I then demonstrated that the AP peak voltage had a weakly negative correlation to the recording series resistance (Spearman's Correlation Coefficient = -0.354). The average AP peak was 46.09 ± 2.13 mV (± Standard Error of the Mean). The standard deviation was 10.01 mV.

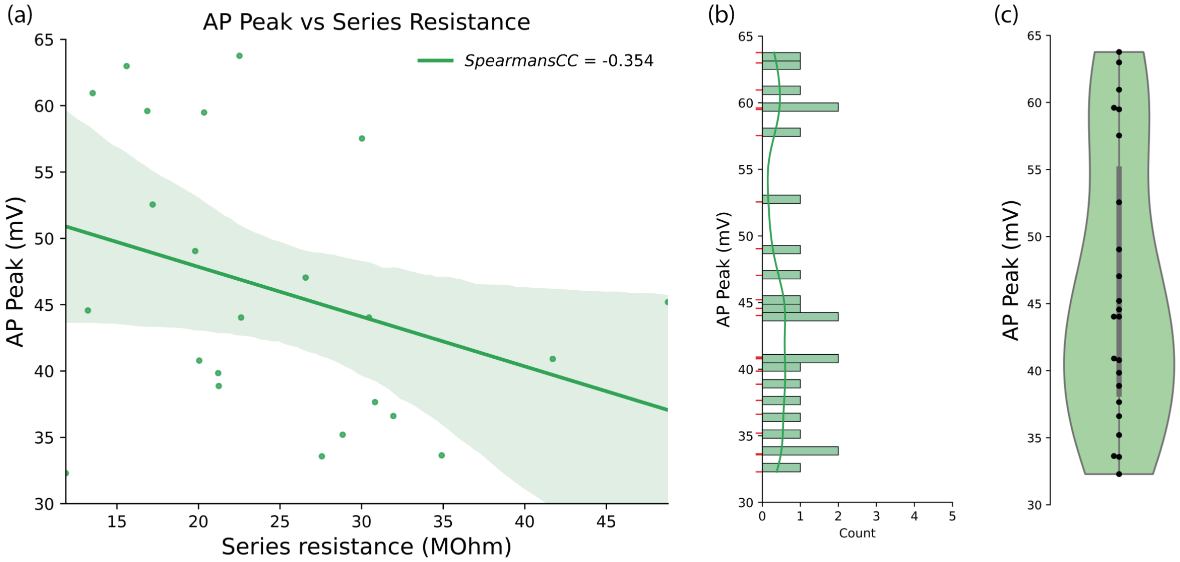

Figure 3-5 Action Potential (AP) peak and whole- cell recording series resistance have a weakly negative correlation. ***a*** *Linear regression showing the AP peak of n = 23 neurons versus their respective recording series resistance. Each latency was calculated by averaging over n = 5 trials where each trial corresponded to an AP which fired under the lowest AMPA conductance input tested on that particular neuron, i.e., this data represents the average AP which is evoked with the minimal current input to each neuron. The Spearman's Correlation Coefficient = -0.354, suggesting a weakly negative correlation between AP peak and series resistance. The dark green line represents the linear regression, and the shaded green area represents*

the 95% confidence interval. ***b*** *Histogram showing the distribution of AP peaks. Red ticks on the y-axis represent the average AP peak voltage of individual neurons. The green plotted curve represents the kernel density estimate (KDE) with a gaussian kernel and bin width of 0.3. The average AP peak was 46.09 ±2.13 mV (± Standard Error of the Mean). The standard deviation was 10.01 mV.* ***c*** *A violin plot of the same data in b. Each black dot represents a sample point, and the shaded region represents the KDE of the data.*

3.4.4 Action Potential (AP) Full Width, Half-Maximum (FWHM) and whole-cell recording series resistance have a weakly positive correlation

Finally, it was seen that the AP FWHM was weakly correlated to the recording series resistance (Spearman's Correlation Coefficient = 0.375). The average AP FWHM was 2.30 ± 0.18 ms (± Standard Error of the Mean), and the standard deviation was 0.86 ms.

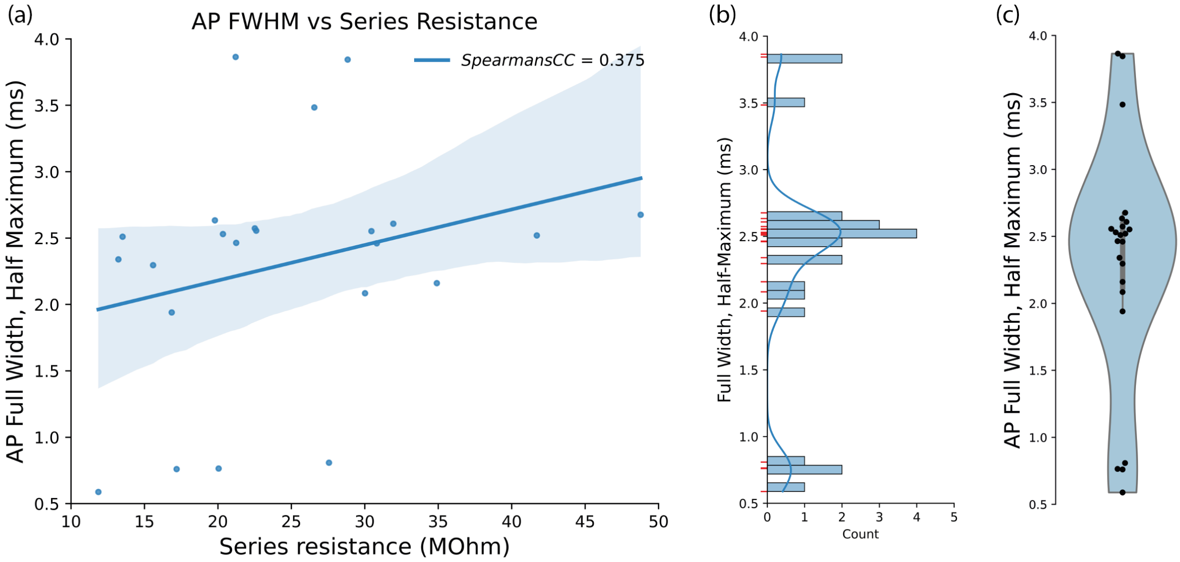

Figure 3-6 Action Potential (AP) Full Width, Half-Maximum (FWHM) and whole- cell recording series resistance have a weakly positive correlation. ***a*** *Linear regression showing the AP FWHM of n = 23 neurons versus their respective recording series resistance. Each latency was calculated by averaging over n = 5 trials where each trial corresponded to an AP which fired under the lowest AMPA conductance input tested on that particular neuron, i.e., this data represents the average AP which is evoked with the minimal current input to each neuron. The Spearman's Correlation Coefficient = 0.375, suggesting a weakly positive correlation between AP FWHM and series resistance. The dark blue line represents the linear regression, and the shaded*

blue area represents the 95% confidence interval. ***b*** *Histogram showing the distribution of AP FWHMs. Red ticks on the y-axis represent the average AP FWHM of individual neurons. The blue plotted curve represents the kernel density estimate (KDE) with a gaussian kernel and bin width of 0.3. The average AP FWHM was 2.30 ±0.18 ms (±Standard Error of the Mean). The standard deviation was 0.86 ms.* ***c*** *A violin plot of the same data in b. Each black dot represents a sample point, and the shaded region represents the KDE of the data.*

Once the effects of recording series resistance on AP properties were quantified, I then moved on to validate the GHK model used with the dynamic correct clamp method to ensure its suitability for our needs.

3.4.5 NON-LINEAR CL$^-$ GOLDMAN-HODGKIN-KATZ (GHK) LEAK VALIDATION

As the GHK model used would be imposing a non-linear, voltage dependent current to patch clamped neurons (for a full description of this model and it's validation, see 3.3.2), we needed to ensure that the conductances were physiologically suitable for our experiments. Specifically, that across the range of membrane voltages a neuron might naturally be at whilst at rest and whilst firing action potentials, the leak conductances would not be large enough to affect the neurons health.

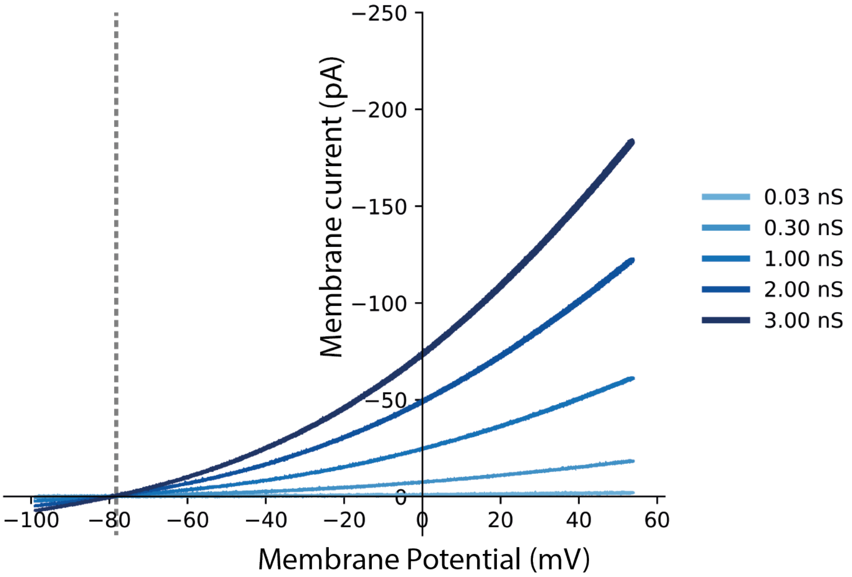

Figure 3-7 Non-linear Cl- Goldman-Hodgkin-Katz (GHK) leak validation*. Altering the membrane voltage whilst imposing a non-linear leak conductance (for full methodology, see section 3.3.2) on a model cell (PATCH-1U MODEL CELL, Axon Instruments) results in a non-linear response in input current. As the*

membrane potential moves away from the reversal potential of the GHK model (grey dashed line), there is a non- linear current response which acts to drive the membrane potential back to the reversal potential. Increasing the magnitude of the GHK leak (0.03 – 3.00 nS, represented by the range of blue curves) shows that the larger the magnitude of the GHK leak, the steeper gradient of the non-linear current response as the neuron's membrane potential moves away from the model reversal potential.

Using a model cell as described in section 3.3.2, I demonstrate the range of conductances that the GHK model could impose on a real neuron were within acceptable physiological limits: injected currents between +10 pA and -200 pA at membrane voltages between -100 mV and 50 mV respectively, whilst using a maximum GHK leak conductance of 3.0 nS. In other words: using a maximum GHK leak voltage of 3.0 nS ensured that leak currents imposed by the model described in section 3.3.1 were within the regular bounds that a neuron may experience naturally, so long as the neuron's membrane potential was also within its physiological limits (-100 mV to 50 mV). This validation process is described further in section 3.3.2. This is seen graphically in Figure 3-7. Furthermore, increasing the magnitude of the GHK leak (0.03 – 3.00 nS, represented by the range of blue curves in Figure 3-7) shows that the larger the magnitude of the GHK leak, the steeper gradient of the non-linear current response as the neuron's membrane potential moves away from the model reversal potential.

3.4.6 A NON-LINEAR CL- GOLDMAN-HODGKIN-KATZ (GHK) LEAK DRIVES NEURONAL RESTING MEMBRANE POTENTIAL TOWARDS THE MODEL REVERSAL POTENTIAL

A theoretical observation of neuron membrane potential whilst increasing the magnitude of the GHK leak conductance is that the membrane potential will be 'driven' towards the reversal potential (the membrane potential at which no current arises from a particular conductance) of the GHK model. An example of this is neuron resting membrane potential; by increasing the GHK leak conductance, the resting potential should shift towards -77 mV. This was seen experimentally across n = 9 recorded neurons on to which I imposed increasing GHK leak conductance on using dynamic current clamp. Figure 3-8 shows these data.

Once the GHK model conductances were validated as described in section 3.4.5, I then sought to validate the AMPA conductances used to ensure they too with physiological relevant ranges and suitable for our needs.

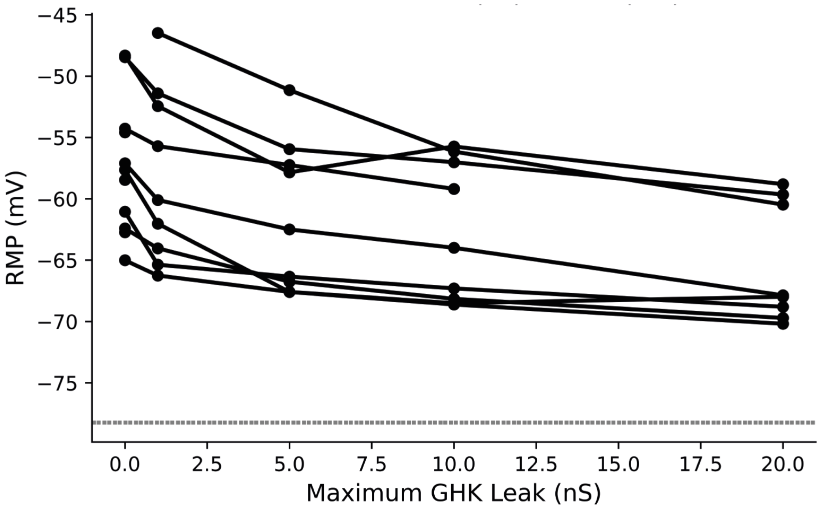

Figure 3-8 A non-linear Goldman-Hodgkin-Katz (GHK) Cl- leak drives neuronal resting membrane potential towards the model reversal potential*. Using Dynamic Current Clamp to impose a non-linear GHK leak on whole-cell recordings of PFC neurons shows that increasing the GHK leak pushes the neuron's Resting Membrane Potential (RMP) towards the model reversal potential (grey dashed line, discussed in section 3.4.6). Each connected curve represents data from a single neuron, with n = 9 neurons shown. RMPs are found by averaging the resting membrane potential of the neuron over a 1 s window whilst in current clamp injecting no current outside of the current resulting from the GHK leak conductance model.*

3.4.7 VALIDATION OF AMPA CONDUCTANCES USED TO STUDY THE ACTION POTENTIAL (AP) PROPERTIES OF PREFRONTAL CORTEX (PFC) NEURONS.

A goal of this chapter was to measure the effects of realistic AMPA conductances on action potential properties. Hence, I needed to validate the AMPA models used to evoke action potentials in target neurons. Figure 3-9 shows these results.

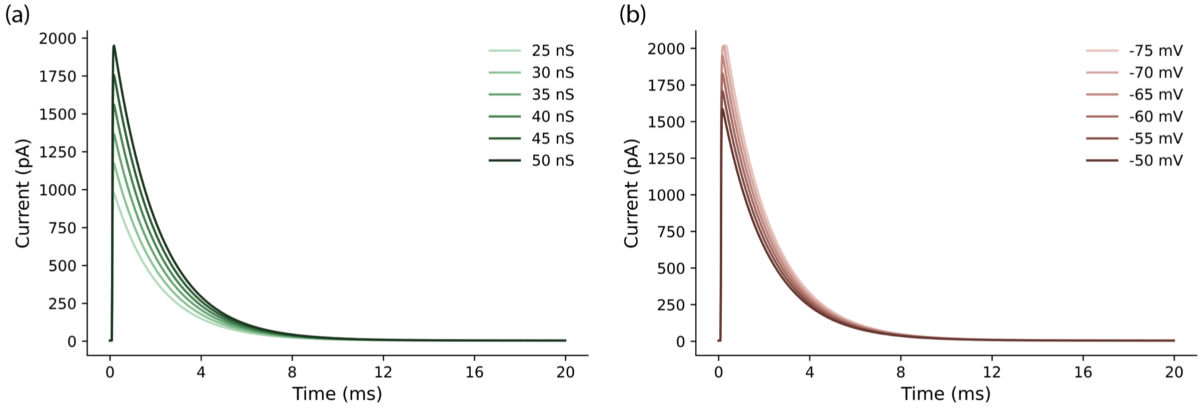

***Figure 3-9 Validation of AMPA conductances used to study the Action Potential (AP) properties of Prefrontal Cortex (PFC) neurons**. These data were recorded using the Dynamic Current Clamp method on a model cell (section 3.3.1). **a** Increasing the maximum AMPA conductance increases the magnitude of current injected into the model cell, from 990 pA to 1961 pA at 25 nS and 50 nS maximum AMPA conductances respectively. Increasing maximum conductances are shown in darker shades of green and described in the legend. **b** The Resting Membrane Potential (RMP) of the neuron effects the magnitude of current injected; the maximum current rises from 1560 pA to 2000 pA at -50 mV and -75 mV respectively. Each curve represents an AMPA conductance of 45 nS imposed on a different RMP. The range of RMPs used represent physiological values observed experimentally, with darker shades of red representing lower RMPs. Curves described in the legend; the darker the hue of red, the higher the RMP.*

Using a model cell as described in section 3.3.1, it is seen that increasing the maximum AMPA conductance increases the magnitude of current injected into the model cell from 990 pA to 1961 pA at 25 nS and 50 nS maximum AMPA conductances respectively (Figure 3.9 **a**). Furthermore, changing the resting membrane potential of the model cell to ranges between – 75 mV to -50 mV effects the current injected from 1560 pA to 2000 pA whilst using the same input conductance- as shown in Figure 3.9 **b** using an AMPA conductance of 45 nS as an example. Note, this validated the model used by ensuring the currents injected by the model across all testing parameters (that is, the range of AMPA conductances between 25 nS and 50 nS and membrane potentials between -50 mV and 70 mV) were within physiological ranges which would minimise harm to the neuron whilst giving an understanding of AP properties which would occur naturally.

3.4.8 CHARACTERISATION OF CHARGE TRANSFER DURING AMPA CONDUCTANCE TIME COURSE

Another way of interpreting the input into a neuron is by monitoring charge transfer over the course of the input event. This can be calculated by integrating under the current-time curve of the event. Figure 3-10 shows this process and result. As expected, the larger the AMPA conductance, the larger the charge transfer over the course of the event. Further, the more depolarised the neuron, the lower the total charge transfer.

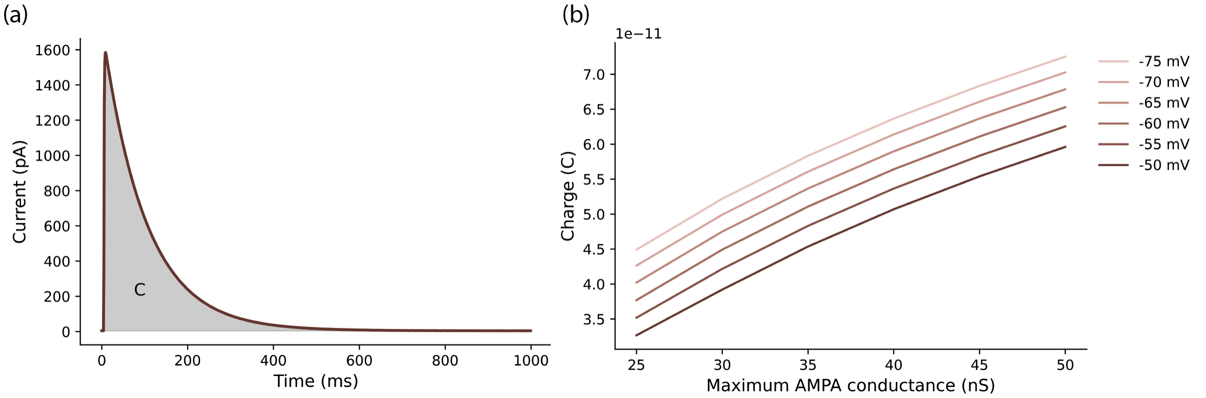

Figure 3-10 Characterisation of charge transfer during AMPA conductance time course*. The charge transferred during the AMPA conductance was found by integrating the area under the conductance curve, show by the shaded grey area C, noted in* ***a****.* ***b*** *Graph showing how increasing the maximum AMPA conductance increases the charge transferred during the AMPA time course, and furthermore how increasing the resting membrane potential (darker red curves) decreases the amount of charge transferred. Data were collected by running dynamic current clamp models on a model cell (for full methodology see section 3.3.1). Charge calculations were taken from single AMPA conductance curves.*

3.4.9 RAW TRACES SHOWING THE EFFECTS OF INCREASING AMPA CONDUCTANCE ON ACTION POTENTIAL PROPERTIES

Once characterised, it was then time to gain and understanding of how AMPA conductances effect AP properties. By using the dynamic current clamp method with the AMPA model as described in sections 3.3.1 and 3.3.2 respectively, I began to quantify this relationship; Figure 3-11 shows the effect of increasing AMPA conductance on one example neuron.

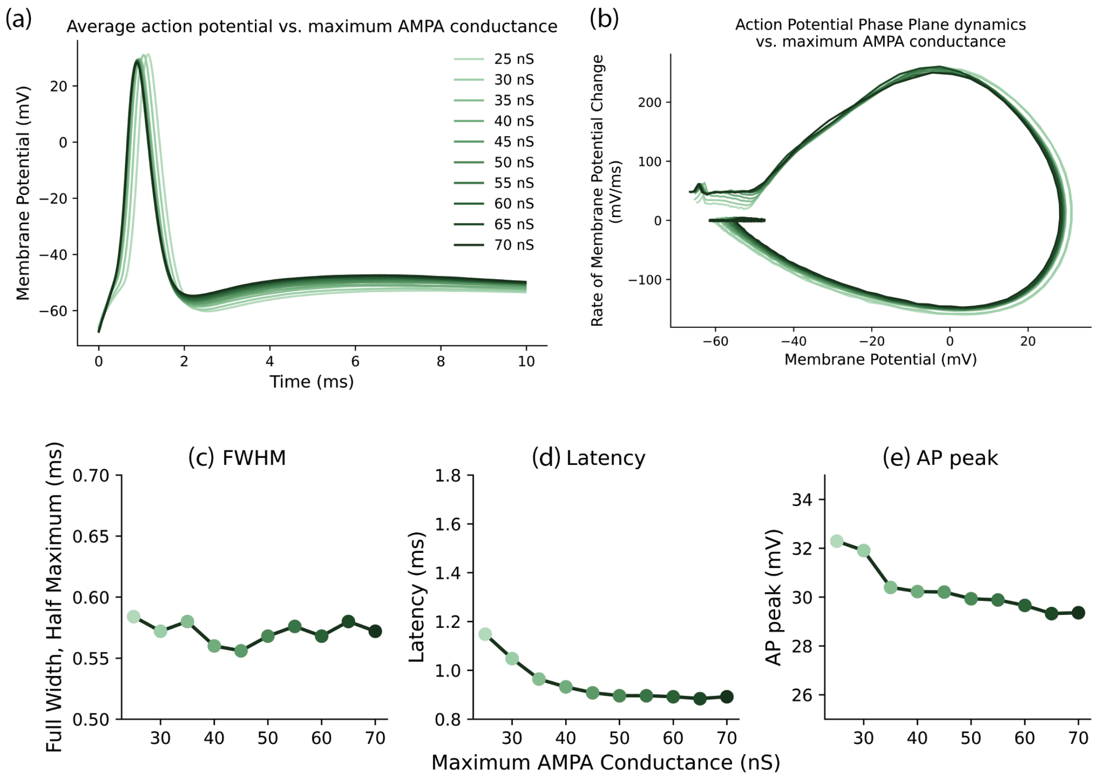

*Figure 3-11 **Raw current-clamp traces showing the effects of increasing AMPA conductance on action potential properties**. **a** Trial-averaged action potential (AP) traces of a single neuron reacting to increasing maximum AMPA conductance (darker green traces). **b** Trial- averaged phase-plane plots of the same traces in a. The phase-plane plots narrow with increasing conductance. **c-e** quantification of the Full-Width, Half Maximum (FWHM), latency, and AP peak voltage for the traces shown in **a** and **b**. The FWHM remains stable across the conductance range with an average FWHM of 0.572 ms, standard deviation of 0.008 ms, and range of 0.028 ms. The latency and AP peak both decrease with increasing conductance; from 25 nS to 70 nS, latencies drop 29.8 % from 1.148 ms to 0.884 ms, and the AP peak drops 10.1 % from 32.29 mV to 29.31 mV. Each trace and data point were averaged over n = 5 trials. Note, error bars for each individual point (and hence trial average) are too small to be shown on this scale.*

Overlaying trial- averaged (n=5), raw AP traces and phase-plane plots (Figure 3-11 **a**, **b**) show how an AP is affected by input AMPA conductance. Qualitatively, we see that the latency and AP peak both decrease with increasing maximum AMPA conductance. Figures 3-11 **c**-**e** quantify these data. The FWHM remains stable across the conductance range with an average FWHM of 0.572 ms, standard deviation of 0.008 ms, and range of 0.028 ms. The latency and AP peak both decrease with increasing conductance; from 25 nS to 70 nS, latencies drop 29.8 % from 1.148 ms to 0.884 ms, and the AP peak drops 10.1 % from 32.29 mV to 29.31 mV.

3.4.10 RAW TRACES CURRENT-CLAMP TRACES SHOWING THE EFFECTS OF INCREASING GHK LEAK CONDUCTANCE ON ACTION POTENTIAL PROPERTIES.

Similarly, overlaying trial- averaged (n=5) raw AP traces and phase plane plots (Figure 3-12 **a**, **b**) shows qualitatively how AP properties are affected by GHK leak conductance. In an example neuron shown in Figure 3-12, we see that using the GHK model with the dynamic current clamp technique described in section 3.3.2 that there is an increase in AP latency and decrease in AP peak. Further, we see that the FWHM remains stable across the conductance range. Quantitatively, Figure 3-12, **c**-**e** show this result: the FWHM remains stable across the conductance range with an average FWHM of 0.591 ms, standard deviation of 0.007 ms, and range of 0.016 ms. Across the same conductance range of 0 nS to 20 nS, the latency increases by 49.5 % from 1.148 ms to 1.716 ms, and the AP peak decreases from 32.29 mV to 27.28 mV- constituting a18.35 % drop. Note, these data are collected by analysing the AP waveforms of a single neuron when stimulated with the lowest AMPA which evoked an AP across the entire GHK conductance range.

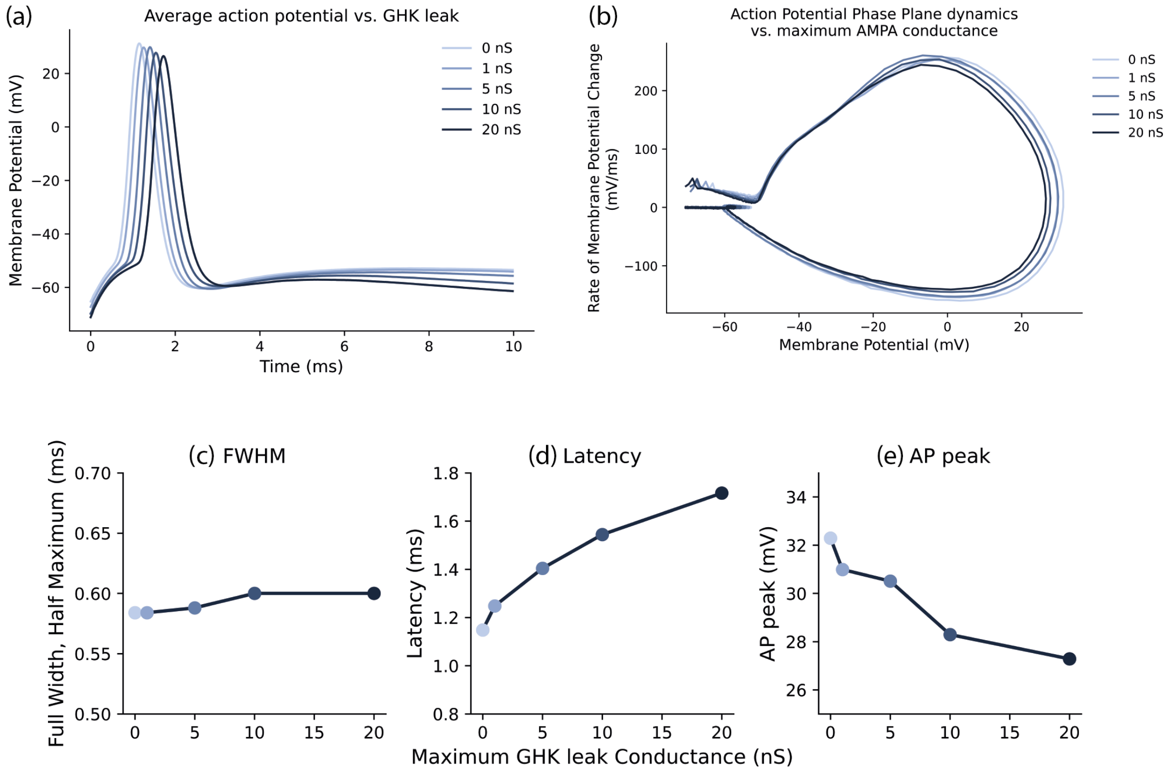

***Figure 3-12 Raw traces showing the effects of increasing GHK leak conductance on action potential properties**. **a** Trial-averaged action potential (AP) traces of a single neuron reacting to increasing GHK leak conductance (darker blue traces). The APs diminish in voltage and shift to the right. **b** Trial- averaged phase-plane plots of the same traces in **a**. The phase-plane plots narrow with increasing leak conductance. **c-e** quantification of the Full-Width, Half Maximum (FWHM), latency, and AP peak voltage for the traces shown in **a** and **e**. show this result: the FWHM remains stable across the conductance range with an average FWHM of 0.591 ms, standard deviation of 0.007 ms, and range of 0.016 ms. Across the same conductance range of 0 nS to 20 nS, the latency increases by 49.5 % from 1.148 ms to 1.716 ms, and the AP peak decreases from 32.29 mV to 27.28 mV- constituting a18.35 % drop. Each trace and data point were averaged over n = 5 trials, and the APs represented here were recorded at the lowest single AMPA conductance which evoked an AP across all leak conductances. Note, error bars for each individual point (and hence trial average) are too small to be shown on this scale.*

3.4.11 Increasing the maximum AMPA conductance and GHK leak conductance did not affect the action potential (AP) Full Width, Half-Maximum (FWHM) across recorded neurons.

Following the same procedures outlined in section 3.3.1-2, it was seen that increasing the maximum AMPA conductance and GHK leak conductance did not affect the FWHM across all recorded neurons; Figure 3-13 shows the aggregation of this data. The average FWHM across n=9 neurons are plotted in black, whilst the trial average (n = 5 trials) of each of those individual neurons in plotted in grey. We observe that increasing the AMPA conductance shows no discernible effect on FWHM; the average standard deviation on the FWHM across all neurons and AMPA conductances was 0.009 ms, 0.011 ms, and 0.014 ms for GHK leak conductances of 0 nS (a), 1 nS (b), and 5 nS (c) respectively.

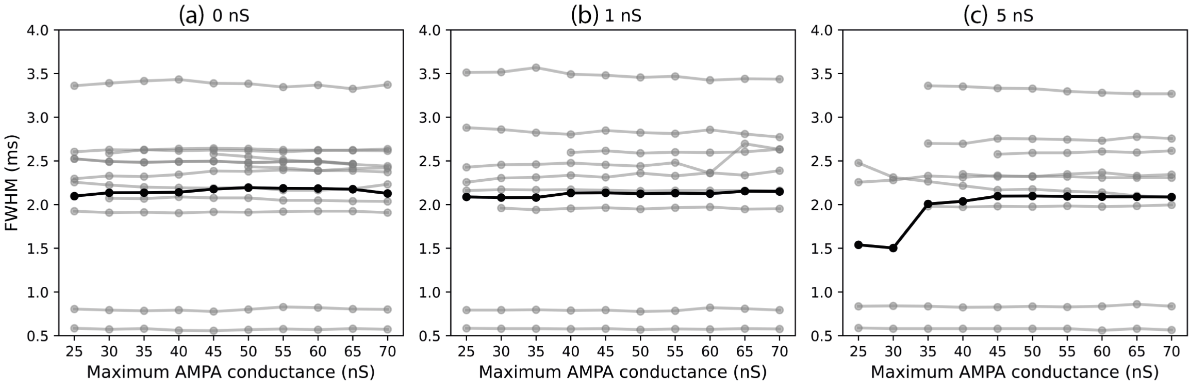

Figure 3-13 Increasing the maximum AMPA conductance and GHK leak conductance did not affect the action potential (AP) Full Width, Half-Maximum (FWHM) in recorded neurons*. By aggregating data across n=9 neurons* ***a-c****, corresponding to GHK maximum leak conductances of 0 nS, 1 nS, and 5 nS respectively, we see that an increase in maximum AMPA conductance does not change the FWHM of an AP. Each grey curve represents data from a single neuron, whilst the black curve represents the average across all neurons. Each spot or data point was taken after averaging n=5 trials, and error bars are too small to be shown on this scale. On average, increasing the GHK leak conductance demonstrated no effect on the FWHM; the average standard deviation on the FWHM across all neurons and AMPA conductances was 0.009 ms, 0.011 ms, and 0.014 ms for GHK leak conductances of 0 nS (****a****), 1 nS (****b****), and 5 nS (****c****) respectively. %). It is important to note that the standard deviation of the FWHM for each neuron was calculated across the range of AMPA conductances which were able to evoke action potentials in the neuron. We further observe that increasing the GHK leak*

*conductance prohibits the neuron from firing an AP at lower AMPA conductances. This explains the gradual loss of data points at lower AMPA conductance trials as we increase the GHK leak conductance (moving from graph **a** to **c**): the increasing GHK leak hyperpolarises the cell and can be seen as an inhibitory conductance on the neuron.*

Similarly, increasing the GHK leak conductance shows no discernible change in FWHM across all neurons. If we discount the datapoints for the average FWHM at 25 nS and 30 nS AMPA conductances whilst using a 5 nS GHK leak conductance- these points can be seen as outliers which exist due to the hyperpolarising effect on the neuron leading to lower AMPA conductances not being able to evoke APs in 4 of the 9 neurons- then the average FWHM across all neurons was 2.02 ms, 2.03 ms, and 2.01 ms for GHK leak conductances of 0 nS, 1 nS, and 5 nS (Figure 3-13 **a**-**c**) respectively.

In 4 of the 9 recorded neurons, we also observe a 'losses of data as we increase the GHK leak conductance (moving from left to right in Figure 3-13). This can be explained by the hyperpolarising effect of the GHK leak on a neuron which can be seen as a constant inhibitory conductance- the consequence of which is that the neuron would require larger input conductances or charge transfers across its membrane to reach AP threshold. In the context of this experiment: lower AMPA conductances were not able to evoke APs in some of the patched neurons when we increased the GHK leak conductance from 0 nS to 5 nS.

3.4.12 INCREASING THE MAXIMUM AMPA CONDUCTANCE DECREASES THE ACTION POTENTIAL (AP) LATENCY ACROSS ALL RECORDED NEURONS

However, in the same 9 neurons, it was seen that increasing the maximum AMPA conductance decreases the AP latency. Figure 3-14 shows this result. Quantitatively, the average decrease in AP latency across all neurons was 0.42 ms, 1.1 ms, and 0.8 ms for GHK leak conductances of 0 nS, 1 nS, and 5 nS- corresponding to a 21 % decrease, 65 % decrease, and 42 % decrease in AP latency respectively. Note, the decrease in AP latency for each neuron was calculated across the range of AMPA conductances which were able to evoke APs in that particular neuron; these latency data are calculated from the same APs used for the FWHM dataset in section 3.4.11. Hence, the same hyperpolarising effect of the GHK leak conductance is seen here, which leads to 'missing' data in Figure 3-14.

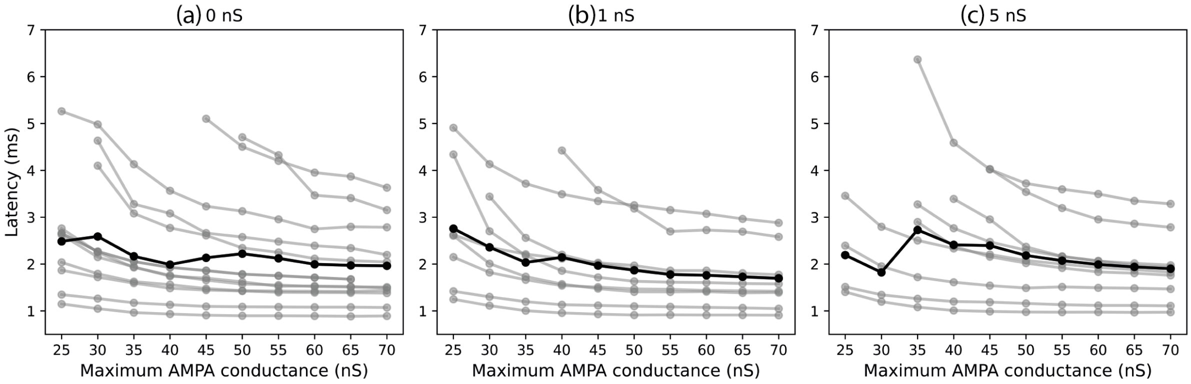

***Figure 3-14 Increasing the maximum AMPA conductance decreases the action potential (AP) latency across all recorded neurons**. By aggregating data across n=9 neurons **a-c**, corresponding to GHK maximum leak conductances of 0 nS, 1 nS, and 5 nS respectively, we see that an increase in maximum AMPA conductance decreases the latency of an AP. The average decrease in AP latency across all neurons was **a** 0.42 ms (21 % decrease), **b** 1.1 ms (65 % decrease), and **c** 0.8 ms (42 % decrease). It is important to note that the decrease in latency of each neuron was calculated across the range of AMPA conductances which were able to evoke action potentials in that particular neuron. Each grey curve represents data from a single neuron, whilst the black curve represents the average across all neurons. Each spot or data point was taken after averaging n=5 trials, where error bars are too small to be seen on this scale. We further observe that increasing the GHK leak conductance prohibits the neuron from firing an AP at lower AMPA conductances. This explains the gradual loss of data points at lower AMPA conductance trials as we increase the GHK leak conductance (moving from graph **a** to **c**): the increasing GHK leak hyperpolarises the cell and can be seen as an inhibitory conductance on the neuron.*

3.4.13 INCREASING THE MAXIMUM AMPA CONDUCTANCE DECREASES THE ACTION POTENTIAL (AP) PEAK VOLTAGE IN RECORDED NEURONS

Finally, in the same set of neurons it was seen that increasing the maximum AMPA conductance decreases the AP peak voltage (Figure 3-15). Quantitatively, the average decrease in AP peak voltage was 7.1 mV, 2.1 mV, and 3.0 mV for GHK leak conductances of 0 nS, 1 nS, and 5 nS- corresponding to a 17 % decrease, 4.9 % decrease, and 7.9 % decrease in AP peak voltage respectively. Similar to section 3.4.12, the decrease in AP peak voltage for each neuron was calculated across the range of AMPA conductances which were able to evoke APs in that particular neuron, and the same hyperpolarising effect of the GHK leak on the neurons (and hence lack of data at lower AMPA conductances as we increase GHK leak conductance) is observed in this data set.

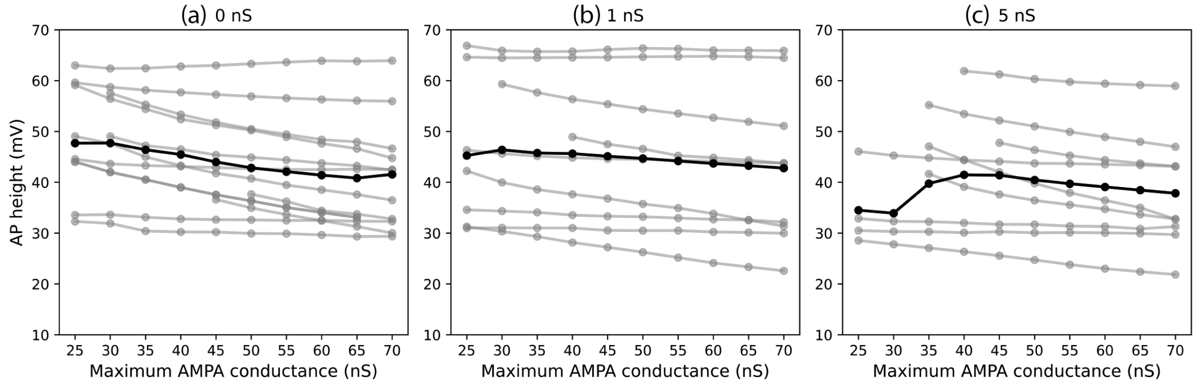

Figure 3-15 Increasing the maximum AMPA conductance decreases the action potential (AP) height in recorded neurons*. By aggregating data across n=9 neurons* ***a****-****c****, corresponding to GHK maximum leak conductances of 0 nS, 1 nS, and 5 nS respectively, we see that an increase in maximum AMPA conductance decreases the latency of an AP. The average decrease in AP peak voltage was* ***a*** *7.1 mV (17 % decrease),* ***b*** *2.1 mV (4.9 % decrease), and* ***c*** *3 mV (7.9 % decrease). It is important to note that the decrease in peak voltage for each neuron was calculated across the range of AMPA conductances which were able to evoke action potentials in that particular neuron. Each grey curve represents data from a single neuron, whilst the black curve represents the average across all neurons. Each spot or data point was taken after averaging n=5 trials, where error bars are too small to be seen on this scale. We further observe that increasing the GHK leak conductance prohibits the neuron from firing an AP at lower AMPA conductances. We further observe that increasing the GHK leak conductance prohibits the neuron from firing an AP at lower AMPA conductances. This explains the gradual loss of data points at lower AMPA conductance trials as we increase the GHK leak conductance (moving from graph* ***a*** *to* ***c****): the increasing GHK leak hyperpolarises the cell and can be seen as an inhibitory conductance on the neuron.*

3.5 DISCUSSION

3.5.1 RECORDING QUALITY SHOWED LITTLE TO NO EFFECT ON AP FWHM, LATENCY, OR PEAK VOLTAGE

Before looking at the relationship between GHK leak conductance or AMPA conductance on AP properties, it was important to understand if the recording series resistance would be a confounding variable which itself affects AP latency, peak voltage, or FWHM. By demonstrating that none of these properties were strongly correlated to series resistance across our range of recordings (Spearman's Correlation Coefficient values of 0.433, -0.354, 0.395 respectively across n=23 neurons, and series resistances ranging from 12 MOhm – 49 MOhm), we can infer that data collected when looking at AMPA and GHK leak conductances would not be skewed by recording quality so long as our recordings were within those series resistance bounds- which they were.

3.5.2 GHK LEAK DID NOT AFFECT AP FWHM IN RECORDED NEURONS, BUT DROVE RMPS TO REVERSAL POTENTIAL

By imposing non- linear GHK leaks with increasing magnitude on putative pyramidal neurons in the PFC it was seen that there was no discernible effect on the FWHM. However, we did observe that the GHK leak worked- increasing the leak conductance drove the neuron resting membrane potential towards the reversal potential of the model.

It is also important to note that our dataset contained n=9 neurons. Though the null result was ubiquitous across our dataset, by increasing our sample size we could determine the effect of GHK leak on the AP FWHM with statistical power.

3.5.3 INCREASING AMPA CONDUCTANCE DECREASED AP PEAK VOLTAGE AND LATENCY

The final results of this chapter showed the effects of AMPA conductance on the AP latency and peak voltage; increasing the maximum conductance of the former decreased the latter two AP parameters. Quantitatively, the average decrease in AP latency across all neurons was 0.42 ms, 1.1 ms, and 0.8 ms for GHK leak conductances of 0 nS, 1 nS, and 5 nS- corresponding to a 21 % decrease, 65 % decrease, and 42 % decrease in AP latency respectively. Further, the average decrease in AP peak voltage was 7.1 mV, 2.1 mV, and 3.0 mV for GHK leak conductances of 0 nS, 1 nS, and 5 nS- corresponding to a 17 % decrease, 4.9 % decrease, and 7.9 % decrease in AP peak voltage respectively.

Crucially, these two parameters have an effect on synaptic release and hence understanding the effect of AMPA conductance, and analogously, charge transfer during an input event (be it an AMPA waveform or a photocurrent waveform) provides insights into connectivity mapping paradigms. For instance, based off these results it could be argued that maintaining consistent presynaptic photostimulation protocols (light power density, spot size, pulse duration) is paramount as it helps to mitigate variability in photocurrent charge transfer, and hence pre-synaptic AP peak voltage and latency. By reducing the variability in these two AP parameters, we mitigate the variability in synaptic release magnitude and timing- both of which are already inherently variable but have an effect on functional connectivity metrics such as post-synaptic response time and magnitude.

3.5.4 FUTURE DIRECTIONS FOR THE WORK IN THIS CHAPTER

The entirety of this chapter utilised single neuron patching. An interesting direction here would be to scale this up to dual-recording connectivity mapping, with pairing protocols utilising realistic AMPA conductances of varying maximum conductance. In this way one could begin to experimentally demonstrate the effect of charge transfer during a synaptic event on functional connectivity metrics such as connection probability, mEPSC rates in the post-synaptic neuron, and post-synaptic response timings.

In parallel to this, one could use Dynamic Current Clamp (DCC) to model photocurrents. This will be discussed further in Chapter 4, though was a planned experiment that unfortunately timing and circumstance left unfinished. One could in principle factor in membrane voltages, expression variability, opsin biophysics, light power density, spot size, and pulse duration in to DCC protocols which would allow us to rapidly assay the effects of these parameters on AP properties. Furthermore, scaling this to dual patching functional mapping as spoken about above, this could even yield data on how various photostimulation parameters could affect functional connectivity assays.

CHAPTER 4

DEVELOPMENT, CHARACTERISATION, AND VALIDATION OF A LIGHT PATTERNING MICROSCOPE FOR FUNCTIONAL CONNECTIVITY ASSAYS OF NEURONAL MICROCIRCUITS

4.1 ABSTRACT

To achieve single-neuron resolution functional connectivity maps of neuronal microcircuits using optogenetics, the photostimulation light used must be shaped with high spatial and temporal precision. Spatially, the light must be confined such that it precisely illuminates individual presynaptic neurons whilst avoiding any indirect actuation of neighbouring neurons and processes which may express opsin. Temporally, the light must be shaped such that it can reliably actuate action potentials in target neurons. To this end, I characterised and developed the light patterning capabilities of a microscope incorporating a Digital Micromirror Device (DMD) into its light path.

Firstly, by utilising an ultra-flat dichroic mirror with reflection and transmission windows optimised for our experimental plans, I was able to improve the homogeneity of photostimulation light across the addressable Field of View. Secondly, I validated the system's ability to generate arbitrary light patterns within the microscope's field of view

with micrometre spatial precision, millisecond temporal precision, microsecond jitter, and light spot power densities within and surpassing ranges cited for evoking action potentials in Channelrhodopsin-2 (ChR2) expressing neurons. All together, these steps demonstrate the microscope's ability to achieve single neuron precision many-to-one functional connectivity maps of neuronal microcircuits within specific experimental bounds.

Given these results I demonstrate single neuron precision photostimulation of Inter-Telencephalic (IT) neurons in acute brain slices. I show the range of photocurrents which can be evoked using different photostimulation parameters including spot size, spot location, light pulse duration, and light power. I compare the charge transferred over the course of photocurrent events using a range of light spot sizes and pulse durations to the charge transferred over the course of AMPA conductances known to reliably evoke action potentials in pyramidal neurons and demonstrated that the system could induce sufficient photocurrent charge transfer to generate action potentials in ChR2 expressing neurons using our particular transgenic model. Finally, the results of these validation steps helped determine the technical limitations of the microscope in terms of the spatial and temporal precision with which we can reliably photostimulate neurons, and by extension what scientific questions could be addressed with it.

4.2 INTRODUCTION

4.2.1 RATIONALE FOR DEVELOPING THE MICROSCOPE

Local functional connectivity assays of neuronal networks have in in the past relied on patch clamp electrophysiology which, as discussed Section 1.2, are limited in the number of neurons which can be studied at once [31]. Optogenetic approaches can help to bypass this limit by allowing optical access to potentially all neurons within a microscope's FoV. However, such experimental paradigms depend heavily on the transgenic strategy for expressing the opsin as well as the optical stimulation method.

In an ideal many-to-one optogenetic functional connectivity mapping paradigm where we photostimulate putative presynaptic neurons and measure the response from a single post-synaptic neuron, we would be able to precisely photostimulate presynaptic neurons without indirectly stimulating any neighbouring neurons or process which express opsin. This ensures any signal seen in the patch-clamped postsynaptic neurons can be more reliably correlated to and causally linked to the activity of the photostimulated presynaptic neuron. The difficulty in this precision stimulation is determined by several parameters: the spatial distribution of the photostimulation light, the light power density deliverable to photostimulation volume, the temporal profile of photostimulation light, and finally the spatial sparseness or density of opsin expression in neurons and processes. As the latter parameter of opsin expression profiles involves an inherent biological variability, understanding the capabilities and limitations of our optical system in reference to the former factors is crucial. The knowledge would firstly validate our ability to optically map the functional connectivity of IT neurons. Secondly, it would guide developments to our system to improve its functionality with respect to our experimental goal of local functional connectivity mapping of neuronal microcircuits. Finally, the knowledge helps us to understand the range of scientific questions we can ask of our specific animal model (described in Section 5.2.2) when using this system.

Spatial precision of photostimulation light

The spatial precision of photostimulation patterns is paramount when considering two perspectives. First, given the expansive, tortuous, and overlapping nature of neuronal circuitry it is easy for extraneous light to photostimulate any neighbouring neurons and on neuronal processes. This unintended perturbation of network activity is a confounding variable which, in the context of functional connectivity mapping, could invalidate the results of an experiment as there would be extraneous activity diluting either/both the input (e.g., photostimulating a target putative presynaptic neuron as well as a neighbouring opsin expressing neuron), or the signal (putative post-synaptic activity). On another note, being able to reliably change the photostimulation volume cast on to a neuron allows the control of photocurrent magnitude as varying areas of cell membrane hosting expressed opsin can be illuminated. This in turn means one is able to vary the magnitude of summed photocurrent, allowing more precise and reliable control of neural activity. For instance, one could attempt to maximise the spiking probability of a target neuron by maximising the photostimulation volume such that it included the majority of the cell soma, but not more such that extraneous neurons are optically perturbed.

Temporal precision of photostimulation light

The temporal precision with which photostimulation patterns can be cast on to a neuron is also important as the duration that an opsin expressing neuron is illuminated determines- along with the opsin biophysics and the neuron’s specific physiology- how much charge transfer there is across the neuron’s plasma membrane. Subsequently, this and the photostimulation light volume work in concert to determine the neuron’s spiking probability and activity once targeted.

Overall rationale

Overall, in functional connectivity mapping paradigms having spatially and temporally precise, but also reliable, control of light when perturbing putative pre-synaptic neurons is critical. Keeping consistent control illumination strategies means fewer confounding variables when studying complex biological systems with inherent variability. Indeed, things like variable synaptic release following an AP, background network activity, cell health, desensitisation of pre- and post- synaptic terminals, and opsin expression variability are all confounding variables which must be considered and mitigated where possible. Herein lies the impetus of this chapter: to develop our microscope such that we are optimising it's light patterning capabilities, to carefully characterise what it is capable of, and finally, to validate its use for functional connectivity mapping of IT neurons in the PFC.

4.2.2 EXPLORATION OF THE OPTICAL HARDWARE

The optical system I was working on was a fixed-stage upright microscope (Olympus and Scientifica SliceScope), modified to include a DMD micromirror device (Mightex Polygon400) in its optical path. A full discussion of optical systems for optogenetics experiments is discussed in Section 1.3.3. Figure 4-1 shows a schematic of our system.

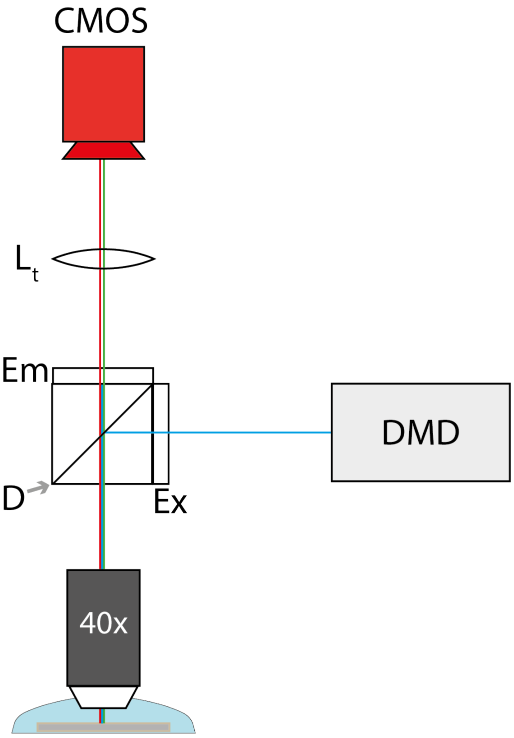

***Figure 4-1 Light patterning optical system**. CMOS = Thorlabs 8955MU; Lt= 180 mm tube lens; D = Chroma T525lpxr ultra-flat 2 mm thick Dichroic, or unmarked proprietary dichroic (Mightex); POLYGON = Digital Micromirror Device (Mightex Polygon400), which contained a blue (490 nm central wavelength) LED, a red (590 nm central wavelength) LED, and a micromirror device for sample illumination and pattern generation respectively; 40x = Olympus 40x water immersion objective lens, which could be switched for a 4x objective. Ex and Em are mounts capable of housing excitation and Emission filters, respectively. An IR light source (coolLED pE-100, 770 nm, not shown), transmits IR light through the bottom of the sample to image the sample on to the camera via the infinity corrected objective and tube lens. Note, within the DMD system was presumably a 180 mm lens used to relay light patterns from the internal micromirror array down to the objective lens. The exact details of the optics were not available to us from the supplier.*

There are two combined light paths in the system. First, IR light is transmitted through the sample from below via an LED (cooled pE-100, 770 nm). The infinity corrected objective lens (Olympus 40x) images this light from its focal plane onto the camera sensor (Thorlabs 8955MU) via a 180 mm focal length tube lens. The camera itself was controlled using Micromanager[116]. The second path begins at the DMD but is not as readily describable.

The DMD system was a proprietary piece of hardware (Mightex) with the internal optical components being trade secrets. Hence, aside from a few details which are described below, it could almost be treated as a black box as information on any potential opto-mechanics, filters, LEDs, or other optical elements were unavailable to us. Certain features of the system can infer a basic understanding of the DMDs inner workings, however. In its simplest form, the second light path can be described as such: red or blue illumination light (490 and 590 nm respectively) from separate LEDs within the system is cast on to a micromirror array, which as described in 1.4.3, directs light either towards or away from the sample. If towards, the light is presumably imaged at infinity using a 180 mm focal length relay lens. The reasoning for this is that the DMD light path is integrated below the tube lens in Figure 3-1, and hence the light needs to be adjusted to be refocussed at the sample plane with the infinity corrected objective. A dichroic mirror then either transmits or reflects the light towards the sample plane based upon its transmission and reflection windows. Finally, the light pattern is then imaged on to the sample plane with the objective, illuminating target regions of the sample within the microscope's FoV. Finally, if any fluorescence is excited within the sample, this is imaged on to the camera sensor the same way as the IR light is.

4.2.3 SOFTWARE CONTROL OF SPATIAL AND TEMPORAL LIGHT PATTERNING

Control of the light patterning functions of the microscope can be split in to two domains: temporal control and spatial control. Figure 3-2 shows a schematic of the hardware and software control.

Spatially, Polyscan (Mightex, proprietary software) was used to generate arbitrary patterns of light within the camera's Field of View (FoV). These patterns would then be uploaded to the Digital Micromirror Device (DMD, Mightex Polygon400) and stored on the system until triggered by the temporal pattern control. Signal (V6.05b, Cambridge Electronic Devices) was used to generate temporal waveforms which were digitised by the Power1401 hardware (Cambridge Electronic Devices), which in turn triggered the

DMD to cast the spatial patterns onto the sample plane of the microscope. Upon triggering, the DMD would send feedback to the Power1401 and in turn, Signal, to confirm the pattern was successfully cast thus allowing validation during experiments.

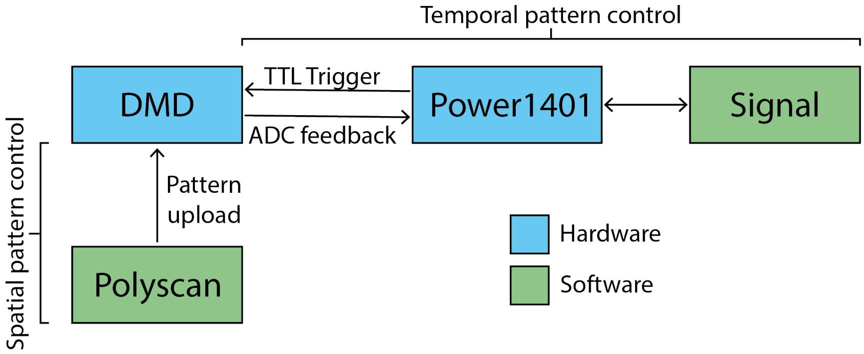

***Figure 4-2 Light patterning hardware and software control**. Control of the optical system was split into the spatial patterning of light and the temporal patterning of light. Spatially, Polyscan (Mightex, proprietary software) was used to generate arbitrary patterns of light within the camera's Field of View (FoV). These patterns would then be uploaded to the Digital Micromirror Device (DMD, Mightex Polygon400) and stored on the system until triggered by the temporal pattern control. Signal (V6.05b, Cambridge Electronic Devices) was used to generate temporal waveforms which were digitised by the Power1401 hardware (Cambridge Electronic Devices). These waveforms triggered the DMD to cast the spatial patterns light patterns with corresponding temporal profiles onto the sample plane of the microscope. Upon triggering, the DMD would send feedback to the Power1401 and in turn, Signal, to confirm the pattern was successfully cast. This provided me with a validation that the system had been triggered during and post- experiment.*

Polyscan utilised a Graphical User Interface (GUI) to manually 'draw' patterns on to the addressable areas of the microscope field of view. It would then perform some calculations (be it simply directing micromirrors towards the sample or away depending on the defined pattern or something more sophisticated- this information is not known and lives beneath the veil of a trade secret).

4.2.4 THEORETICAL LIMITS TO OUR LIGHT SCULPTING CAPABILITIES

Considering the temporal domain, the Polygon DMD (Mightex, Polygon400) used in our system has a quoted frame rate of 4000 frames s^{-1}. In other words, the DMD can in principle change the spatial profile of light cast to the sample plane of the microscope every 250 µs. Discounting any delays in signalling between the Polygon software and hardware, this essentially defines the theoretical limit to the temporal precision of pattern generation that our system is capable of.

With respect to the spatial domain, the pixel dimensions of the DMD were quoted at 16 µm x 16 µm. The objective lens used in the system had a magnification of 40x which means that considering no other magnification in the system and ignoring any optical aberrations, the smallest spot we can cast down to the sample plane was 0.4 µm x 0.4 µm in the lateral extent. However, aberrations in the systems exist, and the wave nature of light describes a broadening of light spots formed from rays emanating from the same point source; these rays will constructively interfere with one another if the difference in their path length is less than half their wavelength. So, to calculate an approximate theoretical limit to the minimal light spot we can cast down to the focal plane of our microscope, we must consider both of these factors.

It can be shown that when considering a flat wavefront passing through a circular aperture (an ideal case of our light patterns passing through the back of our objective) the broadening of light spots formed from a single point source can be described as an Airy disk. The width of this disk can be calculated by Equation 4-1:

$$\mathrm{D} = \frac{1.22 \cdot \lambda}{\theta}$$

Equation 4-1

Where D is the width of the disk, also known as the Abbe limit, λ is the wavelength of light used, and θ is the angular resolution of the system. The central wavelength of our blue

LED is 490 nm, and the NA of our objective is 1. Altogether, this means that in an ideal case of a flat wavefront passing through our objective, free from any optical aberrations, we could theoretically focus individually resolvable light spots in the sample plane with a lateral resolution of 0.245 µm x 0.245 µm. This is smaller than the theoretical spot cast by pointing an individual mirror in the micromirror array down at our sample, hence we can conclude that our system is not diffraction limited. Instead, we must turn our attention to aberrations in the system.

This now presents an engineering limit of this project. The Polygon system, as discussed, is a proprietary piece of hardware. The internal optics were trade secrets meaning it is difficult to ascertain or mitigate any aberrations which may be caused by its internal optics. Hence, the only optics we can consider in this regard are the two we have control over: the dichroic mirror and the objective itself.

As a final measure of spatial limits to our light sculpting capability, we consider the axial extent of our photostimulation patterns. As we are using single photon illumination strategies, there is limited axial confinement and hence a large axial spread of light. So, even with the smallest lateral spot we can generate, our axial spots size will likely extend far past the size of a neuron. This will create a significant limitation to functional mapping paradigms and must be quantified where possible.

4.2.5 PLANNED OPTIMISATIONS TO THE OPTICAL SYSTEM

Two attributes of the microscope that were targeted for improvements were the camera’s FoV and the homogeneity of photostimulation light in the sample plane. With respect to the FoV, it was reasoned that increasing the area of an acute brain slice that we could visualise without laterally moving the microscope stage would mean that we could rapidly identify IT neurons (or more generally, any opsin expressing neuron) within the FoV. From this we could rapidly generate photostimulation patterns- and as a consequence rapidly photostimulate larger sets of putative presynaptic neurons.

The second targeted optimisation was the dichroic mirror. From the get-go, there was limited, and arguably factually incorrect, details provided about its optical properties from the supplier. We were simply told that it had a 'transmission window of 380 nm – 750 nm', which was nonsense as it clearly reflected blue light (490 nm) down to the sample plane. Furthermore, the dichroic was significantly tarnished. Practically, the dichroic mirror is a crucial optic in the system as it's optical transmission or reflectance windows control the flow of certain bandwidths of light through the light path. Uncertainties in its optical properties lead to uncertainties in the optical stimulation paradigms; tarnishing of the mirror would cause inhomogeneities and aberrations in the light path. These aberrations would manifest as losses of spatial precision in light patterns cast to the sample plane, and distortions of images taken from the sample plane by the camera. Such distortions would hinder our ability to identify opsin expressing neurons and craft light patterns which fit within the soma diameter. Hence, ensuring this optic was optimised for the task at hand was of high priority.

4.2.6 SPECIFIC CHAPTER AIMS

The specific aims of this chapter are as follows:

1) Identify and address areas of improvement to the light patterning capabilities of our optical system. Two areas of improvements which were targeted were the dichroic mirror and the microscope camera.
2) To characterise the light patterning capabilities of our optical system in both the temporal and spatial domains. Specifically, I wanted to ascertain that we could reliably generate photostimulation spots within the size of a single IT neuron cell body (~10 μm), at light power densities and light pulse durations necessary to induce action potentials.
3) To experimentally verify that we could generate photocurrents in our particular animal model using the optical system, and moreover verify that mapping the functional connectivity of IT neurons in the PFC using our system was feasible-

and if so, to what limitations. Where possible, all of the above was to be quantified and compared to literature values of photostimulation parameters used to evoke action potentials in neurons.

4.3 MATERIALS AND METHODS

Broadly speaking, this Materials and Methods section can be split in to two halves. The first half spanning Sections 4.3.1-7 details the optical system characterisation and control; the second half spanning 4.3.8-14 details the validation of the system.

With respect to the electrophysiology used this chapter: animal and animal care information is detailed in Section 2.1. The ChR2 transgenic strategy and stereotaxic viral injection strategy are detailed in Section 2.2.2. Solutions used for electrophysiology and tissue preparation are described in Sections 2.3.4-6; tissue slice preparation Section 2.4; and whole-cell electrophysiology procedures in Section 2.5.1. Note, the intracellular solution used in this chapter was the K-Gluconate based solution. Further, all electrophysiological recordings were taken from putative pyramidal neurons (as determined by discernible cell morphology and approximate anatomical region) within the Prefrontal Cortex (PFC) of wild-type animals. Finally, intracellular solutions were filled with 1 mg biocytin to attempt to reconstruct neuronal morphology for future imaging and structural connectivity assays (filling and slice preservation protocols are described section 4.3.10-11).

4.3.1 SPIN COATING RHODAMINE-6G SLIDES

5 mg of Poly(methyl methacrylate) (PMMA, Merck) was first dissolved in to 100 ml ethyl-acetate (Merck) a day ahead of time; the PMMA takes time to fully dissolve. The next day, 5 mg Rhodamine-6G (Merck) was dissolved in to 10 ml of the above solution, turning it bright orange. This solution was then dripped on to a 10 mm diameter

glass coverslip using a syringe fitted with a 25 mm diameter, 1 µm pore size syringe filter (Pall Acrodisk, Merck). This coverslip was then placed in the centre of a spin coater (P6700 Mark 1, Spincoater) and spun using the following parameters which were found to create a uniform layer of the Rhodamine- 6G:

RPM 1	600
RAMP 1	5
TIME 1	10
RPM 2	4000
RAMP 2	10
TIME 2	100
RMP 3	6000
RAMP 3	20
TIME 3	30
RAMP 4	10

Table 4-1 *Spincoater parameters for Rhodamine-6G slide preparation.*

Once the spinning procedure was complete, cover slips were stored in a 4°C fridge until needed.

4.3.2 GENERATING SPATIAL PHOTOSTIMULATION PATTERNS

Spatial patterns of light were generated using Polyscan (Mightex, proprietary software). Its functionality was as follows: the signal from the camera was fed into the software via USB 2.0 collection. This image feed was then displayed within the Graphical User Interface (GUI), upon which patterns could be 'drawn' on. In practice, the user (me) drew on circles and other simple vector images like frame-filling rectangles for full FoV illumination strategies. Polyscan then processed these vectors behind the scenes to turn the required mirrors within the DMDs micromirror array toward or away from the sample. Figure 3-3 shows a screenshot of the Polyscan GUI.

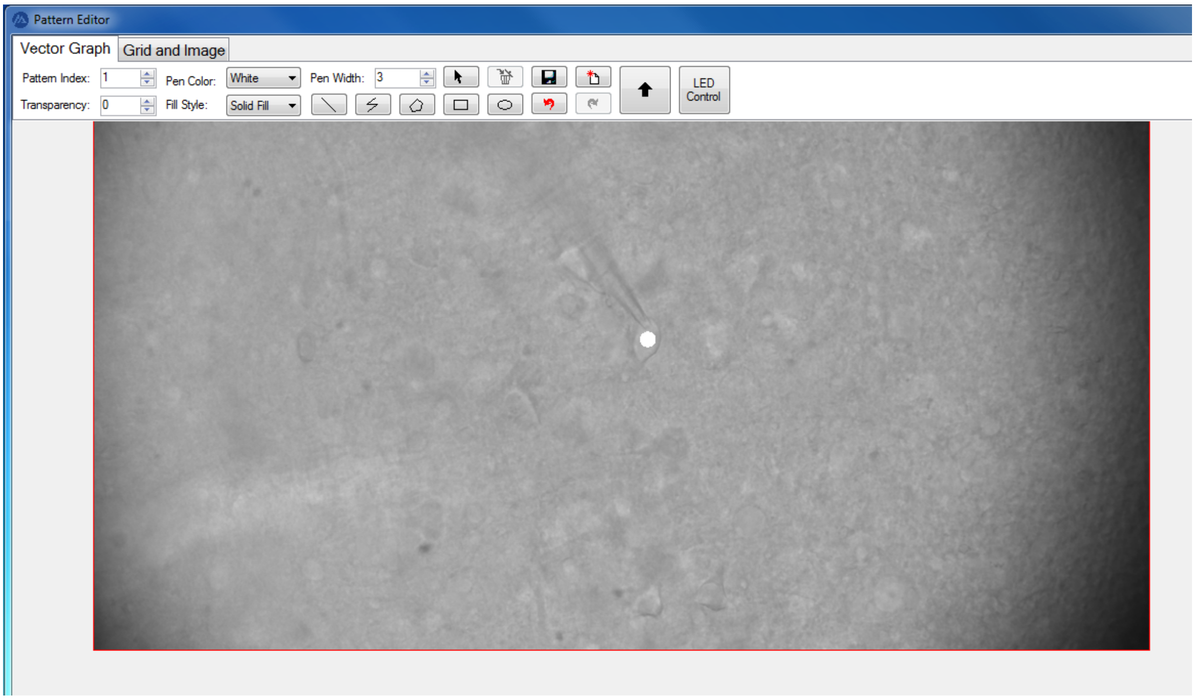

Pattern Index: 1
Transparency: 0
Pen Color: White
Fill Style: Solid Fill
Pen Width: 3

***Figure 4-3 Polyscan GUI**. Control of the spatial profiles of photostimulation light was achieved using the Polyscan (Mightex, proprietary software). This screen shot shows the general use: the IR feed from the microscope was fed into the system, and light pattern could be drawn as simple vector images on top of this feed. The software would then interpret this, control the DMD within the Polygon (polygon400, Mightex) hardware, and cast the required light pattern down to the sample plane of the microscope. The small white dot drawn towards the centre of the Field of View above represents a 5 µm light spot to be cast down on to a real sample.*

4.3.3 TEMPORAL LIGHT CONTROL

Once patterns were generated using the Polyscan GUI, they were uploaded to the Polygon device (polygon400, Mightex) via a USB 2.0 connection. Desired patterns were interweaved with empty patterns which served as 'off' switches for the previous light desired pattern. To control the temporal patterning of these profiles, sequential TTL triggers were generated in Signal (V6.05b, Cambridge Electronic Devices) with timings pertinent to that specific pattern; each specific pattern had an 'on' pulse and an 'off' pulse separated by the duration that specific light patterning needed to be incident on the sample (which I define as the light pulse duration), and each of these pairs were spaces at the required duration away from one another to achieve whatever arbitrary inter-pulse time needed. Once these temporal control waveforms were defined in signal, they were sent directly to the Polygon.

4.3.4 LIGHT POWER CONTROL

The power output of the Polygon device was controlled using the Polyscan GUI. The power levels were in arbitrary units from 0 – 1000. The calibration of this scale is shown in section 4.4.5. Before uploading any light patterns to the polygon, the power level was set and uploaded alongside the patterns.

4.3.5 SPATIALLY CHARACTERISING LIGHT PROFILES IN THE MICROSCOPE FOCAL PLANE

Spatial light patterns were imaged on to the surface of a rhodamine-6g spin coated slide and imaged using the system described in 3.2.2. Images were taken using ImageJ[117]. The polygon light power was set manually to ensure the camera sensor was not over saturated, and this was quantified using the camera sensor histogram on the micromanager[116] interface. Due to small heterogeneities in the spin-coating process, 5 images were taken at the same power level and averaged to obtain the final image used for analysis. Image averaging, image plotting, and intensity cross-section plotting was all done using custom python scripts.

4.3.6 TEMPORALLY CHARACTERISING LIGHT PROFILES IN THE MICROSCOPE FOCAL PLANE

To characterise the temporal profile of light pulses a custom photodiode circuit was made and utilised, shown in Figure 4-4.

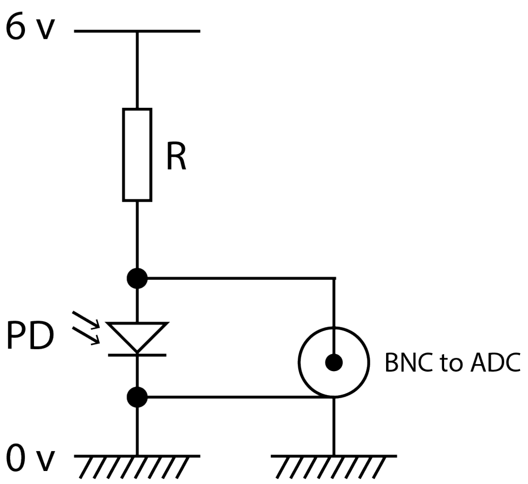

__Figure 4-4__ The photodiode circuit used to characterise the temporal profile of light patterns. PD = photodiode, R = resistor, BNC to ADC = BNC output to ADC digitiser. The photodiode would be placed at the sample plane of the microscope.

Between a potential difference of 6V, a 100 Ohm resistor was wired in series with a photodiode (BPX65, Centronic). Across the photodiode was a BNC to ADC connector; this output measured any potential changes across the photodiode when responding to incident light.

To measure the temporal profile of light pulses, the photodiode was placed at the approximate focal plane of the objective. Then, light patterns controlled as described in 4.3.3 were cast on to the diode, with the BNC output measuring any changes in voltage across the diode. The signal from the BNC was digitised by a Power1401 digitiser (Cambridge Electronic Devices) at 50 kHz, and then analysed using custom python scripts which matched the light pattern output from the DMD with the signal obtained via the photodiode.

4.3.7 POWER MEASUREMENT AND CALIBRATIONS

Measuring the power was achieved by placing a power meter (PM100D, Thorlabs) at the approximate focal plane of the microscope objective- as discerned by focussing light on to the sensor of the power meter itself. In the case of simple power measurement, the desired pattern was cast on to the power meter and its power read out.

For the case of calibration, the range of polygon power levels (0-1000) were cast down to the power meter sensor, each time measuring the power whilst the sensor was continuously illuminated. Care was taken to emulate lighting conditions on the day of an experiment by turning off most ambient light sources where possible. This procedure was repeated for 5 μm spots, 10 μm spots, and full Field of View photostimulation patterns, with this set of conditions repeated using both the old (proprietary) and new (T525lpxr, Chroma) dichroic mirrors. These specific patterns were chosen as they were the patterns used for optogenetic experiments.

4.3.8 LIVE SLICE IMAGING: LOCATING OPSIN EXPRESSING NEURONS WITH GFP

A crucial aspect of this project was identifying opsin expressing neurons for functional connectivity mapping. With this in mind, the retro- viral construct we selected (pAAV-Syn-ChR2(H134R)-GFP, full methodology detailed in 2.2.2) contained a ChR2-GFP payload. Hence, upon transfection with the virus neurons would express ChR2 which had GFP conjugated to it- the latter of which we could image using our system. To find opsin expressing IT neurons in the PFC I would first navigate to the rough anatomical region using IR imaging and a low magnification (4x) objective. Once I had done this, I would cast full FoV blue light patterns down to the sample plane, using powers lower that 1 mW. This upper limit was empirically determined as either the point which maximised the camera saturation at the brightest pixels or allowed clear visualisation of the GFP in transfected neurons- which ever of the two situations occurred first. In practice, opsin expression was highly variable, and it was often the former scenario which came first. Further, to limit the effect of excitotoxicity arising from prolonged exposure to blue light induced photocurrents, attempts were made to minimise the light power cast to the sample as soon as possible: immediately after neurons were identified the blue light was switched off.

Once a GFP signal was found, I attempted to find the healthiest looking GFP positive neurons (as judged by switching between IR imaging and GFP imaging whilst looking for tell-tale signs of cell health (no puckering, no visible nucleus, a ‘pillow-y’ look- again all empirically and subjectively determined based upon my own experience). These cells were then targeted for patching and photostimulation experiments.

4.3.9 PHOTOSTIMULATION CHARACTERISATION PROTOCOLS

Once opsin expressing neurons were identified, they were first patched and left in voltage clamp as described in Section 2.5.2. The neuron itself was then focused axially to ensure it was in the focal plane of the microscope. Further, the targeted neurons were aligned centrally (with respect to the lateral, focal plane) in the addressable area of the microscope field of view. This central point was marked using the Region of Interest (ROI) manager in imageJ, and all target neurons were subsequently aligned to this point. If the recording was deemed healthy (recording quality was constantly monitored during this characterisation process; leak currents and series resistance were checked periodically between photostimulation epochs), characterisation protocols were run in parallel to efficiently retrieve data from the neuron:

Soma targeted photostimulation characterisation

First, soma- targeted photo stimulation spots of 5 µm and 10 µm were cast on to the neuron, with pulse durations in the set of 2, 3, 5, 7, and 10 ms. That spatial profile of the light was defined as described in 4.3.2, and the temporal profile was generated as described in section 4.3.3. In the first instance, a 5 µm spot was used, and in the second, a 10 µm spot was used. Pulse durations were randomised using the Signal U for both instances. This first characterisation step aimed to confirm opsin expression in lieu of reliable GFP signal and understand how pulse duration and light spot size affect photocurrents in opsin expressing IT neurons. The maximum polygon power of 1000-

corresponding to a power density of 0.11 $^{\mu W}/_{\mu m^2}$ or 0.125 $^{\mu W}/_{\mu m^2}$ for a 10 µm or 5 µm spot respectively- was used throughout, save for the case of the light power characterisation protocol described below.

Lateral spatial characterisation:

Once soma targeted photostimulation data were collected, I then sought to understand how lateral displacement of the photostimulation spots affect photocurrents in target neurons. To this end, rather than generating photo stimulation spots with the required lateral displacements relative to the neuron, I chose to move the microscope stage and hence neuron relative to the centrally aligned ROI. This is discussed further on in this chapter, but the brief reason why I chose to characterise this way was experimental simplicity in the face of poor opsin expression profiles and cell health, technical issues with the microscope, and maintaining the exact same light spot characteristics for each laterally displaced data point.

So, the stage was displaced in 5 µm increments away from the target neuron. The map of photostimulation spots is shown below in Figure 4-5.

At each lateral photostimulation location (1-9 in Figure 4-5), a 5 µm photostimulation spot was cast with the full set of pulse durations used for the soma-targeted photostimulation characterisation (2, 3, 5, 7, and 10 ms). This particular characterisation step was designed to yield data on the lateral spatial confinement of our photostimulation spot, the spatial precision needed to evoke photocurrents in single neurons, and the temporal profile of light one could use to mitigate any off-target photocurrents. Throughout this step, the maximum polygon power of 1000- corresponding to a power density of 0.11 $^{\mu W}/_{\mu m^2}$ or 0.125 $^{\mu W}/_{\mu m^2}$ for a 10 µm or 5 µm spot respectively- was used.

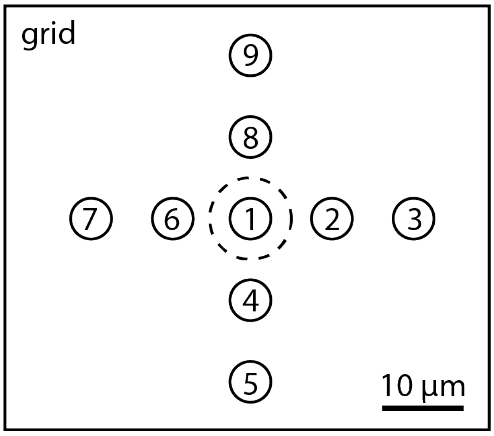

***Figure 4-5 Optogenetic spot patterning grid**. To test the efficacy of precise spatial photostimulation using our system, light spots were sequentially cast to a sample with increasing lateral distance from the grid centre. The grid was centred on a patched ChR2 expressing neuron, and each circle represents a photostimulation spot; number spots show 5 µm spots, and the dashed circle represents a 10 µm spot. Spot 1 was centred on the target neuron. Scale bar = 5 µm.*

Axial photocurrents characterisation

Our photostimulation light was collimated single photon LED light. Hence, we knew *a priori* that there would be limited axial spatial confinement of our light patterns. Nevertheless, I sought to demonstrate this and see if there were limits with which we could axially displace our photostimulation spots whilst still evoking photocurrents as intended. This would also yield information on the axial extent of our patterns so we could attempt to avoid targeting any neurons which had other opsin expressing neuron in the same axial column of light.

To test this, photostimulation spots were targeted to the cell soma as described above for the soma-targeted characterisation. Then, the same photostimulation protocol was run as above, this time whilst axially displacing the neuron by refocusing the microscope such that the neuron was axially displaced from the focal plane of the objective. This was done such that the focal plane was at the surface of the brain slice, at the neuron itself, and -100 µm below the neuron. The latter number was selected as this was essentially the deepest one could image our slices whilst still resolving neurons- any deeper and tissue scattering of light became predominant for both IR light and GFP fluorescence, and single cell optical functional mapping would not be possible. This is further explored in the discussion section of this chapter. Throughout this step, the maximum polygon power of 1000- corresponding to a power density of 0.11 ${}^{\mu W}/_{\mu m^2}$ or 0.125 ${}^{\mu W}/_{\mu m^2}$ for a 10 µm or 5 µm spot respectively- was used.

Light power photocurrent characterisation

The final characterisation protocol was focussed on the relationship between light power (and hence light power density) and photocurrents. This was done using the same soma-targeted strategy as above but only using a 5 µm spot, and this this varying the polygon light power output from 0-1000 (0 ${}^{\mu W}/_{\mu m^2}$ - 0.125 ${}^{\mu W}/_{\mu m^2}$). This was done to gain and insight as to how one could modulate photocurrent magnitude by modulating light pattern power density.

4.3.10 BIOCYTIN FILLING PROTOCOL

To enable post-experiment reconstruction of neuron morphology, 1 mg/ml of biocytin (B4261, Merck) was dissolved into internal solution of any variation described in Section 2.3.4. Biocytin salt was added to pre-made aliquoted internal solution immediately after defrosting on the day of experiment, and then thoroughly shaken to ensure proper dissolution of the salt. Once this was confirmed by visual inspection, I used the internal for electrophysiology experiments as normal. This allowed the biocytin could naturally dialyse with the intracellular contents of the neuron during whole-cell recordings.

4.3.11 SLICE STAINING AND FIXING PROTOCOL.

After whole-cell recordings of neurons using biocytin containing internal solutions, the recording pipette was slowly withdrawn to reseal the cell. The brain slice was then then immediately removed from the recording chamber and placed in 4%PFA/96% PBS which was itself stored in a 4°C cold room. After at least 24 hours, slices were washed three times in PBS before being immersed in a PBS solution containing 0.5% Triton-X (Merck) and 0.5% streptavidin-conjugated Alexa-594 (S11227, ThermoFisher Scientific) for 3-4 hours. The Triton-X permeabilised the cell membranes within the entire slice and the streptavidin bound to the biocytin. The slice was finally washed 3 times with PBS and mounted between a glass slide and coverslip with DAPI Vectashield fluorescent mounting medium (H- 1000, Vectashield®).

Note, at each stage individual slices were placed in a chamber of a 12-well plate containing approximately 300 μl of the relevant solution. Transferring slices between solutions was done with the soft end of a fine paint brush, and washing the slices entailed emptying the extra solution from the chamber using a Pasteur pipette and replacing it with PBS- each time gently shaking the well plate.

DAPI was chosen to stain the nuclei of all cells within the brain slice, and Alexa-594 was chosen as its fluorescence profile was spectrally separate from GFP meaning we could in principle image both ChR2-GFP expressing neurons as well as the biocytin filled neuron. This allows the opportunity for structural connectivity mapping and is discussed further in 1.3.1.

4.3.12 FIXED SLICE CONFOCAL IMAGING

Fixed slices were imaged using a Leica SP8 Inverted confocal microscope (Facility for Imaging by Light Microscopy (FILM), Imperial College). This system was capable of imaging the DAPI, GFP, and Alexa-594 giving us multi-spectral images of our slices. Please note, imaging was done with the help of Dr David Gaboriau, a FILM Microscopy Specialist.

4.3.13 REGISTERING IR AND CONFOCAL IMAGES FOR PHOTOSTIMULATION SPOT LOCALISATION

Figure 4-6 shows the stages of identifying and characterising the photostimulation capabilities of our system. In the first instance, neuron morphology was ascertained using IR and GFP imaging under our microscope (Figure 4-6 a and b). The dashed black line represents the inferred morphology of the neuron soma, the rectangular grid represents the same grid in Figure 4-5, added to scale. This inferred morphology was then rotated and scaled along with the grid such that the dashed line matched the maximum intensity z-projections shown in Figure 4-6 c and d. These z-projection images were the confocal images of the same neuron patched in Figure 4-6 **a** and **b.** In practice, this registration process was manual and done using Illustrator (2022, Adobe). Logically, as all images are of the same coronal slice, with the imaging light (optical axis) perpendicular to the slice surface, this process should yield good registration results. However, I note the subjectivity in inferring neuron morphology and the role that tissue deformation occurring during the slice preservation may have on this result.

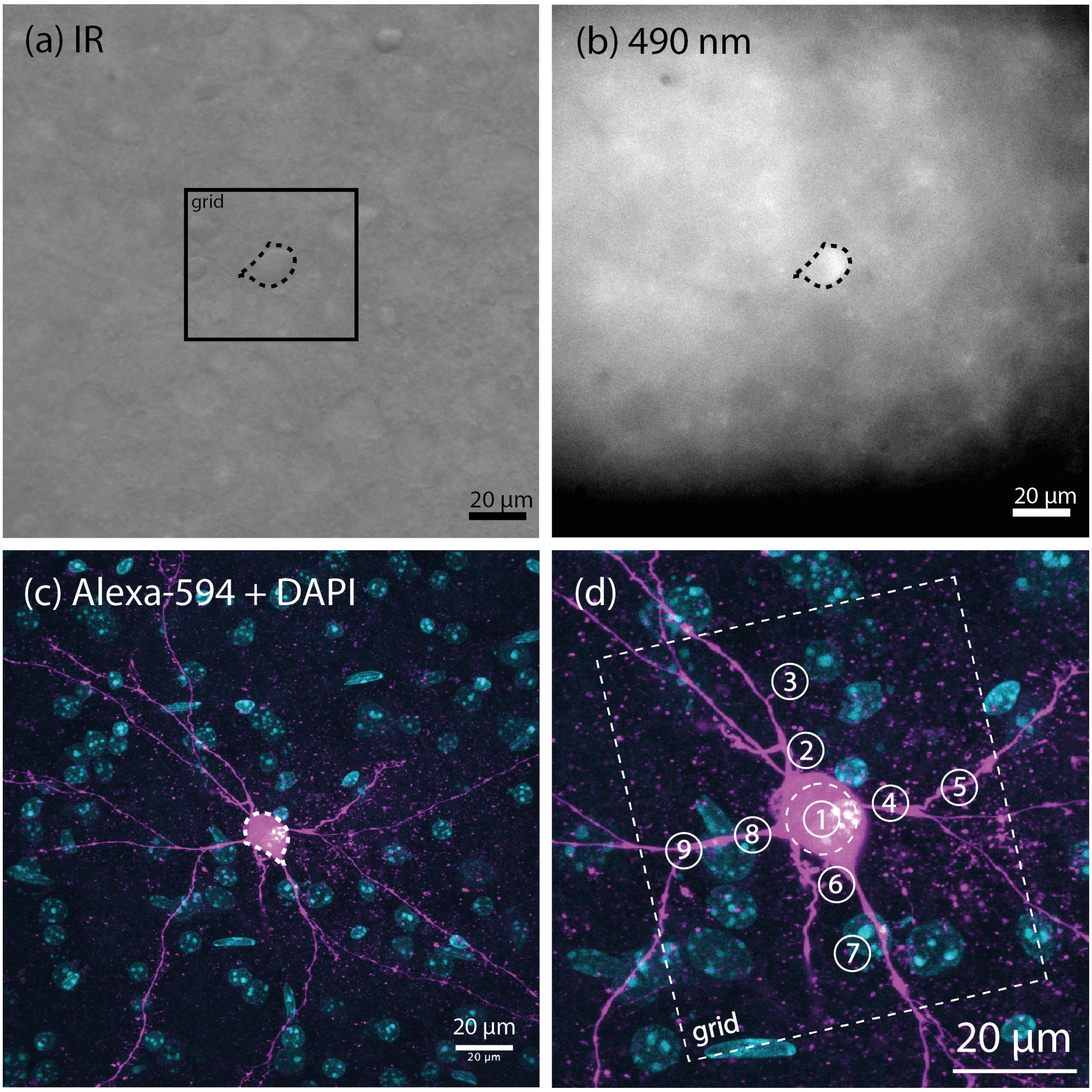

Figure 4-6 ***Lateral light spot placement map for photocurrent characterisation of ChR2 positive neurons****.* ***a*** *IR and* ***b*** *490 nm (blue-channel) images of a ChR2 expressing neuron taken using our system during photostimulation experiments. The contrast in* ***b*** *was adjusted in attempt to highlight the GFP signal in the soma of the target neuron.* ***c*** *and* ***d*** *are maximum intensity z-projection confocal images taken post-experiment showing an overlay of Alexa-594 (magenta) and DAPI nuclear staining (cyan). Precise imaging methodologies are outlined in section 4.3.12. The labelled grid in* ***a*** *and* ***b*** *represent the same grid in Figure 4-5, to scale. The dashed outlines in a and b highlight the neuron soma- the geometry and orientation of which were used to align the grid in* ***d*** *post-experiment to map photocurrent induced by casting spots to different map locations. All images from this figure are of the same Inter-Telencephalic Neuron in the Prefrontal cortex. All scale bars 20 µm.*

4.3.14 DATA ANALYSIS

I analysed all images and electrophysiological recordings in this chapter by writing custom python scripts for each experiment.

4.4 RESULTS

4.4.1 ARBITRARY SPATIAL PATTERNS OF LIGHT CAN BE GENERATED USING OUR SYSTEM

The first step towards validating the system for our needs was to demonstrate that arbitrary light patterns could be generated in the microscopes field of view. By generating patterns within the Polyscan GUI and casting them to the sample palm as described in section 4.3.2, we were able to ascertain that any pattern could be generated successfully. Figure 4-7 shows this result.

The next step was to replace the dichroic mirror to improve the spatial precision and homogeneity of light cast down to the sample plane.

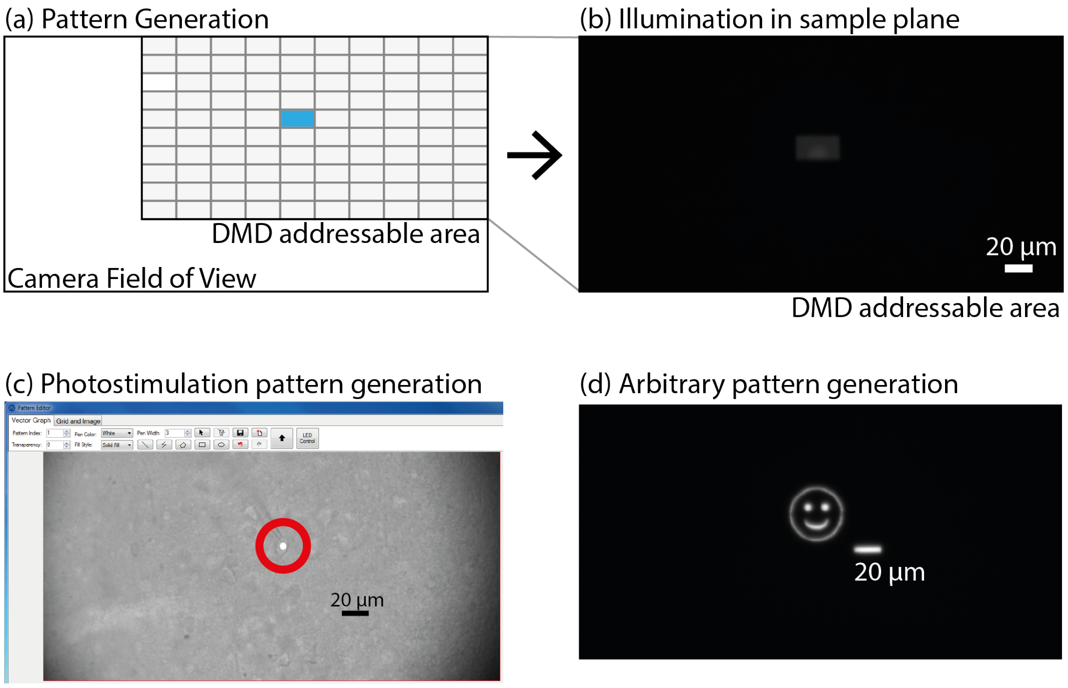

Figure 4-7 Arbitrary spatial patterns of light can be generated using our system. *Spatial patterns can be arbitrarily generated within the Digital Micromirror Device's addressable area, itself a sub-area of the microscope's Field of View (FoV).* ***a*** *The addressable area of the DMD was split in to a 10 x 10 grid, with each node being 19.5 µm x 34.5 µm (grey) and an example node (blue) was cast to the sample plane.* ***b*** *The example node from in* ***a*** *imaged using a fluorescent (spin-coated Rhodamine-6G) slide in the sample plane of the microscope.* ***c*** *The Guided User Interface (GUI) within Polyscan which is used to generate spatial light patterns in the microscope sample plane. In this example, an IR feed of an acute brain slice in the sample plane is fed in to Polyscan, and a 5 µm spot (white, circled in red) was drawn on top of a patched neuron and cast to the sample using the tools within the GUI.* ***d*** *Arbitrary spatial patterns can be generated and cast to the sample plane. All scale bars = 20 µm.*

4.4.2 SELECTION OF A NEW DICHROIC MIRROR BASED UPON EXPERIMENTALLY RELEVANT OPTICAL WINDOWS

To ensure the correct optic was chosen when replacing the dichroic mirror, I took careful consideration of the optical spectra involved in our experimental plan. We would be using blue light (specifically with a central wavelength of 490 nm), and casting that down to the sample via the dichroic to both photostimulate ChR2 neurons and excite GFP fluorescence. Hence, the dichroic would need to be reflective at this wavelength.

However, to visualise the GFP conjugated to the ChR2 (and hence opsin expressing neurons) the dichroic would also need to be transmissive for the emission spectrum of GFP. Figure 4-8 shows the relevant optical spectra for our experimental plans, as well as the chosen dichroic transmissivity (and by extension, reflectivity).

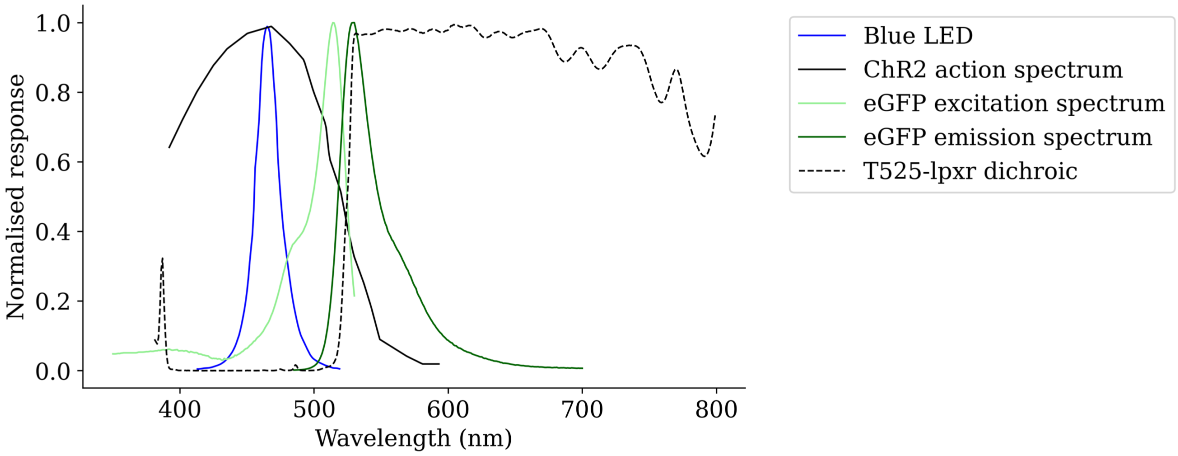

Figure 4-8 Selection of a new dichroic mirror based upon relevant optical windows*. Taking in to consideration the spectrum of light emitted by our blue LED (blue curve), the action spectrum of ChR2 (black curve), and the excitation and emission spectrum of eGFP (conjugated to the ChR2 used for optogenetic mapping, light and dark green curves respectively), a new ultra-flat dichroic (dashed black line, T526-lpxr, Chroma) was selected which reflects the blue excitation light towards the sample plane whilst allowing transmission of the eGFP emission spectrum towards the camera. This configuration allowed the visualisation of ChR2 positive neurons within our microscope's Field of View. On this plot, the normalised response for the dichroic represents the transmissivity of the dichroic.*

As illustrated in Figure 4-8, the transmissivity profile of the dichroic essentially reflects the 490 nm excitation light down to the sample, whilst allowing the majority of GFP emission photons to be transmitted back up to the camera for imaging. It is important to note, though the 490 nm excitation light was named as such, the spectra provided by the supplier (Mightex) was that shown by the blue curve in Figure 4-8. This curve looks more centred at 470 nm. Hence, future word could characterise the ground truth spectrum using a spectrometer.

Once replaced, I then sought to characterise the improvement and general capability of spatial light patterning of our system with respect to field uniformity and spatial precision.

4.4.3 REPLACING THE DICHROIC MIRROR IMPROVED THE HOMOGENEITY OF ILLUMINATION LIGHT IN THE SAMPLE PLANE

To assess the field uniformity of spatial light patterns, I cast a full-field light pattern down to the sample plane, as described in Section 4.3.2. The rational was to image these patterns and understand how light was distributed across the addressable area of the microscopes FoV. Figure 4-9 shows these results.

Under the same illumination strategies, the new dichroic showed three improvements: first, a higher efficiency of light delivery across the field of view (Figure 4-9 a, b, and e); second, greater homogeneity of light across the pattern (Figure 4-9 e); and thirdly, it cast light to more of the addressable area (Figure 3-6 a-d).

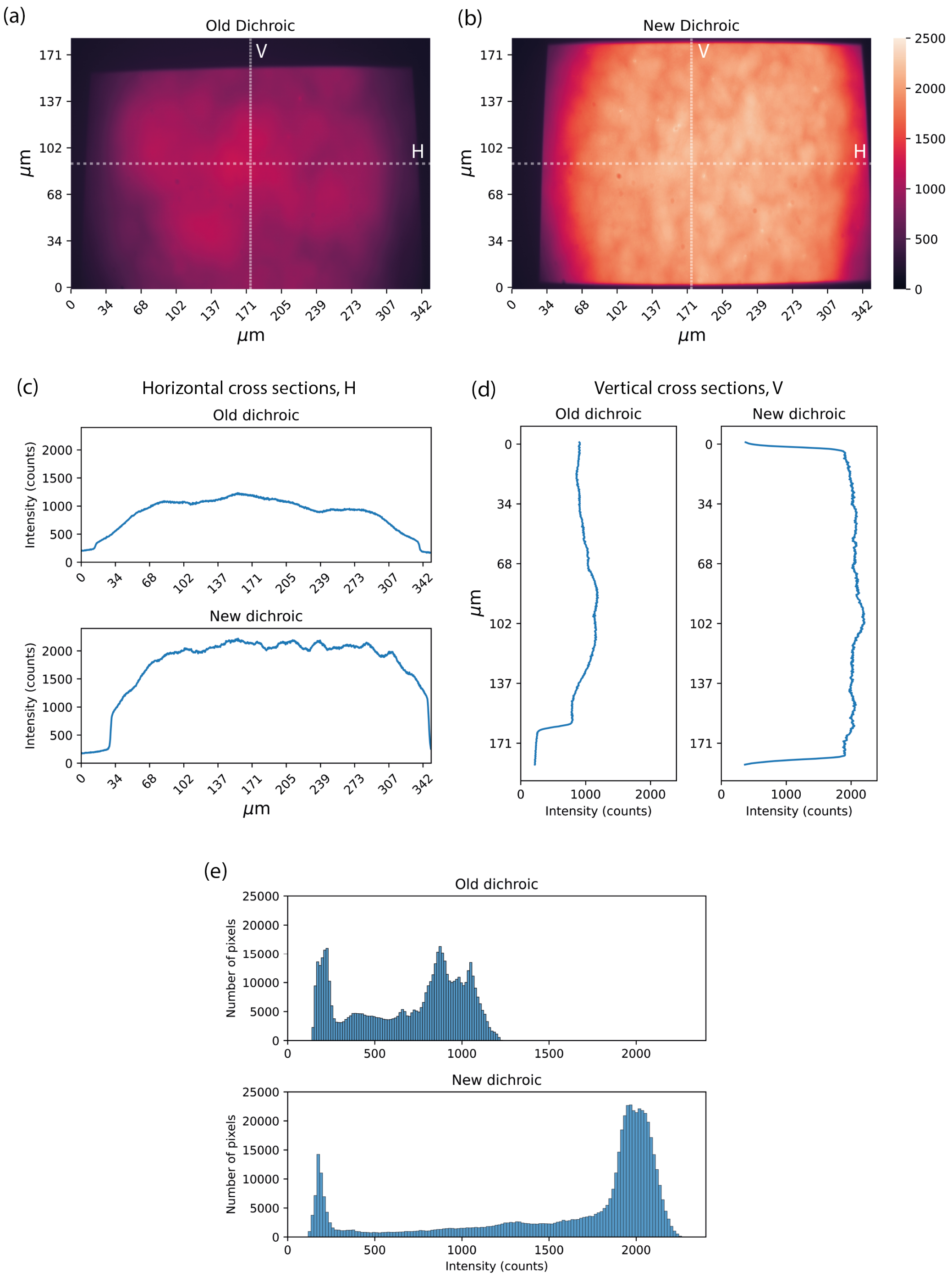

Figure 4-9 Replacing the dichroic mirror improved the homogeneity of illumination light in the sample plane*. Intensity plots of the old dichroic (**a**, proprietary, Mightex) and new dichroic (**b**, Chroma T525lpxr) reveal that under the same illumination conditions the new dichroic illuminated more of the Field of View, and with greater light intensity. The same LED power and alignment were used, and each plot was taken by averaging over 10 images taken by casting the illumination light on a spin-coated Rhodamine-6G slide. **c** and **d** show the corresponding horizontal and vertical intensity cross- sections of each image. **e** Quantitively, we observe the new dichroic registers higher intensity (counts) across the illumination area, with more camera pixels registering higher intensities, and a clearer bi-modal distribution relative to the old dichroic which shows a more heterogenous distribution of intensities across all pixels.*

4.4.4 SPOT SIZES OF PHYSIOLOGICAL RELEVANCE TO SINGLE-NEURON PHOTOSTIMULATION WERE RELIABLY GENERATED

To ensure photostimulation spots of physiological relevance (that is, sizes smaller than the cell soma diameter) could be reliably cast to the sample plane, I generated 5 µm and 10 µm spots and imaged them as described in section 4.3.2. The results are shown in figure 4-10. For this test, only the new dichroic was used as it was now clear that the old dichroic was not suitable for our needs.

Taking the vertical and horizontal cross section of average intensity plots for both spot sizes (4-10 c-d), I show that we can reliably cast spots of both sizes. The average full width, half-maximum (FWHM) for the 5 µm spot was 5 ± 0.2 µm in the horizonal and vertical cross-sections, and the average FWHM for the 10 µm spot was 10 ± 0.2 µm in the horizonal and vertical cross-sections.

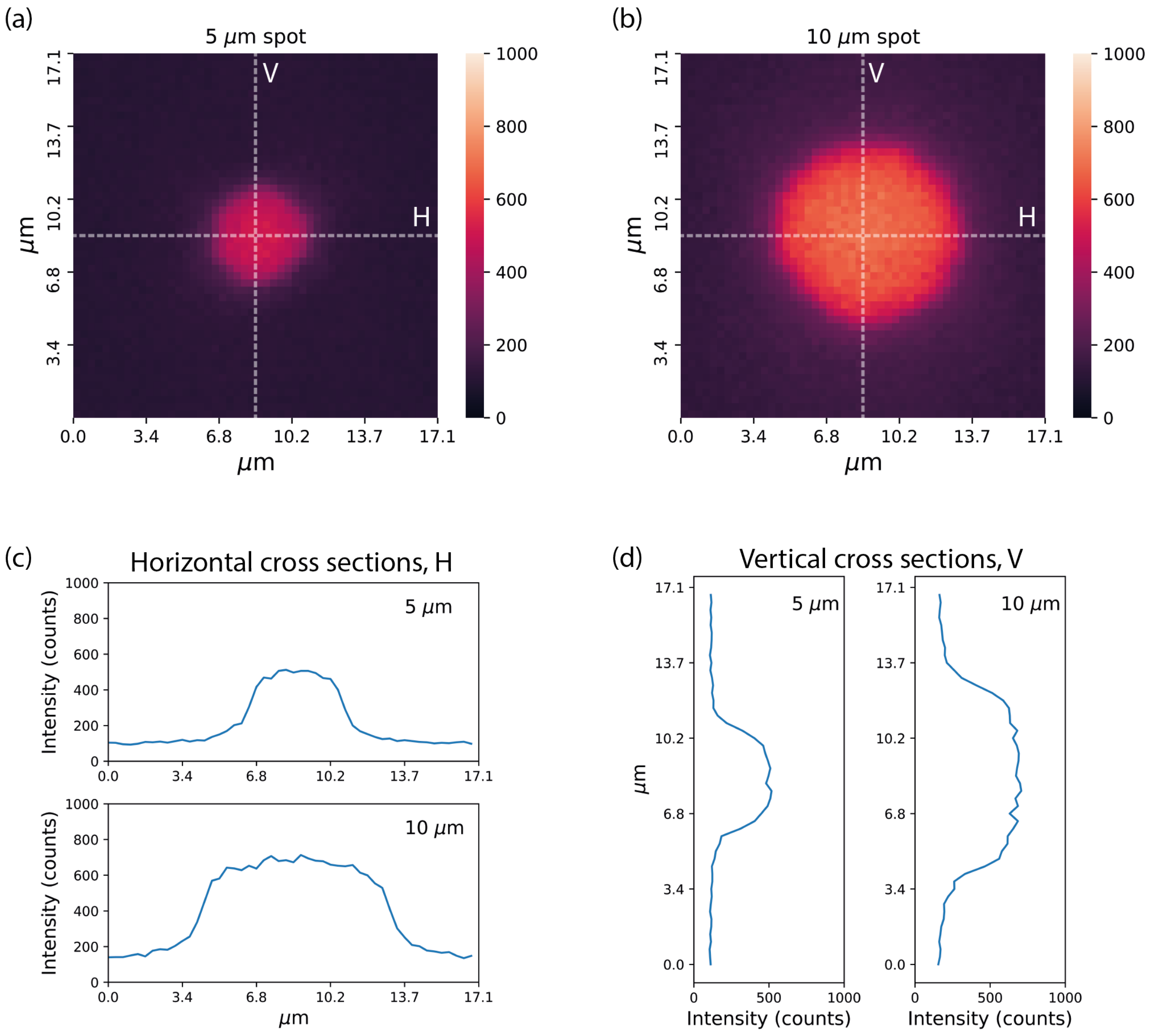

***Figure 4-10 Spot sizes of physiological relevance to single neuron photostimulation were reliably generated**. Average intensity plots of **a** 5 µm and **b** 10 µm light spots taken by casting the respective spots onto a spin coated rhodamine-6G slide. **c** and **d** show the corresponding horizontal and vertical intensity cross-sections of each spot. All data were taken by averaging over 5 images for each spot to account for any variability in rhodamine-6G coverage on the slide. The average full width, half-maximum (FWHM) for the 5 µm spot was 5 ±0.2 µm in the horizonal and vertical cross-sections, and the average FWHM for the 10 µm spot was 10 ±0.2 µm in the horizonal and vertical cross-sections. All spot images were taken from the centre of the microscope Field of View.*

To get another measure of light delivery efficiency and to calibrate the power output of the polygon system, I next sought to measure the light power at the sample plane.

4.4.5 REPLACING THE DICHROIC MIRROR IMPROVED THE EFFICIENCY OF LIGHT DELIVERY TO THE SAMPLE PLANE

By measuring the light power at the sample plane of the microscope (methodology described in section 4.3.7), I determined that under the same conditions the new dichroic outperformed the old dichroic with respect to the efficiency of light delivered to the sample plane. This was true for full-field illumination (4-11 a), as well as for light spot sizes of 5 µm and 10 µm (4-11 b, c). Furthermore, the light power at the sample plane showed a sub-linear response to polygon light power (4-11 a-c). Crucially, the system can generate 5 and 10 µm diameter spots with power densities encompassing the power densities seen in literature to make ChR2 expressing neurons spike.

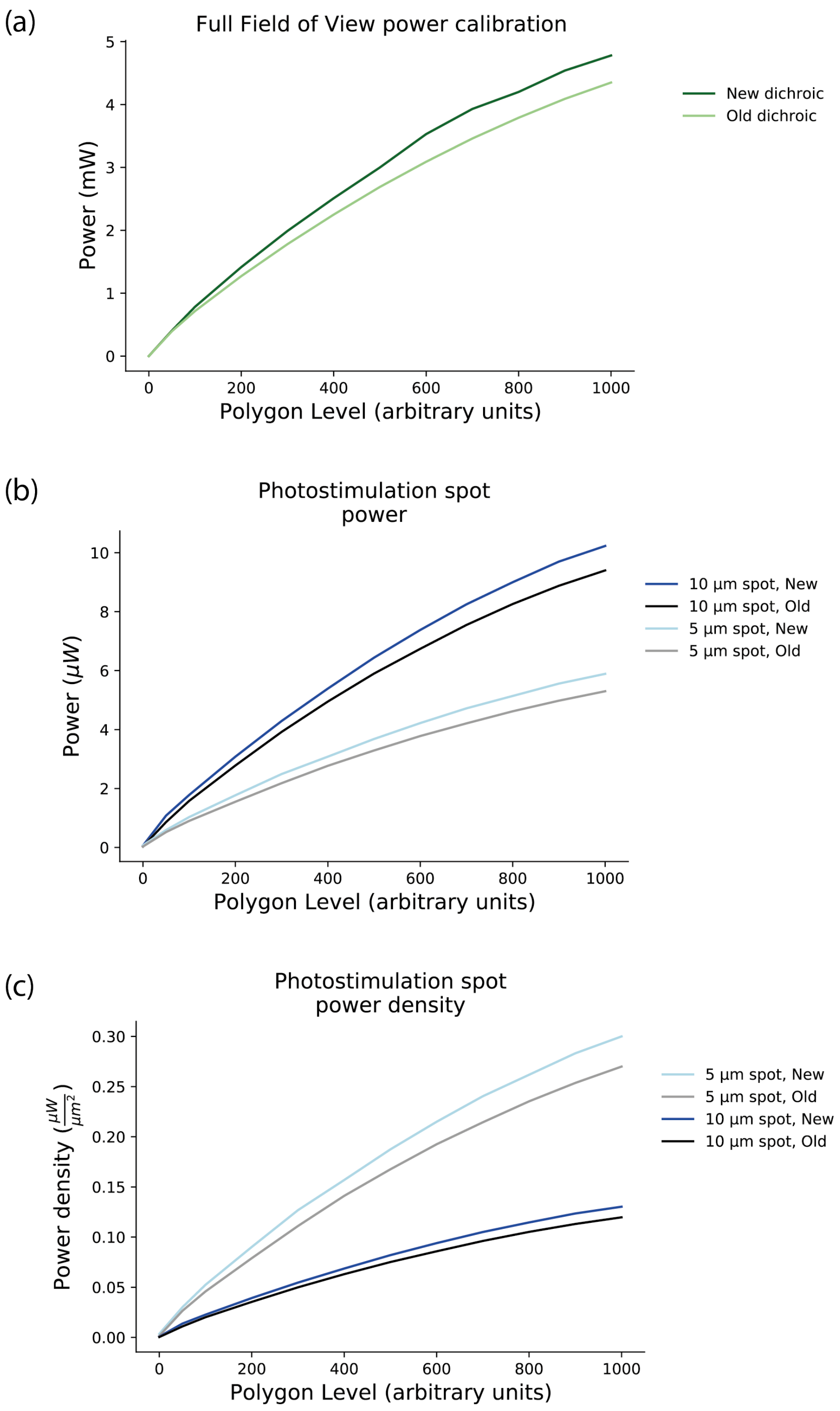

***Figure 4-11 Replacing the dichroic mirror improved the efficiency of light delivery to the sample plane**. We observe a non-linear response to polygon light power/power density and higher efficiency light delivery to the sample plane when: **a** illuminating the entire addressable field of view with increasing polygon power levels; **b** power and **c** power density calibrations casting a 5 μm and 10 μm spot to the sample plane with increasing Polygon power (0-1000 arbitrary units). Spots were cast to the centre of the addressable area where the power meter was placed, and data were taken when the reading stabilised for 2 seconds.*

After ascertaining that the new dichroic was suitable for our needs with respect to power efficiency and the spatial precision and distribution of light cast to the sample plane, it was time to understand the temporal characteristics of light patterning that the system was capable of.

4.4.6 LIGHT PATTERNS CAN BE TRIGGERED WITH MILLISECOND TEMPORAL DURATIONS

The first step to characterising the temporal light patterning capabilities of the system was to ensure we could shape light pulses with millisecond precision. To answer this question, I wired together a photodiode circuit to measure the temporal profile of light patterns (full methodology described in section 4.3.6).

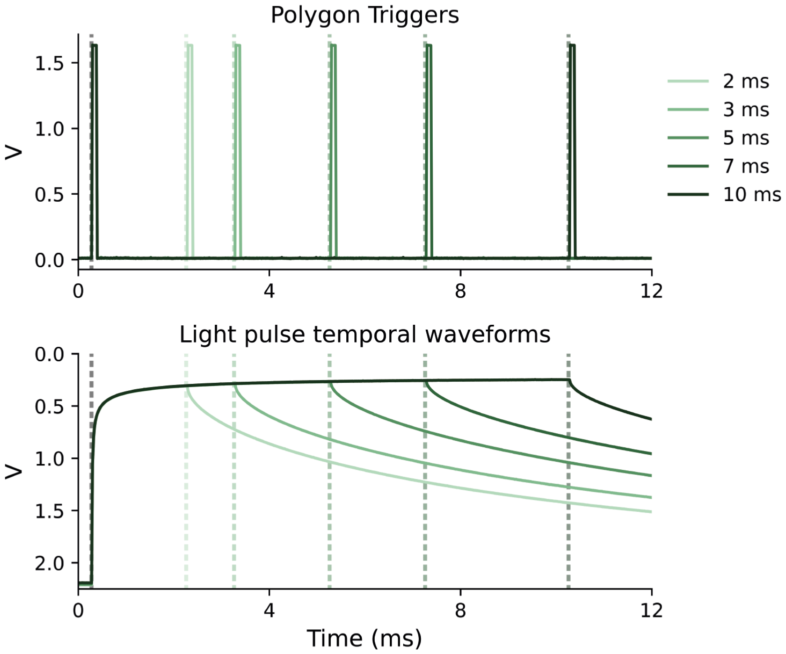

***Figure 4-12 Light patterns can be triggered with millisecond temporal durations**. Spatial light patterns were triggered by sending 'on' and 'off' signals to the DMD in the form of Transistor-Transistor Logic (TTL) pulses. The 'on' pulse at 0 ms (black line) was followed by 'off' signals at 2, 3, 5, 7, and 10 ms seconds (darkening shades of green). The top plot shows these pulses, and the bottom shows the temporal light profile measured at the sample plane using a photodiode circuit (described in section 4.3.6). Note the slow fall-off of voltage is explained by the exponentially decaying photodiode current rather than decay light intensity. The dashed lines show relevant TTL triggers.*

As seen in Figure 4-12, when generating light pulses with 2, 3 ,5, 7, and 10 ms durations the temporal profile of light measured at the sample plane was of the same duration as the corresponding pattern cast to the diode circuit. The dashed vertical lines in the bottom plot coincides with the time at which the photodiode starts discharging-in other words when the light is switched off.

4.4.7 LIGHT PATTERNS WERE ACCURATELY AND RELIABLY CAST WITH MEASURED DURATIONS IDENTICAL TO THE PROGRAMMED DURATION

Alongside temporal precision, accuracy and reliability of light pattern generation is of paramount importance. Accuracy in this case translates to the system casting a light pulse for the correct duration (i.e., what it was programmed to do), and reliability means that it can repeatably cast the programmed durations.

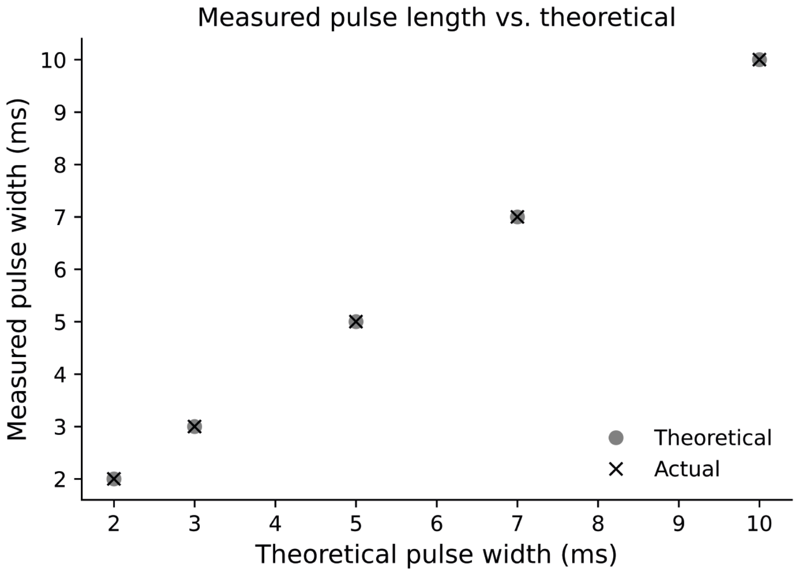

Figure 4-13 Light patterns were accurately cast with measured durations identical to the programmed duration. *By measuring the pulse width of light at the sample plane, we see that the theoretical (programmed) duration of light pulses matched the measured pulse duration.*

Figure 4-13 shows that the measured pulse length at the sample plane matched the theoretical programmed pulse width identically.

4.4.8 LIGHT PULSES WERE MEASURED WITH MICROSECOND LATENCIES AND ERRORS ACROSS ALL PULSE DURATIONS

To quantify the difference in measured vs. programmed pulse width, I took the average difference between the values across 5 trials and plotted the result. This error was reliably 20 µs across all pulse widths (Figure 4-14, top plot). Furthermore, the latency between light pulse trigger and measuring peak light power under the object in me was found to be 180 µs for all light pulses (Figure 4-14, bottom plot). Altogether, this demonstrates the system reliably cast light patterns to the sample with the desired, physiologically relevant, pulse durations.

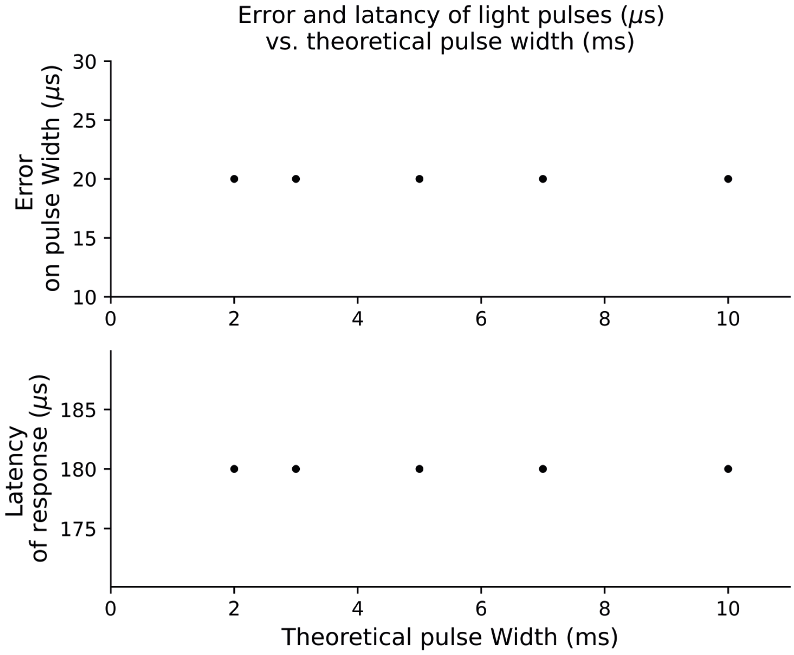

Figure 4-14 Light pulses were measured with microsecond latencies and errors across all pulse durations, indicating highly precise temporal control of light patterns*. Top plot: the error of the pulse width remained steady at 20 µs across all pulse widths. Bottom plot: the latency of response (measured as the time of peak voltage minus trigger time) remained steady at 180 µs. Note, these data were averaged over n=5 trials, and errors were plotted but too small to see on this scale.*

Note, the sampling rate as which the signal from the photodiode was digitised was 50 kHz which equates to a temporal resolution of 20 µs. In short this means that the rate at which

I sampled limited the measures of pulse width error and latency of response- giving an experimentally constrained precision (to all the above recordings) of ± 10 µs.

Once I had determined that the optical system was theoretically capable of single neuron precision photostimulation, millisecond temporal precision, and microsecond pulse width error, it was time to validate its use experimentally. The following section detail the validation phase of this chapter.

4.4.9 SOMA-TARGETED PHOTOSTIMULATION CHARACTERISATION: INCREASING PHOTOSTIMULATION SPOT SIZE AND LIGHT PULSE DURATION INCREASED PHOTOCURRENTS IN A CHR2 EXPRESSING NEURON

To validate the light patterning capabilities of our microscope for functional connectivity mapping with single cell spatial precision, I first sought to characterise the soma targeted photocurrents I could evoke with a 5 µm and 10 µm spot. To do this, I patched and photostimulated a ChR2-GFP expressing neuron as described in section 4.3.9. The raw photocurrent traces are shown below in Figure 4-15.

We see that increasing the pulse duration increases the peak evoked photocurrent (viewing the plots from top to bottom). We also see that the larger the spot size, the larger the photocurrent (viewing the plots from left to right). Average traces are shown in black, whilst individual traces are shown in grey. Photostimulation epochs are shaded in blue.

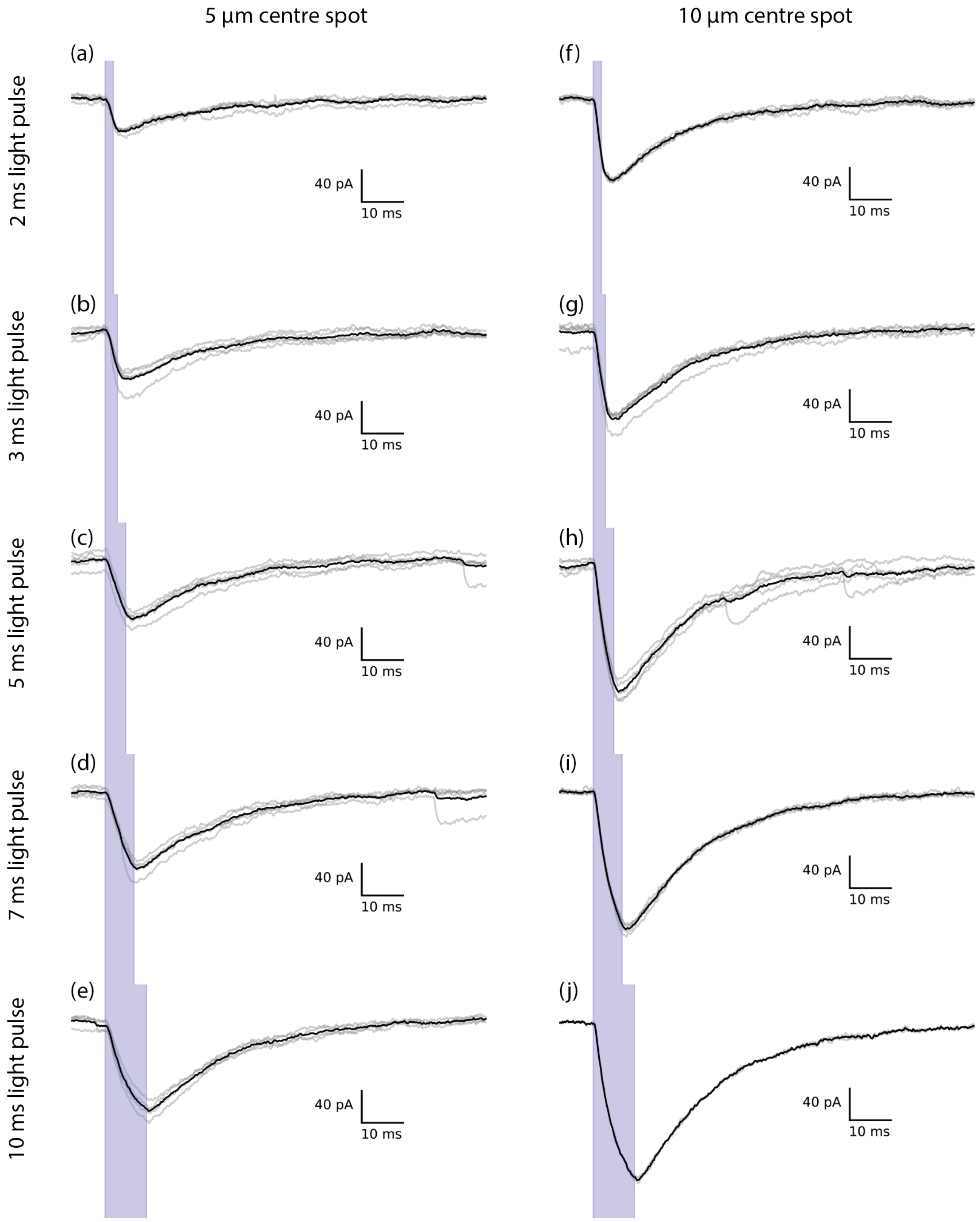

Figure 4-15 ***Increasing photostimulation spot size and light pulse duration increased photocurrents in a ChR2 expressing neuron****. Raw current- clamp traces of photocurrents of the same Inter- Telencephalic neuron shown in Figure 4-6 when photostimulating with a 5 µm diameter* ***a-e*** *and 10 µm diameter* ***f-j*** *490 nm photostimulation spot. Reading downwards in the figure shows how longer photostimulation times using the same spot diameter increases peak photocurrents, whilst reading left-right shows how using the same stimulation time but a larger diameter spot has the same effect. Grey traces represent individual trials (n = 5), and black traces represent trial averages. Blue bars represent photostimulation epochs. All scale bars are identical. The power density of the spots were 0.11* $^{\mu W}/_{\mu m^2}$ *or 0.125* $^{\mu W}/_{\mu m^2}$ *for the 10 µm or 5 µm spots, respectively.*

4.4.10 SOMA TARGETED PHOTOSTIMULATION CHARACTERISATION: AVERAGE PHOTOCURRENT OVERLAYS FOR 5 μM AND 10 μM PHOTOSTIMULATION SPOTS

The average traces from Figure 4-15 are shown below, this time with increasing pulse durations being shaded with darker shades of blue.

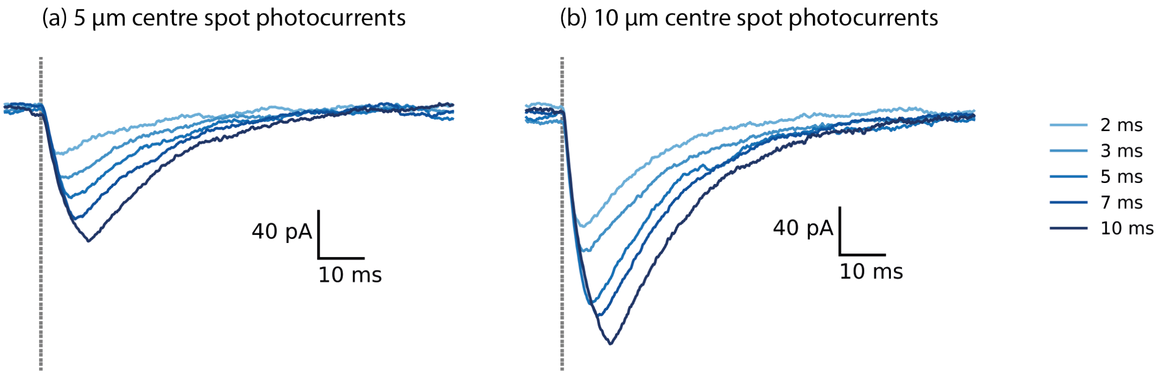

(a) 5 μm centre spot photocurrents

(b) 10 μm centre spot photocurrents

Figure 4-16 Average photocurrent overlays for 5 μm and 10 μm photostimulation spots. *Average current clamp photocurrent traces for the **a** 5 μm and **b** 10 μm photostimulation spot trials in Figure 4.15. Darkening shades of blue represent longer photostimulation durations (labelled in the legend), and the grey dashed lines represent the stimulation onset. All curves are averages of n=5 trials in the same neuron using power densities of* $0.11\ {}^{\mu W}/_{\mu m^2}$ *or* $0.125\ {}^{\mu W}/_{\mu m^2}$ *for the 10 μm or 5 μm spots, respectively.*

Each blue trace shows the average raw traces over n= 5 trials, and we see clearly that increasing spot size and pulse duration increases the photocurrent.

4.4.11 SOMA TARGET PHOTOSTIMULATION CHARACTERISATION: QUANTIFIED AVERAGE PEAK PHOTOCURRENTS FOR 5 μM AND 10 μM PHOTOSTIMULATION SPOTS

The quantified peak photocurrent for the data in Figures 4-15 and 4-16 are shown in Figure 4-17. When increasing the light pulse duration from 2 ms to 10 ms, the peak photocurrent rises from 100 ± 0.3 pA to 200 ± 2 pA for the 10 µm spot and from 41 ± 2 pA to 114 ± 8 pA for the 5 µm spot.

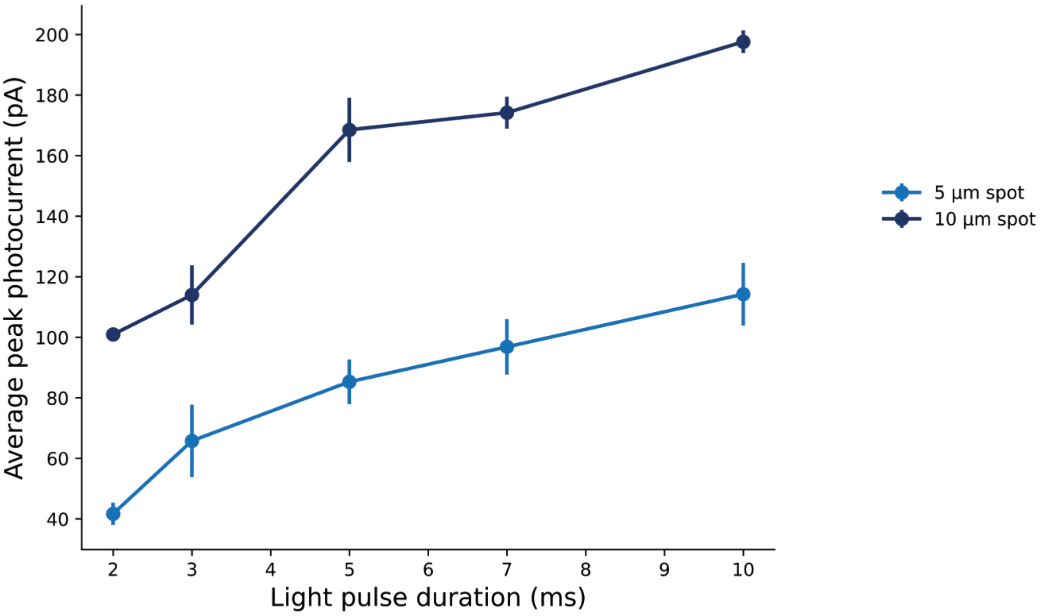

Figure 4-17 Quantified average peak photocurrents for 5 µm and 10 µm photostimulation spots. *Average current clamp photocurrent traces for the 5 µm (dark blue) and 10 µm photostimulation spot trials in Figures 4-15 and 4-16. Each data point is a trail average across n = 5 trials, and vertical lines represent the Standard Error on the Mean (SEM) values. Power densities of 0.11* $^{\mu W}/_{\mu m^2}$ *or 0.125* $^{\mu W}/_{\mu m^2}$ *for the 10 µm or 5 µm spots, respectively were used for this dataset.*

4.4.12 LATERALLY DISPLACING THE PHOTOSTIMULATION SPOT REDUCED PHOTOCURRENT MAGNITUDE AND DEMONSTRATED THE SPATIAL CONFINEMENT OF PHOTOSTIMULATION SPOT

To get an experimental verification of lateral spatial precision of photostimulation spots, I then photostimulated spots with lateral displacement from the neuron. Shown below. Note, the locations (numbers 1-9) refer to the optogenetic stimulation grid described in Figure 4-5, and shown inset in Figure 4-18 b.

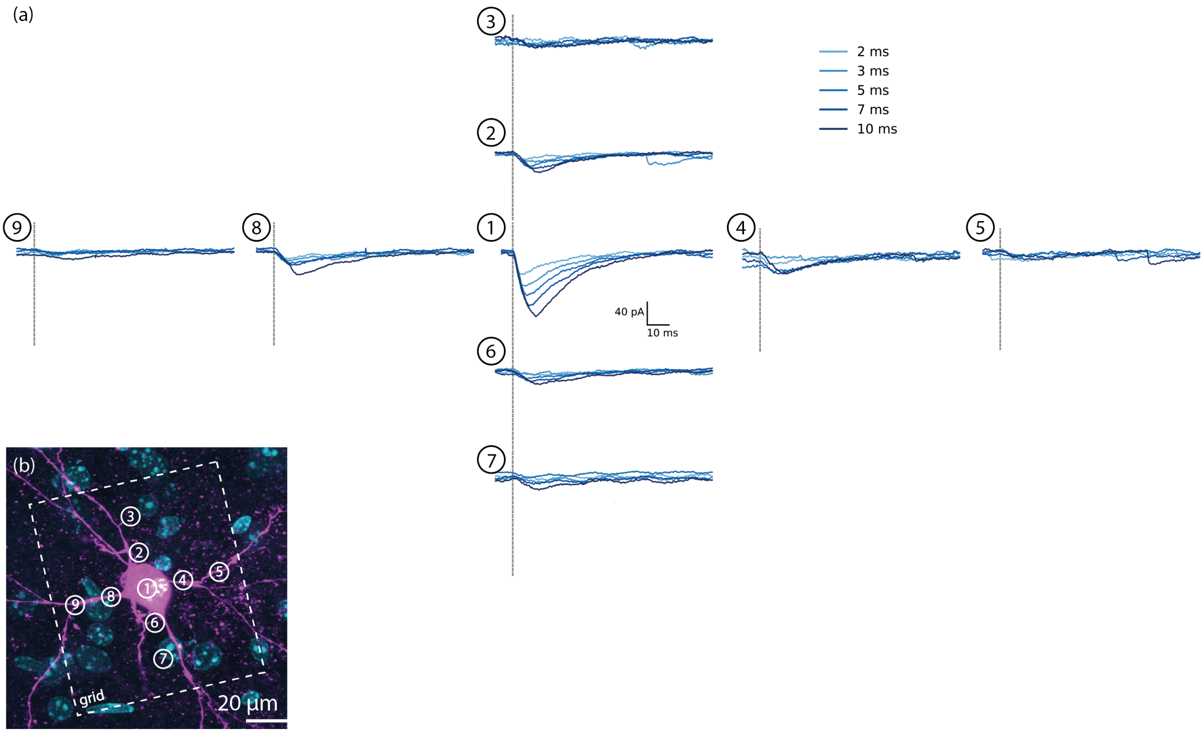

Figure 4-18 Laterally displacing the photostimulation spot reduced photocurrent magnitude and demonstrated the spatial confinement of photostimulation spots*. Referring to the photostimulation spot map in* ***b*** *(location numbers 1-9), the average photocurrent traces for a 5 µm photostimulation spot are shown in* ***a*** *with corresponding location numbers 1-9. Increasing light pulse durations are shown with darkening shades of blue, with pulse durations ranging from 2 -10 ms. Each trace is averaged over n = 5 trials, and vertical lines represent the photostimulation onset. As seen, the longer the light pulse duration, the larger the photocurrent, and the further away the photostimulation spot, the smaller the photocurrent. Note, the photocurrents do not disappear completely when laterally displaced- with reference to the map in a it is likely that the light spot is photostimulating opsin in the neuronal processes.*

We see that displacing the spot relative to the neuron decreased the photocurrent, almost eliminating it altogether. This confirms that our photostimulation patters are spatially confined in the lateral extent. However, we see that laterally displaced photocurrents exist, and with reference to the putative photostimulation map in Figure 4-18 **b**, it would seem that I was photostimulating opsin expressing processes.

4.4.13 AXIALLY DISPLACING THE PHOTOSTIMULATION SPOT SHOWS MINIMAL IMPACT ON PEAK PHOTOCURRENT OR PHOTOCURRENT RISE-TIME

With respect to the axial confinement of our spots, we see that axially displacing our spot whilst photostimulating the neuron soma (methodology described in section 4.3.9) had minimal effect on photocurrent peak magnitude or the 10-90 rise time, as shown in figure 4-19. Qualitatively, both parameters remain relatively flat across all axial depths of focus and pulse durations tested for this neuron. Due to the variability of the data, this observation was difficult to properly quantify. Further measurements or increasing the number of neurons recorded from may help to derive a precise quantitative measure.

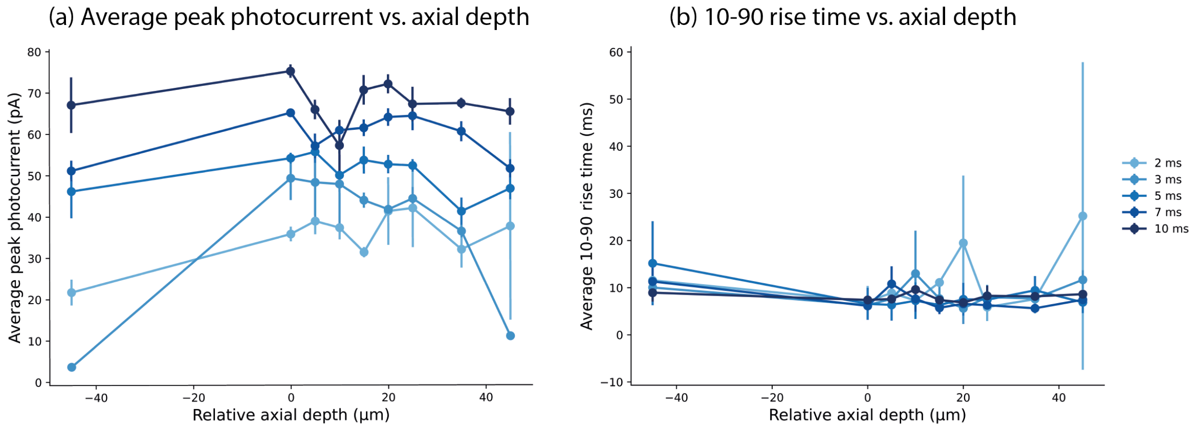
(a) Average peak photocurrent vs. axial depth

(b) 10-90 rise time vs. axial depth

Figure 4-19 Axially displacing the photostimulation spot shows minimal impact on peak photocurrent or photocurrent rise-time. *Axially displacing our spot whilst photostimulating the neuron soma (methodology described in section 4.3.9) had minimal effect on photocurrent peak magnitude* ***a*** *or the 10-90 rise time* ***b****. Both parameters remain relatively flat across all axial depths of focus and pulse durations tested for this neuron. Each circle represents the trial average (n=5 trials, and the vertical lines represent the Standard Error on the Mean (SEM). The darker the shade of blue, the longer the pulse duration as noted in the figure legend on the right-hand side. For all trials, a 5 μm light spot was used with a power density of 0.125* $\mu W/_{\mu m^2}$.

4.4.14 THE EFFECTS OF PHOTOSTIMULATION LIGHT POWER ON PEAK PHOTOCURRENT AND RISE TIME

The final validation step was characterising the effect of light power on photocurrents. Figure 4-20 show these results.

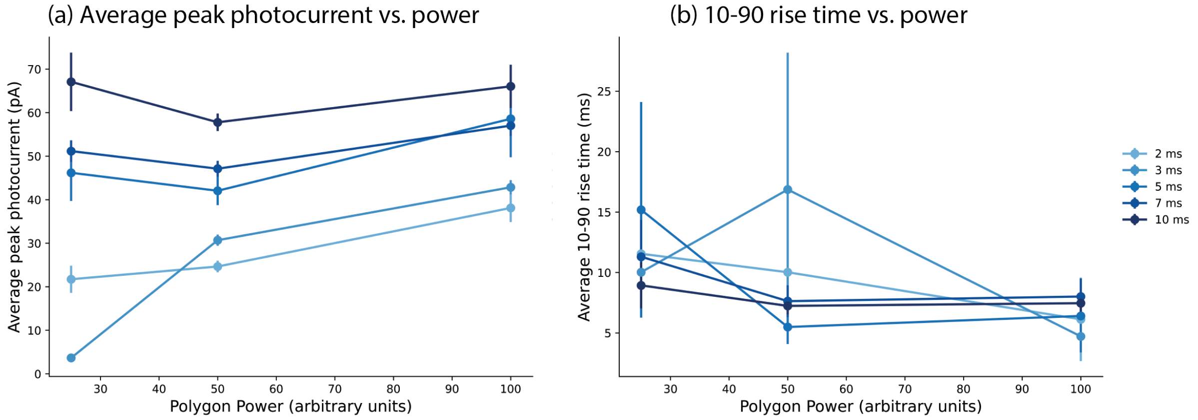

Figure 4-20 The effects of photostimulation light power on peak photocurrent and rise time*. Varying the light power from 0-1000 units (in this case, 0 $^{\mu W}/_{\mu m^2}$ - 0.125 $^{\mu W}/_{\mu m^2}$, for full methodology see section 4.3.9) showed a flat response in average peak photocurrent* ***a*** *and 10-90 rise times* ***b****. Increasing pulse durations are shown in darker shaders of blue. The larger the pulse duration, the larger the average peak photocurrent. However, increasing the pulse duration seemed to have no effect on the 10-90 rise time in the neuron recorded. Each circle represents the trial average (n=5 trials, and the vertical lines represent the Standard Error on the Mean (SEM). The darker the shade of blue, the longer the pulse duration as noted in the figure legend on the right-hand side.*

Varying the light power from 0-1000 units (in this case, 0 $^{\mu W}/_{\mu m^2}$ - 0.125 $^{\mu W}/_{\mu m^2}$, for full methodology see section 4.3.9) showed a flat response in average peak photocurrent and 10-90 rise times. Increasing pulse durations are shown in darker shaders of blue. The larger the pulse duration, the larger the average peak photocurrent. However, increasing the pulse duration seemed to have no effect on the 10-90 rise time in the neuron recorded.

4.4.15 COMPARING PHOTOCURRENT CHARGE TRANSFER TO AMPA CONDUCTANCE CHARGE TRANSFER

Revisiting the charge transfer per AMPA conductance and membrane potential in Figure 3-10, we can begin to make an assessment on spiking probability given particular photostimulation paradigms. Figure 4-21 below shows the comparison between the charge transfer measured for the AMPA conductances shown in Figure 3-10, and the charge transfer across the set of photostimulation protocols (5 µm and 10 µm spot sizes at light pulse durations of 2 ms – 10 ms. The total charge transfer for photocurrent events was calculated in a similar way to that of the AMPA conductance; it was essentially the area under the average photocurrent trace.

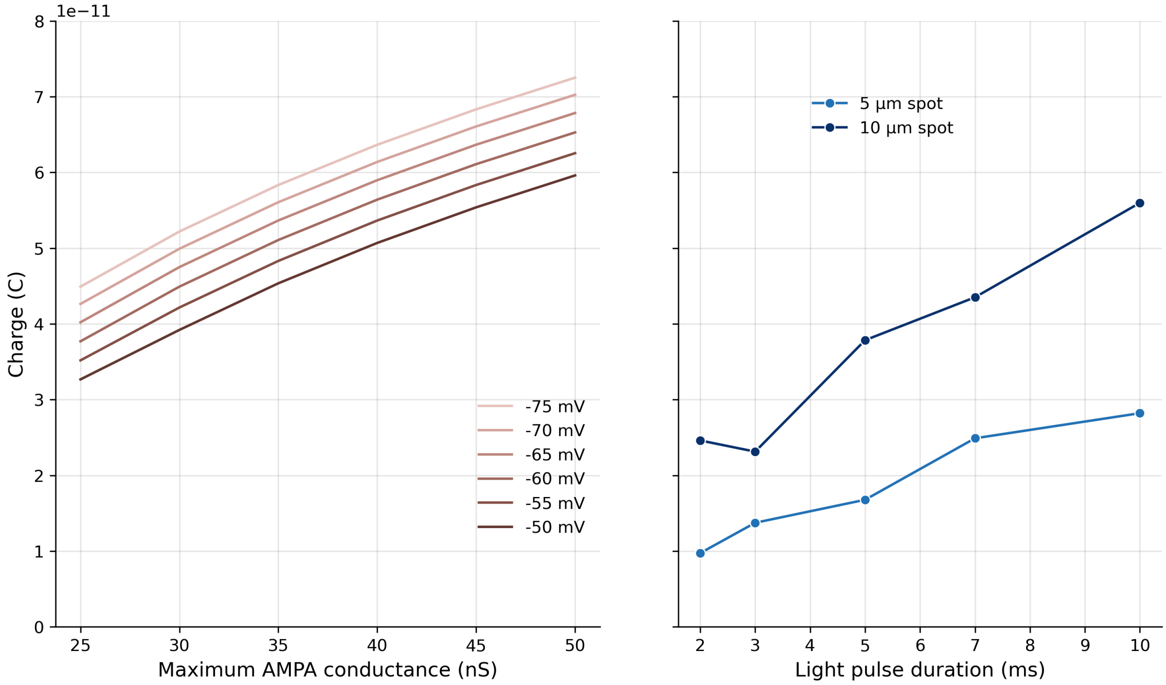

Figure 4-21 Comparison of total charge transfer between AMPA conductances and photocurrent events*. Replotting the charge transfer per AMPA conductance and membrane potential in Figure 3-10 (left plot) next to the charge transfer during a photocurrent event (right hand plot), using a 10 µm spot diameter with a 5 ms pulse duration and above begins to match the charge transfer over the course of the set of AMPA events tested in Section 3.4.8. Note, power densities of 0.11* $^{\mu W}/_{\mu m^2}$ *or 0.125* $^{\mu W}/_{\mu m^2}$ *for the 10 µm or 5 µm spots, respectively were used for this dataset.*

The data shown in Figure 4-21 shows that photostimulation spots 10 μm in diameter at light pulse durations greater that 5 ms have comparative charge transfer to AMPA conductances which were shown to evoke APs in neurons (for the corresponding data, please see section 3.4.

4.5 DISCUSSION

4.5.1 REFLECTION ON CHAPTER AIMS

The functionality of our system was successfully improved in relation to our experimental needs

The first goal of this chapter was to develop the light patterning microscope such that I could optimise it's use for local functional connecting mapping of neuronal microcircuits with single cell spatial precision. To this end I installed a new, ultra-flat dichroic mirror optimised for the optical spectra relevant to our animal models and experimental plan Figure 4-8). By assessing the homogeneity of light when casting full field of view illumination down to the sample plane of our microscope, I demonstrated a marked improvement to our systems light patterning capabilities (Figures 4-9 and 4-10). With reference to the histograms of pixel intensity (Figure 4-9 **b**), we see clearly that the distribution if pixel intensities for the old dichroic mirror was far more heterogenous than the new dichroic, with the population of intensities more left leaning than the new. This suggests a heterogenous illumination of the sample plane, and a less efficient delivery of light to the sample when contrasting to the new dichroic; the new dichroic has a cleaner bimodal distribution of pixel intensities corresponding with illuminated and non-illuminated areas of the sample plane. It also has far more pixels illuminated at greater intensities- once again suggesting a higher efficient of light delivery. This disparity of light efficiency is seen clearly in power calibrations (Figure 4-11), ad driven home by the fact that all of the above described data used identical illumination strategies. Ultimately, this improvement in performance can be explained by the old dichroic being tarnished and likely not optimised for the task at hand- though for the latter point no further comment can be made without precise knowledge of the specifications of the optic.

To conclude this specific aim with respect to experimental constraints, the new dichroic allows us to distribute light more evenly to different neurons across the addressable area of the microscope's Field of View. We would also need less light power than with the old dichroic to achieve the same spot power densities. In other words: we can rapidly photostimulate more neurons with comparatively lower experimental complexity and a higher degree of experimental robustness and consistency.

The microscope is able to reliably generate spatially precise photo stimulation spots with sizes of physiological relevance to single neuron level many to one functional connectivity mapping experiments

The second aim of this chapter was to characterise the light patterning capabilities of our optical system in both the temporal and spatial domains. Specifically, I wanted to ascertain that we could reliably generate photostimulation spots within the size of a single IT neuron cell body (~10 μm), at power densities and pulse durations necessary to induce action potentials.

In the spatial domain, I firstly demonstrate that we can generate arbitrary lateral spatial patterns of light in the sample plane, before showing that we can reliably cast laterally confined spots down to the sample plane. The latter was achieved by imaging 5 μm and 10 μm spots with a fluorescent Rhodamine-6G spin-coated slide (Figure 4-10). Both spots had an uncertainty in diameter (as measured by the Full Width, Half Maximum of the spot image intensity cross-sections) of 0.2 μm. This shows we can reliably generate physiologically relevant spots size in the later extent of our sample.

We were able to reliably generate light patterns with millisecond temporal precision

In the temporal domain, I used a custom photodiode circuit to measure the temporal profile of light patterns at the sample plane. I show that we can precisely generate patterns with millisecond precision, and furthermore reliably with microsecond errors (Figure 4-14). With the former, pulse widths were repeatedly generated with errors in duration 20 μs ± 10 μs suggesting we can generate pulse widths of any length with a high degree of reliability. This value equates to a 1 % error on a 2 ms pulse width and could in principle be smaller than measured. The measurement was limited by the sampling rate of the Power1401 digitisation. Sampling above 50 kHz could provide a more accurate measure. With respect to pulse latency, it was seen that across all pulse widths there was a consistent 180 μs latency between pattern triggering and peak photodiode current measurement. This suggests that we have a small systematic error in our pulse timing measurements, but a reliable one meaning we can easily subtract this error or generally take it into account depending on the experimental paradigm we chose.

I validated the microscopes capability by demonstrating precise temporal and spatial control of photocurrents

The final aim of this chapter was to validate the system's use for single neuron precision functional mapping in our animal model. By whole-cell, voltage clamping an Inter-Telencephalic (IT) neuron in the PFC and running an array of photostimulation characterisation protocols (described in section 4.3.9), I validate that we can photostimulate single IT neurons in the PFC, and by extension, that our microscope is capable of single neuron precision functional connectivity mapping.

By photostimulating the soma of said neuron with 5 μm and 10 μm spots I show that the latter evokes larger photocurrents than the former. Similarly, increasing the pulse duration increases the peak evoked photocurrent (Figures 4-15, 4-16, and 4-17). To take this a step further and demonstrate the lateral spatial confinement of light patterns, I laterally displaced the spots from the target neuron and observed a marked decrease or disappearing of any photocurrents (Figure 4-18). Indeed, with reference to the registered photostimulation grid in Figure 4-18 **b**, it seems likely that photocurrents observed while illuminating laterally displaced areas relative to the neuron some arise from stimulation of opsin expressing processes of the same neuron. Though the registration process itself has some subjectively involved and it's accuracy cannot be completely relied upon (I manually selected morphologies which I myself perceived to be similar) this points towards a significant limitation of our system- ChR2-GFP is expressed in the entire transfected neuron, hence it is within the realm of possibility that we could be adding a confounding variable to optical connectivity mapping paradigms in the form of unintended photostimulation of neuronal processes. Though this was something we considered from the get-go when planning these experiments, these data provide a nice illustration and validation for this limiting aspect of our mapping paradigms.

Power densities and charge transfers were in theory sufficient for evoking Action Potentials

Considering Figure 4-11, we see that we can generate 5 and 10 μm diameter spots with power densities encompassing the power densities seen in literature to make ChR2 expressing neurons spike[49]. Furthermore, referring to Figure 4-21, we see that using a 10 μm spot diameter with a 5 ms pulse duration and above, and a power density of 0.11 $^{\mu W}/_{\mu m^2}$, we begin to match the charge transfer over the course of the set of AMPA events tested in Section 3.4.8 at a range of biophysically realistic membrane potentials. The key part of this is that the entire range of AMPA conductance were able to evoke action potentials in patched neurons. Hence, we can make an inference on our photostimulation protocols: using the above stated parameters which match the AMPA charge transfers, it is possible that we are evoking APs in putative presynaptic neurons.

However, it is worth discussing the datasets used. With respect to the AMPA dataset, we have no precise knowledge of the neuronal classes used. So, whilst I observed APs using the AMPA conductance protocols, it could be that these were from a cell class with a different excitability than IT neurons, hence not necessarily a comparable dataset. On balance, upon visual inspection of cell morphology during patching, and looking at the set of AP properties, it is likely that these were pyramidal neurons, and furthermore given their anatomical location in the slice (I specifically aimed for Layer 5 pyramidal neurons in the PFC using the Allen Brain Atlas as guide), it is possible that they are of similar physiologies to the IT neurons I photostimulated. With respect to the photocurrent charge dataset: the dataset came from a single neuron. This paucity of data is unfortunately due to poor cell health and expression profiles of ChR2 expressing neurons- as discussed at multiple points of this thesis- but in essence increasing the number of neurons which this graph is derived from can help us more reliably and quantifiably make inferences on presynaptic spiking, but furthermore gain a trial average which works towards ironing out expression heterogeneity; we could calculate an average charge transfer per photostimulation parameter set *over a range of expression levels* which could help us to tweak photostimulation parameters to maximise presynaptic spiking probability in repose to photostimulation. This is especially critical without any reporting of presynaptic activity.

4.5.2 SYSTEM LIMITATIONS AND FUTURE EXPERIMENTAL CONSIDERATIONS

As we began to see during the characterisation step, there were certain limitations to the capabilities of our system. Here, I will outline these limitations and suggest possible directions one could take to mitigate their effects.

No axial confinement of photostimulation spots

A clear limitation of our system was the axial confinement of photostimulation spots. We knew *a priori* that this would be the case; we were using LED light and in the single photon illumination domain, hence axial confinement would be low. As seen in Figure 4-19, this is clearly the case: axially displacing the photostimulation spot whilst using the same photostimulation paradigms has no effect on peak photocurrent or the 10-90 rise times of said photocurrents. Hence, in the view of functional connectivity mapping using our system, we must take care not to select any putative pre- or post- synaptic neurons which may have other ChR2-GFP expressing neurons in the same axial column. Moreover, given the expression of ChR2-GFP in neuronal processes which could be spanning several or all possible axial columns in our sample, this is an important factor to consider going forward. One possible way of getting around this problem of poor axial confinement would be moving from a 1 photon to 2 photon illumination regimes (with an overview of the myriad elaborate systems being developed described in Section 1.4.6). However, this is not readily doable without the necessary laser systems.

Opsin expression variability and ubiquity

Opsin expression proved to be a stubborn hinderance to this project at large. In my view, this can be broken down in to three domains: 1) variability of expression, 2) the effects of expression itself, and 3) ubiquity of expression.

First, it was observed that expression variability was extremely high, even given our attempts at having uniform expression strategies across all animals. This included using the same virus titre, injection location, mouse age, and experiment time following injections. Outside of intrinsic biological variability, the variability in expression could be explained by varying injection flow rates (this proved difficult to maintain on our system) or unknown blockages of the injection pipette.

For reference, we injected 10 mice, 8 of which were female, and two male. The coordinates remained the same, save for one animal which we inverted the medial lateral coordinate to avoid a blood vessel on the original side. The virus titre, batch and surgical procedure remained uniform across the cohort. We furthermore sacrificed all animals 14-21 days post injection.

The consequence of the variability was that we observe 4 of the 10 animals having noticeable expression levels, of which 2 we were able to collect data from due to cell health issues- which segues nicely into the effects of expression.

More often than not the intersection between healthy neurons and expressing neurons was woefully low. Though only an observation without any scientific process to confirm, it seemed as though opsin expression was bad for neuron health[98]. We routinely observed GFP signal (and hence opsin expression) in dead cells. However, we also observed minimal fluorescence in opsin positive cells (indeed, the two neurons described in sections 4.4.9-20 displayed minimal GFP expression, and yet were opsin positive). This suggests that perhaps too much expression is bad for cell health, and as a consequence we could reduce virus titre for future work.

Finally, with respect to the ubiquity of expression, we observed GFP signal essentially throughout our sample, making the discernment of ChR2-GFP neurons difficult. This was likely due to expression in neuronal processes, and hence a future direction could consider utilising soma targeted variants of ChR2-GFP. These variants, while not perfect, limit expression to the soma of transfected neurons only. This would mean that for functional connectivity mapping experiments one could eliminate the possibility of photostimulating opsin expressing processes. However, this is not a free lunch; by going down this path one loses the ability to structurally map opsin expressing neurons in our model, precluding any possibility of mapping functional to structural connectivity.

Larger datasets

Finally, as a direct consequence of cell health, opsin expression, various author illnesses, hospital trips, and global pandemics, our n-numbers were rather low. A clear future direction of this work would be to optimise the ChR2 expression strategy where possible and repeat all experiments to gain some statistical power to our results.

CHAPTER 5

OPTICALLY MAPPING THE LOCAL FUNCTIONAL CONNECTIVITY OF INTER-TELENCEPHALIC NEURONS IN THE PREFRONTAL CORTEX

5.1 ABSTRACT

After developing, characterising, and validating the light patterning microscope for single-neuron resolution photostimulation with millisecond temporal precision, I sought to map the local functional connectivity of Inter-Telencephalic (IT) neurons in the Prefrontal Cortex (PFC). During the aging process, cross-sectional Positronic Emission Tomography (PET) studies of the brain have shown increased bilateral metabolic activity in the PFC, but only in individuals scoring higher on cognitive performance assays[25,26]. A proposed explanation of this phenomena is network remodelling: the brain recruits broader networks of neurons to maintain cognitive performance over time. However, at the level of neuronal microcircuits the underlying neural network structure and function through time is not well understood. This presents an opportunity for our microscope: understanding the local functional connectivity of such neurons could shed light on our understanding of aging in the brain.

With this in mind, we unilaterally injected a retrovirus containing ChR2-GFP into the PFC of wild-type mice. This led to expression of opsin in the contralateral PFC hemisphere-specifically in neurons projecting to the injection site. Using full Field of View (FoV) photostimulation whilst voltage-clamping a non-expressing neuron, I show that IT neurons are functionally connected to non- IT neurons in the same local region. Furthermore, I observe polysynaptic activity after full FoV stimulation, indicative of more complicated functional architectures. To confirm functional connectivity within this sample, I utilised tetrodotoxin, 4- Aminopyridine, and Kynurenic acid to block action potentials and synaptic transmission, which, upon addition, eliminated any light-stimulus related responses in the patched neuron.

I then attempt single neuron precision functional mapping in another sample with confirmed local functional connectivity, finding no evidence of single neuron functional connectivity. Unfortunately, due to cell health, expression profiles, and timing constraints on this project I was unable to gather further data. Nonetheless I conclude that our system is capable of addressing our scientific goals within specific limits and outline future work and directions of this project.

5.2 INTRODUCTION

Here I discuss the scientific context of this chapter, specifically how functional connectivity in the brain may be affected by the aging process. I then move on to the topic of optical functional connectivity mapping, and the specific goals of this chapter. For a broader discussion of connectivity and connectivity mapping, please see Chapter 1, Sections 1.3 and 1.5. Similarly, for a broader discussion of optogenetics and the related optical microscopy tools, please see Chapter 1, Section 1.5.

5.2.1 SCIENTIFIC CONTEXT

During the natural aging process, the brain is thought to employ compensatory processes to mitigate the effects of cognitive decline[25,26,118]. One such process is network remodelling, where broader neural networks are recruited to maintain cognitive performance over time[26]. This network remodelling is potentially seen in the Prefrontal Cortex (PFC). The PFC is highly interconnected to other cortical and subcortical regions and is implicated in a range of cognitive functions including working memory, long term memory, decision making, and attention. These functions are known to be affected by aging, therefore understanding how PFC circuitry changes over time could help us to better understand the aging process.

Cognitive assays on humans testing episodic memory retrieval have shown that those who maintain performance as they age have increased bilateral metabolic activity in the PFC (as revealed by Positron Emission Tomography (PET)). Conversely, younger subjects and those who demonstrate a decline in performance over time were observed to maintain unilateral activity patterns in the PFC[25]. However, the underlying functional connectivity at a single neuron level precision is not well known.

Network remodelling which could explain this change in metabolic activity could be occurring in Inter-Telencephalic (IT) neurons which project between PFC hemispheres[33]. As discussed in Section 1.3, neurons with similar functional purposes are more likely to be functionally connected[32,37,40] to one another than neurons with differing functional purposes. Furthermore, when considering the theory of network remodelling it could be that these IT neurons whose functions include cross-hemisphere connectivity could form the basis of a network scaffold upon which functional architectures could be built when redistributing computation. Herein lies the scientific context to the connectivity mapping experiments of this chapter: to validate the use of the light patterning microscope developed and characterised in Chapter 4 for local functional connectivity mapping of IT neurons in the PFC.

5.2.2 ANIMAL MODEL DESCRIPTION AND JUSTIFICATION

Please note, this section can also be considered as the justification for the animal model used in Chapter 4 Sections 4.4.9-15.

To study the local functional connectivity of IT neurons in the PFC, we unilaterally injected a retrovirus in to the PFC of C57BL/6 wild type mice. The full methodology can be found in Section 2.2.2. The rationale behind this was as follows: IT neurons in the PFC which project across hemisphere to the injection site would express ChR2-GFP (for a diagram of this, please see Figure 5-3), hence allowing local functional connectivity mapping experiments amongst these functionally defined (and functionally similar) neurons.

Figure 5-1 below shows a 2-photon serial tomography image of an example of our animal model (please note, credit for this image goes to Dr Gerald Moore). Of note, we see that in the contralateral hemisphere (left hemisphere in the image) relative to injection site (right hemisphere) has a relatively sparse expression profile of ChR2-GFP.

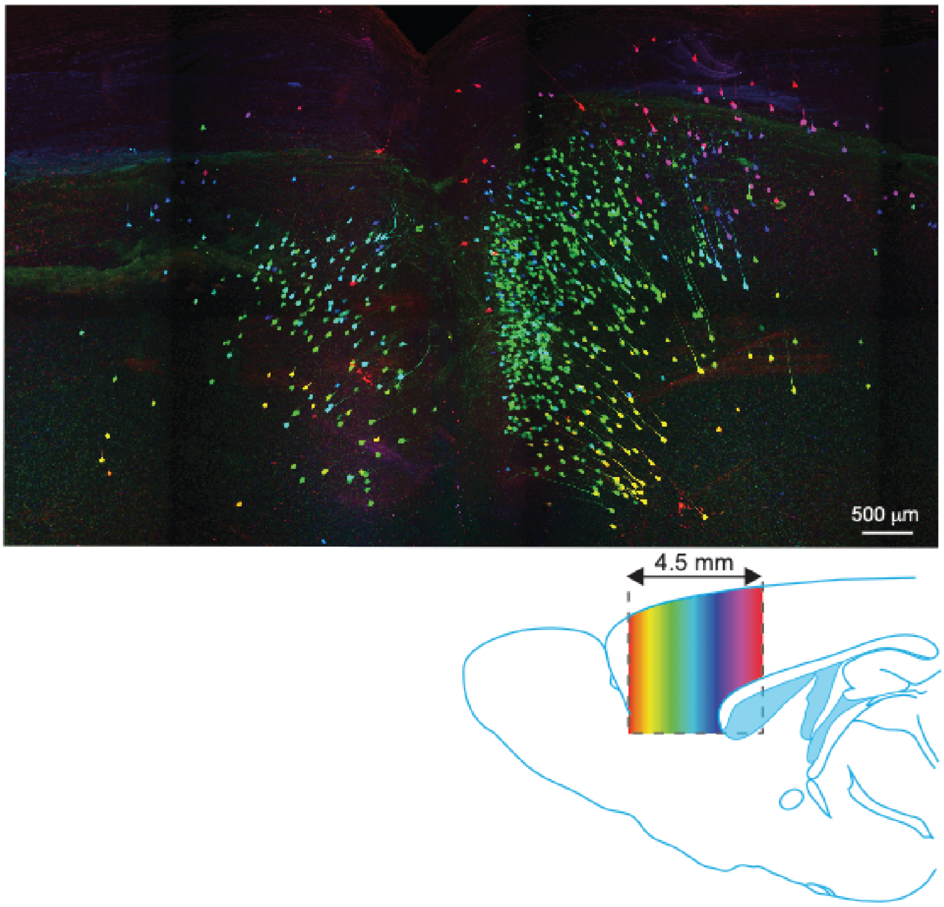

Figure 5-1 Serial 2 photon image of our animal model used for functional connectivity maps*. A rostral-caudal intensity projection of Inter Telencephalic (IT) neurons in the Prefrontal Cortex (PFC) obtained from serial 2-photon tomography imaging (TissueCyte image and figure credit to Dr Gerald Moore and Professor Stephen Brickley). In this figure, the right hemisphere is the injection (ipsilateral) hemisphere, and the left is the contralateral hemisphere which was the focus of local connectivity mapping paradigms. Inset on the bottom right is a sagittal cross-section illustrating the extent of the rostral-caudal intensity projection, as well as a colour code map noting IT neuron depths in the above projection. We see denser expression in the ipsilateral injection hemisphere relative to the contralateral hemisphere. Furthermore, going by colour we see that labelled IT neurons seem to occupy a similar coronal slice of the model.*

Figure 5-2 shows the cortical layer breakdown of labelled IT neurons in the same image set as Figure 6-1. We see a laminar distribution of IT neurons projecting to the injection site with contralateral IT neurons distributed across cortical layers. Hence, this model provides a sensible testing bed for our light patterning microscope: there is a relative sparsity of opsin expression which is beneficial considering the poor axial confinement of our light patterns and the expansive nature of dendrites which may be expressing opsin. Furthermore, the laminar distribution of expressing IT neurons means that if we found that opsin expression was too dense for functional mapping using our system, we could in principle move to inter-laminar IT neuron functional mapping and take advantage of the natural spatial segregation of neurons between cortical layers.

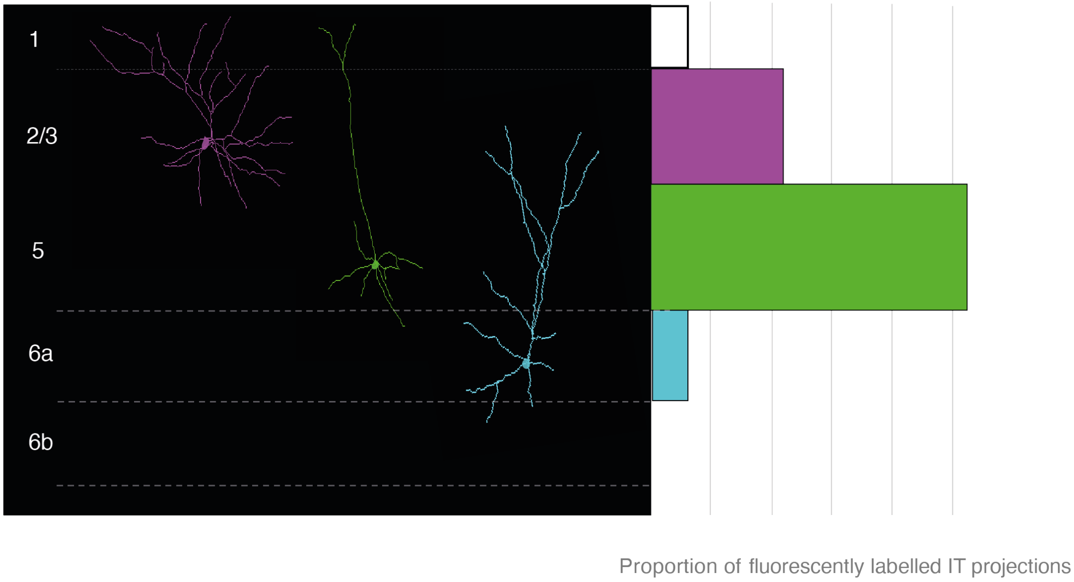

__Figure 5-2 Cortical layer breakdown of labelled Inter-Telencephalic (IT) neurons in the contralateral hemisphere of our animal model used in functional connectivity mapping experiments__. On the left we see traced neurons from each noted cortical layer, obtained using Simple neurite trace (ImageJ plugin). We see IT neurons distributed in layers 2/3, 5, and 6a; IT neurons are not seen in layer 1 to the histogram bar is represented in white. Layer 2/3 neurons are cell type 1, layer 5 neurons are slender tufted pyramid neurons, and layer 6a neurons are corticocortical neurons. Image and figure credit to Dr Gerald Moore and Professor Stephen Brickley.

5.2.3 OPTICAL FUNCTIONAL CONNECTIVITY MAPPING

For a discussion of optical functional connectivity mapping, please see Section 1.5. I discuss the various methods for optical mapping and weigh the experimental paradigm against patch clamp electrophysiology.

5.2.4 SPECIFIC CHAPTER AIMS

The overarching goal of this chapter was to use our light patterning system to map the local functional connectivity of Inter-Telencephalic (IT) neurons in the PFC. Broken down, the aims of this chapter were as follows:

1) Demonstrate that local functional connectivity amongst IT neurons exists using full Field of View photostimulation, pharmacological intervention, and whole cell electrophysiology. Specifically, I aimed to whole-cell voltage-clamp a ChR2-GFP expressing or non-expressing neuron situated amongst opsin expressing IT neurons. I would then photostimulate the entire FoV while centred on the patched neuron and look out for any stimulation-synced responses in the patched putative post-synaptic neuron. Finally, by pharmacological intervention I would block synaptic input on to the post-synaptic neuron, which would eliminate this stimulation- synced response and hence demonstrate that there is local functional connectivity.
2) Once aim 1 yielded positive results, I would then repeat the experiment, but before pharmacologically blocking any responses I would switch to single neuron precision functional mapping with the aim of finding any individual neurons which were functionally connected to the post-synaptic neuron. This would entail rapidly photostimulating putative pre-synaptic neurons in succession, with photostimulation parameters (spot size, pulse duration, and power density) which would, as discussed in Chapter 4, be theoretically suitable for evoking action potentials in the pre-synaptic neurons.

5.3 MATERIALS AND METHODS

For this chapter, animal and animal care information is detailed in Section 2.1. The ChR2 transgenic strategy and stereotaxic viral injection strategy are detailed in

Section 2.2.2. Solutions used for electrophysiology and tissue preparation are described in Sections 2.3.4-6; tissue slice preparation Section 2.4; and whole-cell electrophysiology procedures in Section 2.5.1. Note, the intracellular solution used in this chapter was the Caesium Chloride based solution. With respect to solutions in general, some pharmacological changes were made for the experiments in this chapter; one should take the solution compositions in sections 2.3.4-6 as the base ingredients list, with any additions for the following experiments described in the following methodologies.

Photostimulation pattern generation was achieved using the methodology described in sections 4.3.2-3- for the spatial and temporal control respectively. Light pattern power was controlled using the Polyscan GUI (Mightex, proprietary software).

5.3.1 LOCATING ANATOMICAL REGIONS FOR FUNCTIONAL CONNECTIVITY MAPPING

Locating promising regions for functional connectivity mapping was a challenging task. The methodology I followed was as such: first, navigate to the contra-lateral hemisphere relative to the retro-viral injection- this was done by keeping careful track of animal injection site, slicing procedures, and slice transferral such that we could keep track of which hemisphere was which. It was further confirmed by the expression profile of GFP in each hemisphere; the contralateral hemisphere expresses less opsin than the ipsilateral hemisphere. Next, I navigated to the approximate anatomical region in the PFC containing Layer 5/6 pyramidal neurons. This was done using the Allen brain atlas as guide (https://atlas.brain-map.org/). Once this had been done, the next task was selecting appropriate sets of neurons for functional connectivity assays.

5.3.2 SELECTING PUTATIVE PRE- AND POST- SYNAPTIC NEURONS FOR SINGLE NEURON PRECISION FUNCTIONAL MAPPING

Once at the correct anatomical region, the hunt for the “Goldilocks zone” begun: healthy neurons which were either ChR2-GFP positive or themselves surrounded by healthy looking ChR2-GFP positive neurons. The former case would yield data on many-to-one intra-functional connectivity amongst IT neurons, and the latter would provide control data on the local functional connectivity of IT neurons and non-IT neurons. Care was taken to avoid patching or photostimulating neurons with other GFP expressing neurons in the same axial column- this was due to the poor axial confinement of our photostimulation light and discussed in section 4.5. As it were, both cell health and ChR2-GFP expression were wildly variable (subjective measure expanded on in this chapter’s discussion) hence this process often warranted compromise on either factor. Indeed, as experimental time wore on the tissue slices would succumb to their fight against entropy and start to die; the sooner I selected a region the better.

Once an area was found and a target post-synaptic neuron was patched, I then moved on to photostimulation protocols. Note, in the context of these experiments when I refer to ‘post-synaptic’ neurons they are the patched neuron, and when I refer to pre-synaptic neurons they are considered putatively connected to the post-synaptic neuron and targeted for single-neuron precision photostimulation.

5.3.3 CHR2 EXPRESSION CONFIRMATION AND FULL-FIELD PHOTOSTIMULATION PROTOCOL

Due to expression variability, GFP signal was not a reliable measure of opsin expression. With this in mind I first moved the post-synaptic neuron in to the centre of the FoV and targeted its soma with a 10 µm photostimulation spot, after which I ran the same protocol for lateral spatial confinement characterisation as described in section 4.3. The subsequent observation of photocurrents (or lack thereof) would confirm whether or not the neuron was opsin positive.

Next, I photostimulated the full addressable area of the microscope's Field of View (FoV) using a 10 ms light pulse at a 5 Hz frequency and power density of 0.67 $^{mW}/_{\mu m^2}$. This was designed to maximise the likelihood of inducing photocurrents in opsin expressing neurons/processes within the FoV, and hence confirm functional connectivity.

With regards to the electrophysiology method used for this protocol, the post-synaptic neuron was held in voltage clamp at -70 mV, and the solutions used were stock solutions as described in 2.3.4-6. A CsCl based intracellular solution was used to reduce space-clamp issues thus allowing higher resolution readout of afferent mini Excitatory Post Synaptic Currents (mEPSCs). Further, all intracellular solutions were filled with 1 mg biocytin to attempt to reconstruct neuronal morphology for future imaging and structural connectivity assays (filling and slice preservation protocols are described section 4.3.10-11). A 1 kHz low-pass filter was applied to all electrophysiological data to help detect mEPSCs.

If a stimulus synchronised current response was observed in the post-synaptic neuron, functional connectivity within the FoV was inferred and I moved on to single neuron photostimulation procedures. If not, discarded the recording and moved on to another area and/or target post-synaptic neuron.

5.3.4 SINGLE NEURON PHOTOSTIMULATION PROTOCOLS

For experimental simplicity and to keep photostimulation light profiles identical, I laterally displaced the microscope stage to move target pre-synaptic neurons in to the centre of the microscope FoV. As noted, the target pre-synaptic neurons were in an ideal scenario clearly GFP fluorescent and healthy (subjectively speaking based upon many aeons worth of patching PFC neurons).

Once centred, the following protocol was run: a 5 μm spot was target directly to the cell soma, as photostimulated with light pulse durations of 10 ms at a rate of 1 Hz, with a power density of 0.128 ${}^{\mu\mathrm{W}}/_{\mu\mathrm{m}^2}$. This was repeated for at least 1 minute per pre-synaptic neuron. Further, a baseline recording was made whilst no photostimulation was happening- this was essentially a 151 s recording of spontaneous synaptic inputs into the postsynaptic neuron and would serve as a benchmark against which photostimulation epochs would be compared. Between these photostimulation epochs – which can also be considered pairing protocols- the recording quality of the post-synaptic neuron was monitored, and it was ensured that the series resistance and leak current had not increased. Finally, the lateral stage displacement required to centre pre-synaptic neurons in the FoV was tracked to gain data on the distance of pre-synaptic neurons from the post-synaptic neuron. Each putative pre-synaptic neuron was stimulated in series and selected randomly from the set of promising neurons in the FoV. Figure 5-3 shows a cartoon summarising this optical connectivity mapping paradigm.

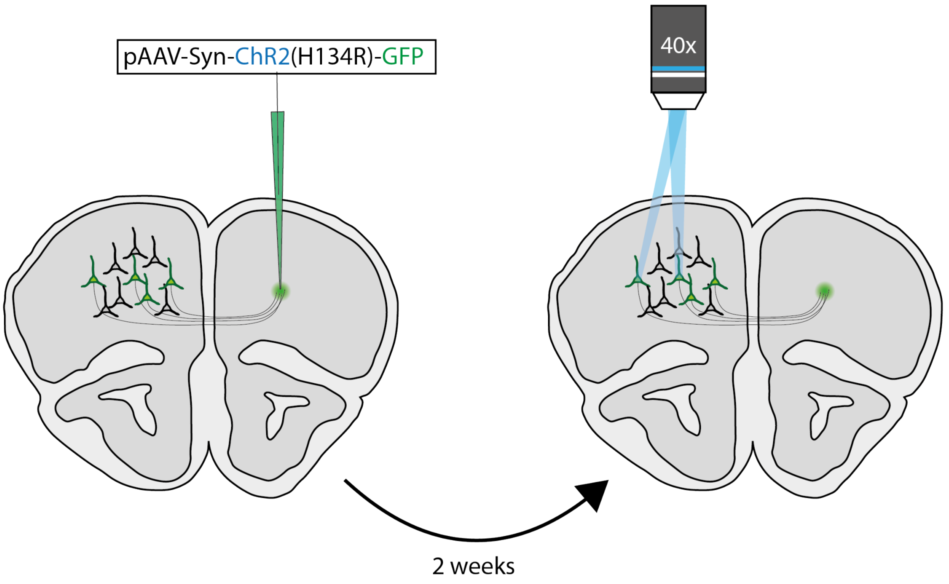
(a) retro viral injection and connectivity mapping

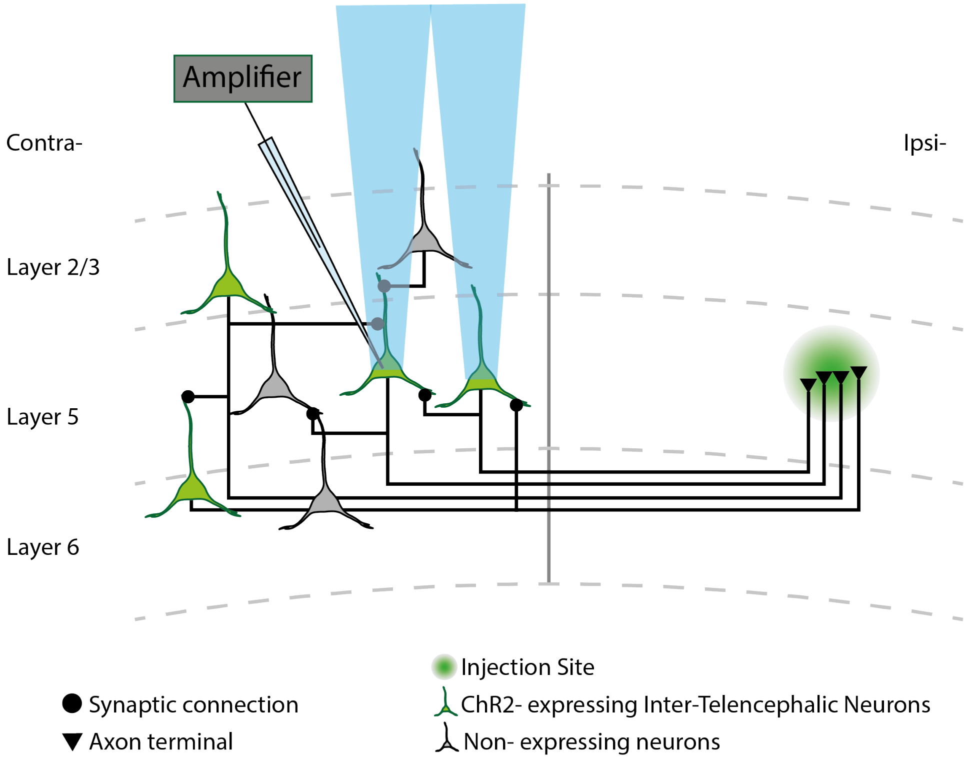
(b) single neuron precision optical connectivity mapping

Figure 5-3 Single neuron precision optical functional mapping schematic*.** ***a *A wild type, C57BL/6 mouse is unilaterally injected in the Prefrontal Cortex (PFC) using a retrovirus construct (pAAV-Syn-ChR2(H134R)-GFP, Addgene). Two weeks following injection, animals are sacrificed, and functional mapping experiments are carried out.* ***b*** *A schematic of the functional connectivity mapping protocol described in Sections 5.3.2-4. Ipsi- and contra- lateral hemispheres are labelled, as well as the laminar distribution of Inter Telencephalic neurons. In this figure, the right hemisphere is the injection (ipsilateral) hemisphere, and the left is the contralateral hemisphere which was the focus of local connectivity mapping paradigms.*

5.3.5 PHARMACOLOGICAL INTERVENTIONS TO PHOTOSTIMULATION PROTOCOLS

Tetrodotoxin

Tetrodotoxin (TTX, Merck) is a Sodium (Na) channel blocker and inhibits action potentials. Hence by adding TTX to the aCSF in the slice recording chamber one can stop any postsynaptic activity and in principle reduce photocurrent mediated pre-synaptic release on to post-synaptic synaptic terminals. With this in mind, after full FoV and single neuron precision photostimulation, I added 1 μM TTX to the aCSF to the recording chamber aCSF supply. I waited 5 minutes to allow the TTX to fully bind to Na channels before re-running full FoV photostimulation protocols as discussed above. The goal was to eliminate polysynaptic activity (that is, activity comprised of neurons within the local network activating one another as a downstream functional consequence of photostimulating the initial neuron- this could eventually lead to more afferent inputs to the patched neuron i.e. polysynaptic activity) and understand if future functional mapping procedures should by default utilise TTX; polysynaptic activity is a confounding variable for functional mapping assays.

4-Aminopyridine

4 - Aminopyridine (4-AP, Merck) is an antagonist of voltage-gated potassium (K) channels. Hence, it also helps inhibit any action potential initiation and propagation. It was added to aCSF to give a final concentration of 0.5 μM and was paired with TTX for the 'Area 2' functional mapping dataset of this chapter. This combination of chemicals together was meant to block any action potentials in the preparation whilst carrying out any functional connectivity assays. This would eliminate polysynaptic activity along with the addition of TTX but lead us to relying on sufficient depolarisation of the putative pre-synaptic neuron when photostimulated; in the absence of an AP the neuron could still release neurotransmitter if depolarised sufficiently- allowing still enabling functional connectivity experiments.

Kynurenic Acid

Kynurenic acid (Merck) is an antagonist of AMPA, NMDA, and Glutamate receptors. Hence, addition of the substance in to aCSF inhibits post-synaptic events. I aimed to 'spike' the bath with the substance to eliminate any photostimulation mediated responses in the patched neuron; if adding Kynurenic acid to the bath stops any response currents in the postsynaptic neuron following photostimulation of pre-synaptic neurons or more generally the microscope FoV, this can be seen as a confirmation of functional connectivity. This pharmacological intervention strategy was used for the 'Area 1' dataset of this chapter (described in 5.4). In practice, 100 µL of 2 mM Kynurenic acid was micro-pipetted into the recording chamber to bring the final concentration to 4 µM. Care was taken to not nudge any equipment or induce any turbulences in the aCSF whilst pipetting to minimise disruptions to the electrophysiological recording. This step was done *after* photostimulation epochs.

5.3.6 DATA ANALYSIS

Data analysis for this chapter was split in to two halves: mEPSC detection and characterisation, and general electrophysiological analysis and connectivity analysis.

mEPSC detection

mEPSCs were detected and characterised using the open-source software WinEDR (v 3.9.7, Strathclyde Electrophysiology Software). Raw electrophysiological traces were output from Signal (V6.05b, Cambridge Electronic Devices) and input in to WinEDR. WinEDR then output summary data frames which I then processed further using custom python scripts.

Cross-correlation analysis for single neuron functional mapping

Cross-correlation analysis aims to characterise the events (response) around a stimulus time- with the stimulus here referring to presynaptic photostimulation and response refers to mEPSC events. It takes the time of each event and subtracts it from the stimulus time, after which this difference is this plotted as a histogram. By using this analysis, I sought to view if there were any changes in peri-stimulus events between the different pre-synaptic neuron photostimulation epochs.

This analysis was done in python. I looked at time difference windows ±100 ms from the stimulus and plotted them for each photostimulation epoch.

General electrophysiological data analysis

Save for mEPSC detection and characterisation, I analysed all electrophysiological data using custom python scripts which read in raw recordings and processed them accordingly.

5.4 RESULTS

Results for this chapter are split across two data sets. The first, labelled 'Area 1', is a specific PFC region containing a non-expressing putative pyramidal neuron centred within the microscope Field of View (FoV – 198 µm x 345 µm) and is surrounded by opsin expressing processes and neurons as discerned by GFP signal. The second data set is labelled 'Area 2' and is taken from a second animal. It is another PFC area that is ostensibly similar to Area 1. Both tissue samples were obtained using the same methodologies- from animal care and transgenic strategy to tissue slice preparation. Finally, in both samples the non-expressing target cell was patched using the methodology used in Section 2.5.1. The recording was left in Voltage Clamp to monitor photocurrents or Excitatory Post-Synaptic Currents (EPSCs). The patched neuron is referring to the post-synaptic neuron, and any neurons targeted for single neuron photostimulation are referred to as putative pre-synaptic neurons.

5.4.1 AREA 1 MICROSCOPE FIELD OF VIEW

The first data set for this chapter is described at the beginning of this results section. The postsynaptic, patched neuron was a non-expressing neuron, as confirmed by both GFP signal and no direct photocurrents from single cell photostimulation. The IR and GFP FoV for this area are shown below in Figure 5-4.

(a) IR image of connectivty map FoV

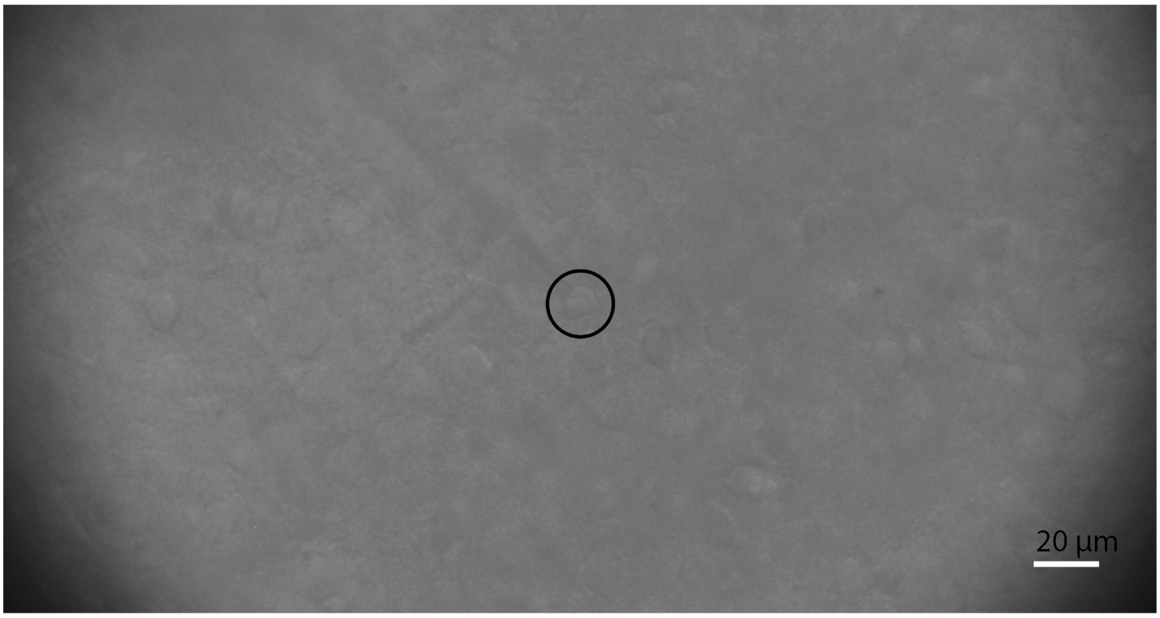

(b) 490 nm image of connectivty map FoV

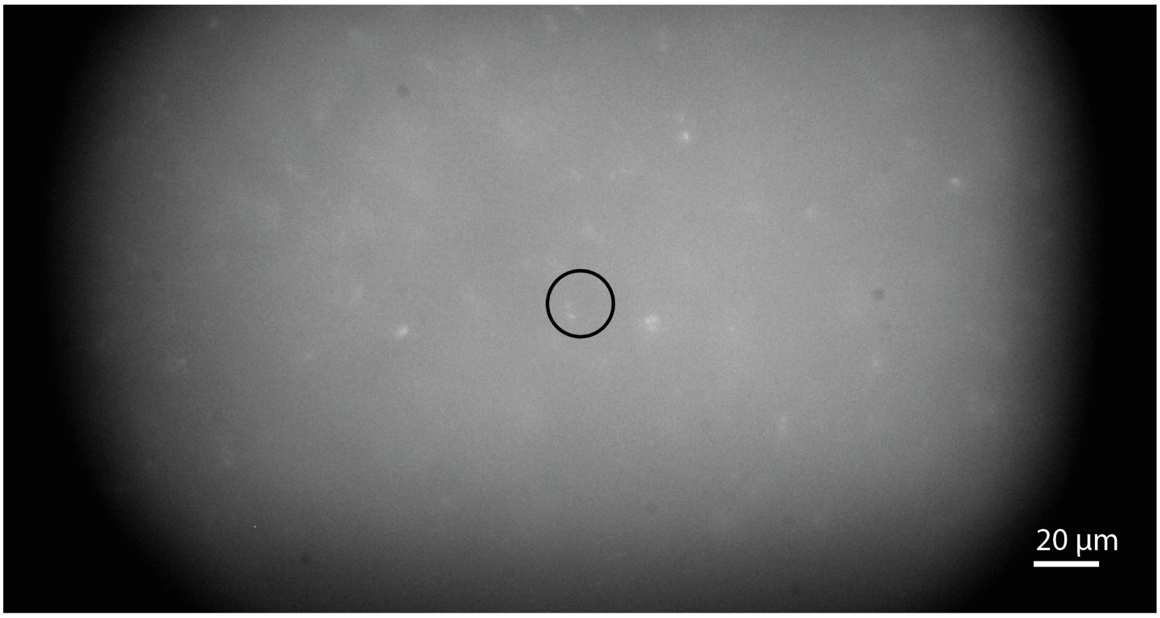

Figure 5-4 Area 1 Field of View and experimental functional connectivity map. *The microscope FoV shown by an IR image of the area* ***a****, and* ***b*** *490 nm image of the area. The patched, non- expressing post-synaptic neuron is circled with a 20 µm black circle. Scale bars are 20 µm. The FoV was 353 µm x 186 µm.*

5.4.2 AREA 1: FULL FIELD OF VIEW PHOTOSTIMULATION WITH TTX, 4-AP, AND KYNURENIC ACID CONFIRMS FUNCTIONAL CONNECTIVITY

Photostimulating the full addressable area of the microscope's Field of View (FoV) using a 10 ms light pulse at 5 Hz (vertical blue bars) demonstrates functional connectivity and polysynaptic activity following stimulation epochs. The power density of the photostimulation pattern was 0.67 mW/µm2. The raw electrophysiological traces are shown in Figure 5-5 below. Figure 5-5 a shows the response current whilst photostimulating the slice with aCSF containing 1 µM TTX and 0.5 µM 4-AP, and b shows the current response in the postsynaptic neuron after spiking the recording chamber with 4 µM 4-Aminopyridine to block any synaptic events in the post-synaptic neuron. We see that in b there is minimal discernible current response to photostimulation, serving as a confirmation of functional connectivity. We also note the 25 ms delay between photostimulation and response current in the postsynaptic neuron.

(a) 1 µM Tetrodotoxin (TTX), 0.5 µM 4-AP

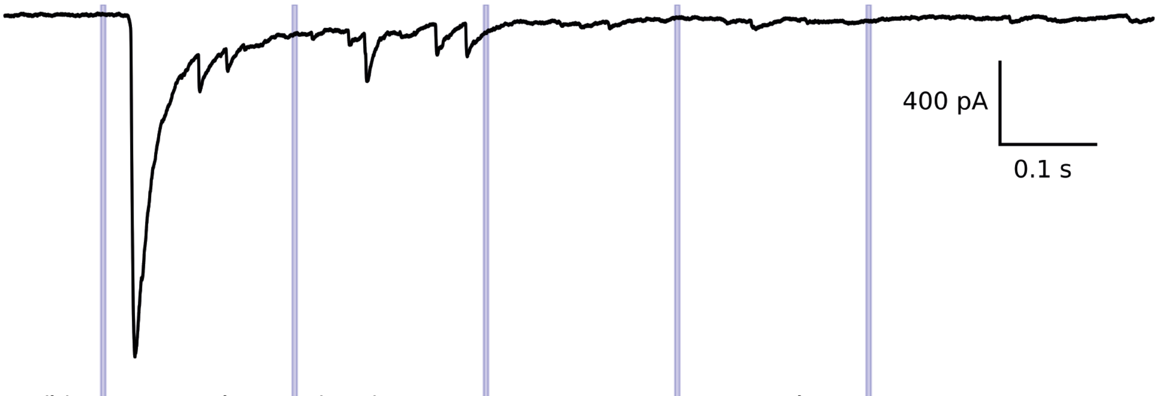

(b) 1 µM Tetrodotoxin (TTX), 0.5 µM 4-AP, 4 µM Kynurenic acid

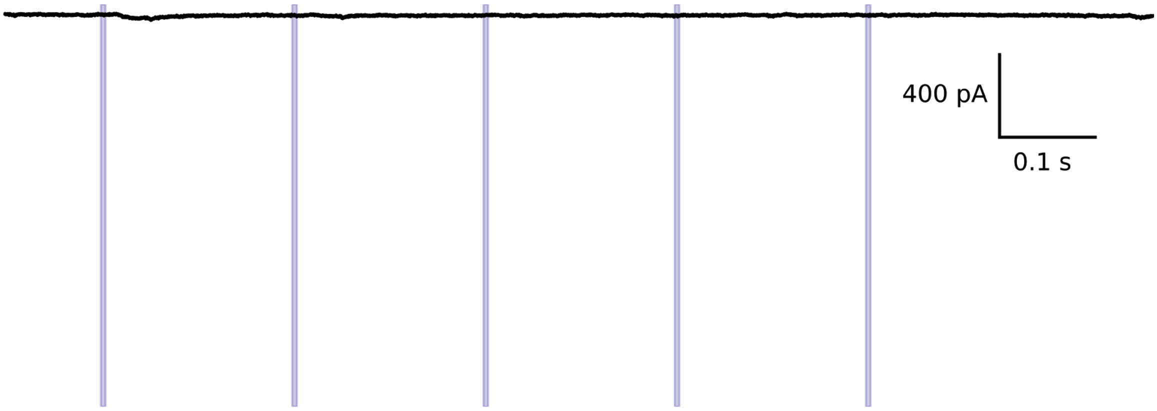

***Figure 5-5 Area 1 full Field of View photostimulation with Kynurenic acid spike confirms functional connectivity**. Photostimulating the full addressable area of the microscope's Field of View (FoV) using a 10 ms light pulse at 5 Hz (vertical blue bars) demonstrates functional connectivity and polysynaptic activity following stimulation epochs. The power density of the photostimulation pattern was 0.67 mW/µm2. **a** shows the response current whilst using aCSF containing 1 µM TTX and 0.5 µM 4-AP, and b shows the current response in the postsynaptic neuron after spiking the recording chamber with 4 µM 4-Aminopyridine to block any synaptic events in the post-synaptic neuron. We see that in **b** there is minimal discernible current response to photostimulation, serving as a confirmation of functional connectivity. We also note the 25 ms delay between photostimulation and response current in the postsynaptic neuron.*

5.4.3 AREA 1: FULL FIELD OF VIEW PHOTOSTIMULATION TRIAL OVERLAYS

The same raw traces for the dataset Figure 5-5 is shown in Figure 5-6. We see more clearly how there are time delayed current responses following photostimulation (Figure 5-6 a). We also observe asynchronous synaptic events. Figure 5-6 b then goes on to demonstrate that adding Kynurenic acid to the recording chamber eliminations any current responses in the post-synaptic neuron.

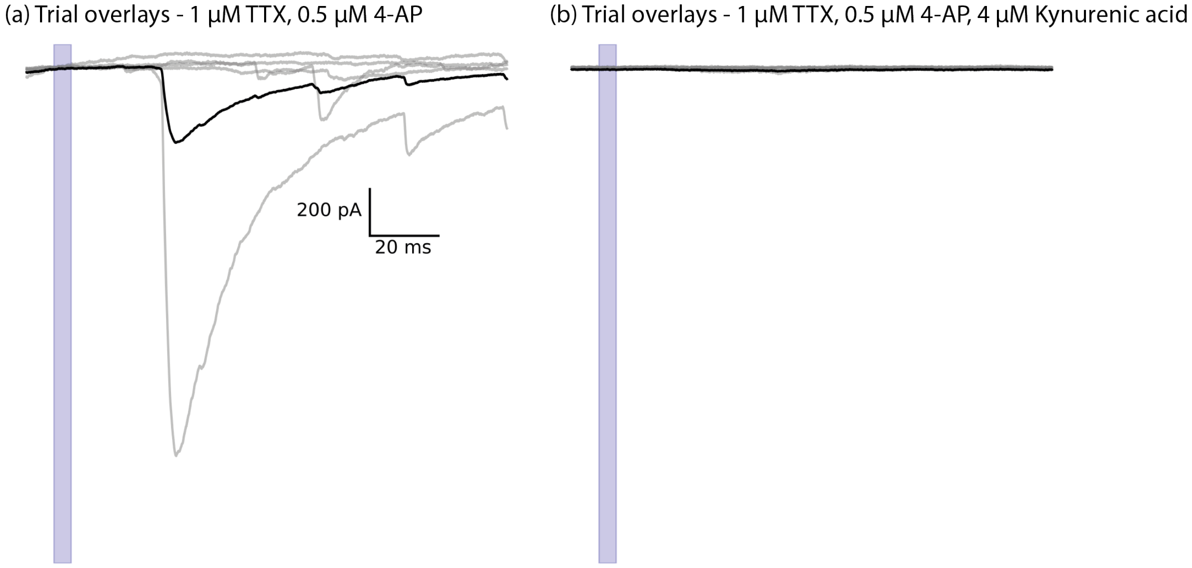

***Figure 5-6 Area 1: Full Field of View photostimulation trial overlays**. Trial overlays for full Field of View photostimulation using aCSF with **a** 1µM TTX and 0.5 µM 4-Aminopyridine, and **b** the same but with the addition of 4 µM Kynurenic acid. **a** shows a time delayed current response following photostimulation- in 2 of 5 trials. We also observe asynchronous synaptic events. **b** then goes on to demonstrate that adding Kynurenic acid to the recording chamber eliminates any photocurrent mediated current responses in the post-synaptic neuron, indicating functional connectivity between non-Inter-Telencephalic neurons and Inter-Telencephalic neuron.*

5.4.4 AREA 2 MICROSCOPE FIELD OF VIEW AND EXPERIMENTAL FUNCTIONAL CONNECTIVITY MAP

The microscope FoV and connectivity map for area 2 is shown in Figure 5-7. Figure 5-7 a shows an IR image of the area, and Figure 5-7 b shows a 490 nm image of the area. The patched, non- expressing putative pyramidal neuron is circled in black with a dimeter of 20 µm. Neurons which appeared GFP positive and hence photostimulated as potential pre-synaptic neurons relative to the patched neuron are circled in white, with diameters of 10 µm. Scale bars are 20 µm.

(a) IR image of connectivty map FoV

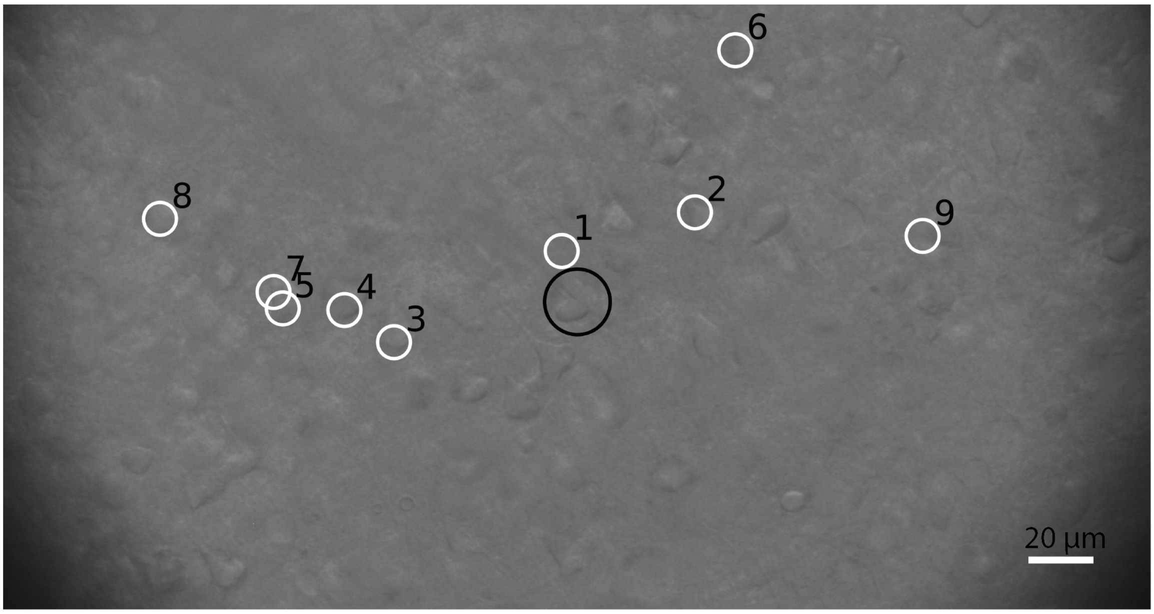

(b) 490 nm image of connectivty map FoV

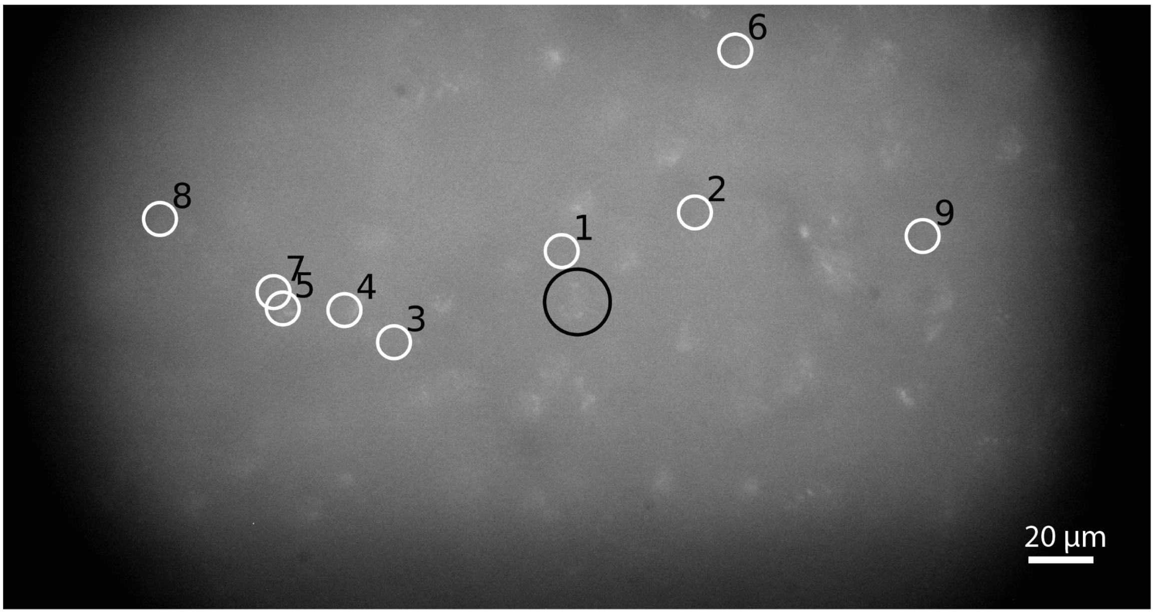

***Figure 5-7 Area 2 Field of View and experimental functional connectivity map. a** shows an IR image of the area, and **b** a 490 nm image of the area. The patched, non- expressing putative pyramidal neuron is circled in black with a dimeter of 20 µm. Neurons which appeared GFP positive and hence photostimulated as potential pre-synaptic neurons relative to the patched neuron are circled in white, with diameters of 10 µm. Scale bars are 20 µm. The entire field of View was 353 µm x 186 µm.*

5.4.5 AREA 2: DISTANCES OF PUTATIVE PRE-SYNAPTIC NEURONS FROM THE POST-SYNAPTIC NEURON

The distance of each putative presynaptic neuron targeted for single neuron precision functional connectivity mapping is summarised in table 5-1.

Presynaptic Neuron ID	X distance (μm)	Y distance (μm)	Z distance (μm)	Euclidean distance (μm)
1	4.8	15.5	0	16.23
2	-35.8	27.3	0	45.02
3	55.9	-12.3	0	57.24
4	71	-2.5	0	71.04
5	89.8	-2	0	89.82
6	-48.1	76.7	0	90.53
7	92.6	3	0	92.65
8	127.2	25.3	0	129.69
9	-105.2	20.1	0	107.10

***Table 5-1 Distances of putative pre-synaptic neurons from the post-synaptic neuron**. Distances were found by monitoring the lateral stage displacement when moving target neurons to the centre of the microscope Field of View. Note, a negative X distance means the neuron was to the right-hand side of the post-synaptic neuron relative to the image, and negative Y distance means the neuron was below the post-synaptic neuron.*

5.4.6 AREA 1: FULL FIELD OF VIEW PHOTOSTIMULATION SHOWS FUNCTIONAL CONNECTIVITY, AND POLYSYNAPTIC ACTIVITY

By photostimulating the full addressable area of the DMD as described in 5.3.3, I observed large, stimulus-synchronised response currents in the voltage clamped post-synaptic cell (Figure 5-8). Further, there were noticeable increases in asynchronous synaptic events suggesting polysynaptic activity induced by photostimulation. Adding 1 µM Tetrodotoxin (TTX) to the aCSF as described in 5.3.5 saw a noticeable decrease in asynchronous responses. Interestingly, it appeared that the first full FoV stimulation trial using TTX induced an action current in the patched neuron. This is discussed further in Section 5.5 of this chapter but in brief could indicate incomplete binding of TTX to Na_v channels.

(a) No pharmacological additions to bath

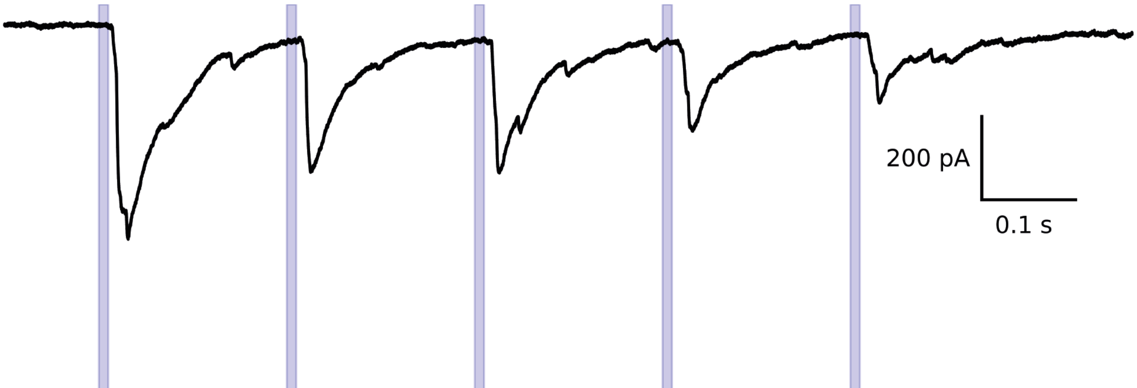

(b) 1 µM Tetrodotoxin (TTX) addition to bath

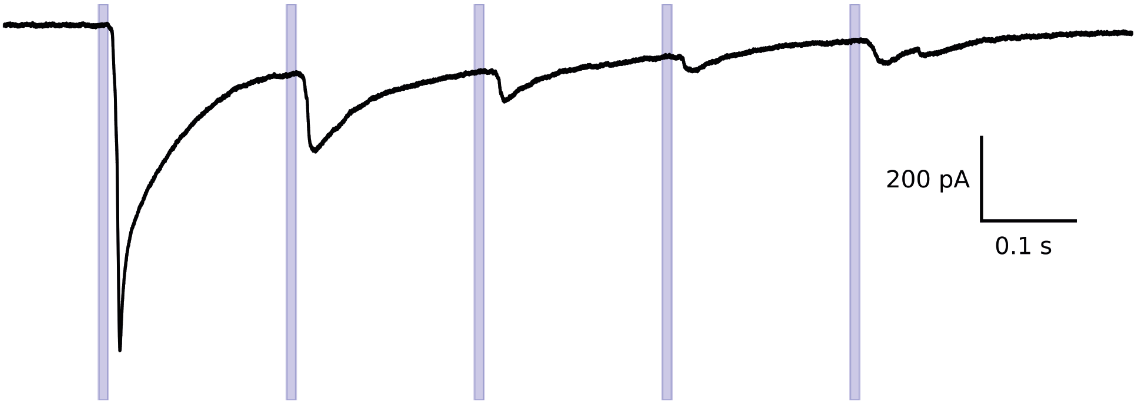

Figure 5-8 Area 2 Full Field of View photostimulation shows functional connectivity and polysynaptic activity*. Photostimulating the full addressable area of the microscope's Field of View (FoV) using a 10 ms light pulse at 5 Hz (vertical blue bars) demonstrates functional connectivity and polysynaptic activity following stimulation epochs.* ***a*** *shows the response current whilst using regular aCSF, and* ***b*** *shows the current response in the postsynaptic neuron after a 1 µM addition of Tetrodotoxin (TTX) to the recording chamber of the microscope. We see that in* ***b*** *there is a noticeable decrease in polysynaptic activity relative to* ***a****. The power density of the photostimulation pattern was 0.67 mW/µm2.*

5.4.7 AREA 2: FULL FIELD OF VIEW PHOTOSTIMULATION TRIAL OVERLAYS AND PEAK RESPONSE QUANTIFICATION

In the same data shown in 5.4.6, a desensitisation of current responses in the patched post-synaptic neuron was seen after sequential photostimulation trials. The simulation frequency was 5 Hz, with each stimulation epoch lasting 10 ms. Figure 5-9 shows a quantification of this observation.

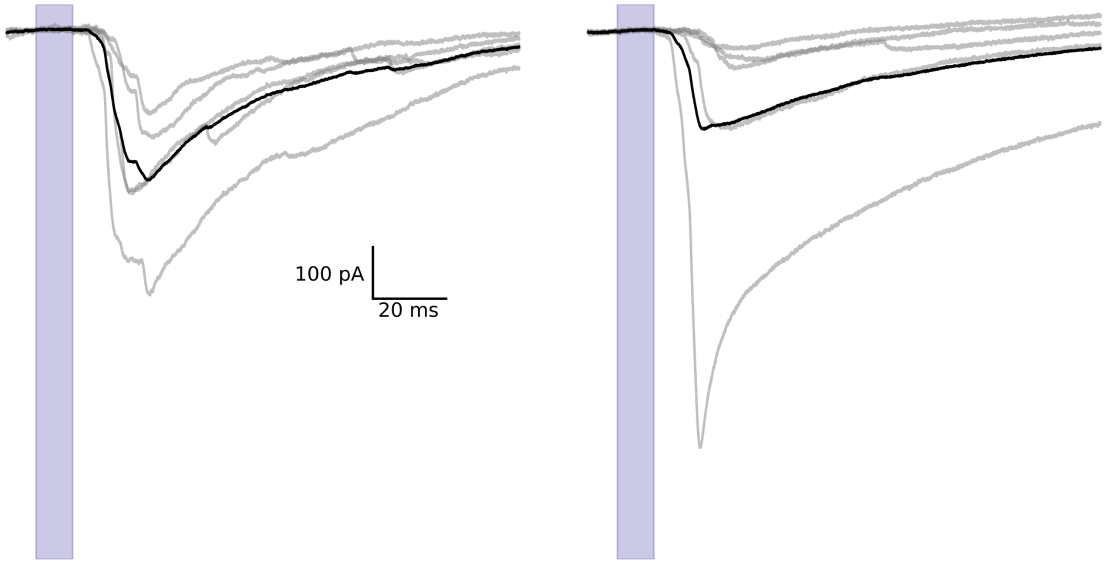
(a) Trial overlays - no pharmacology

(b) Trial overlays - 1 µM TTX

(c) Peak aggregate reponse - no pharmacology

(b) Peak aggregate response - 1 µM TTX

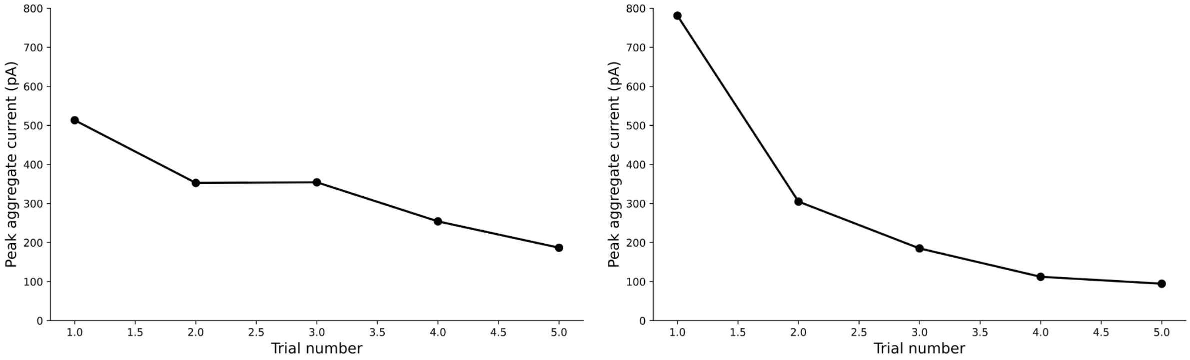

***Figure 5-9 Full Field of View photostimulation trial overlays and peak response quantification**. The peak aggregate current response in the post-synaptic neuron decreased with subsequent photostimulation trial. **a** and **b** show the single trial overlays in grey (no pharmacological intervention and with 1 µm Tetrodotoxin respectively), with and the trial averaged responses are in black (n = 5). **c** and **d** plot the quantified peak aggregate response of each trial.*

Once the full FoV response demonstrated that there was some form of functional connectivity within the addressable area of the microscope, I sought to map single-neuron resolution functional connectivity. Note, the TTX full FoV experiments in 5.3.6-7 above were done after these single neuron mapping experiments in order to allow photostimulation trials to evoke action potentials in putative pre-synaptic neurons.

5.4.8 AREA 2: SINGLE NEURON RESOLUTION CONNECTIVITY MAPPING – POST-SYNAPTIC NEURON MEPSC TRIAL OVERLAYS

The methodology for single neuron resolution functional connectivity mapping is described in section 5.3.4. Figure 5-10 shows the average trial overlays for each putative pre-synaptic neuron photostimulation epoch (neurons 1 -9), as well as the baseline trial overlays whilst not simulating anything. Light grey traces are single trials; black traces are trial averages across however many photostimulation trials were conducted on that particular neuron; grey shaded areas represent the standard deviation of the traces, and blue bars represent photostimulation epochs. Average traces in all recording epoch are seen to be almost flat, with no discernible response to the photostimulation epochs.

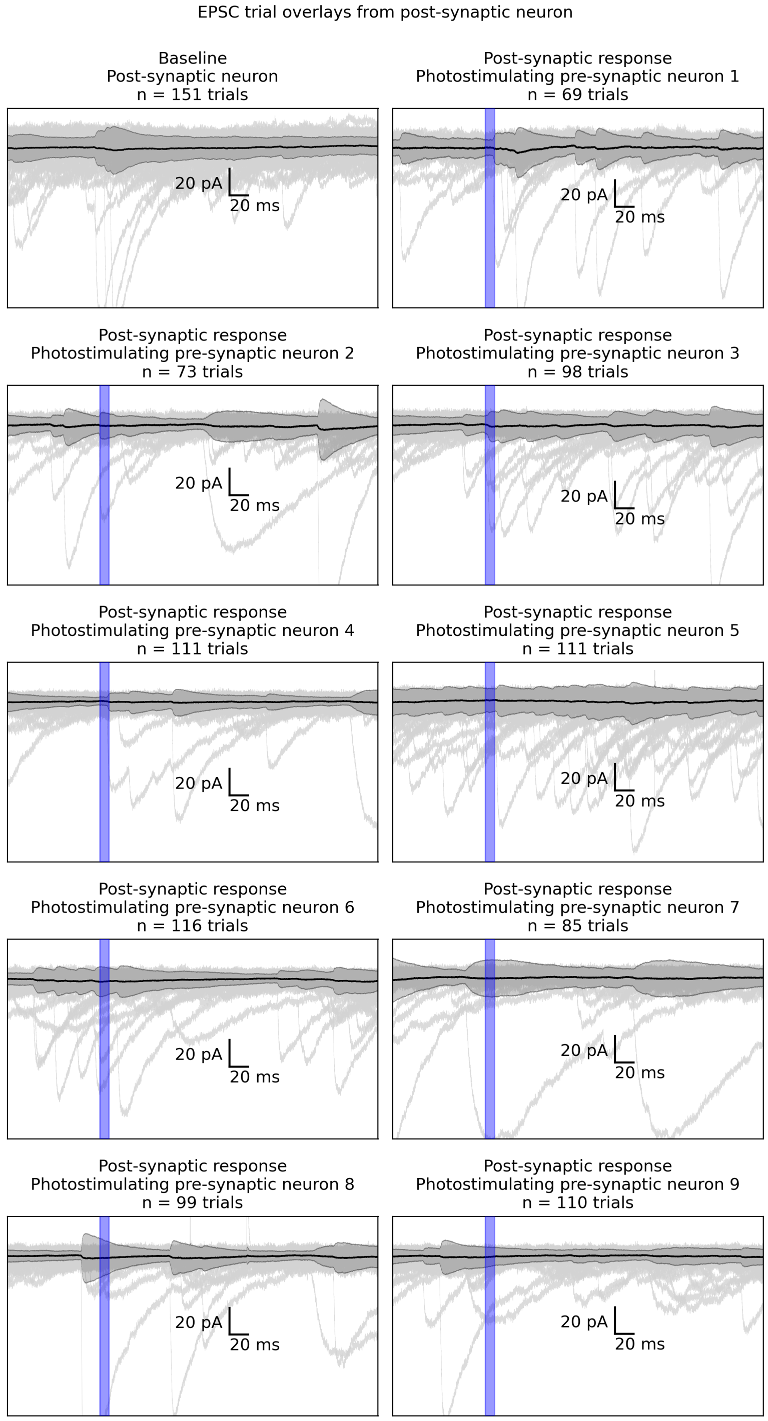

Figure 5-10 Single and average trial overlays for each pre-synaptic neuron photostimulation epoch*.* *The average trial overlays for each putative pre-synaptic neuron photostimulation epoch (neurons 1 -9), as well as the baseline trial overlays whilst not simulating anything. Each pre-synaptic neuron was stimulated with a 5 μm light spot with a power density of* $0.128\ ^{\mu W}/_{\mu m^{2}}$*, and a pulse duration of 10 ms with a frequency of 1 Hz. Light grey traces are single trials; black traces are trial averages across however many photostimulation trials were conducted on that particular neuron; grey shaded areas represent the standard deviation of the traces, and blue bars represent photostimulation epochs. Average traces in all recording epochs are seen to be almost flat.*

5.4.9 AREA 2: SINGLE NEURON RESOLUTION CONNECTIVITY MAPPING – POST-SYNAPTIC NEURON MEPSC AMPLITUDE DISTRIBUTIONS

Another metric for assessing functional connectivity is mEPSC amplitudes. The larger the AP or depolarisation of the pre-synaptic terminal, the larger the release of neurotransmitter, and hence larger the mEPSC on the post-synaptic neuron. Figure 5-11 shows normalised histograms of mEPSC events recorded in the post synaptic neuron during the set of photostimulation epochs. Plotted on top of each distribution is the Kernel Density Estimate for the data. Upon inspection, the distributions of each epoch look qualitatively similar. If there were functional connectivity, one might see a larger number of larger mEPSCs, or perhaps a larger number of events in general.

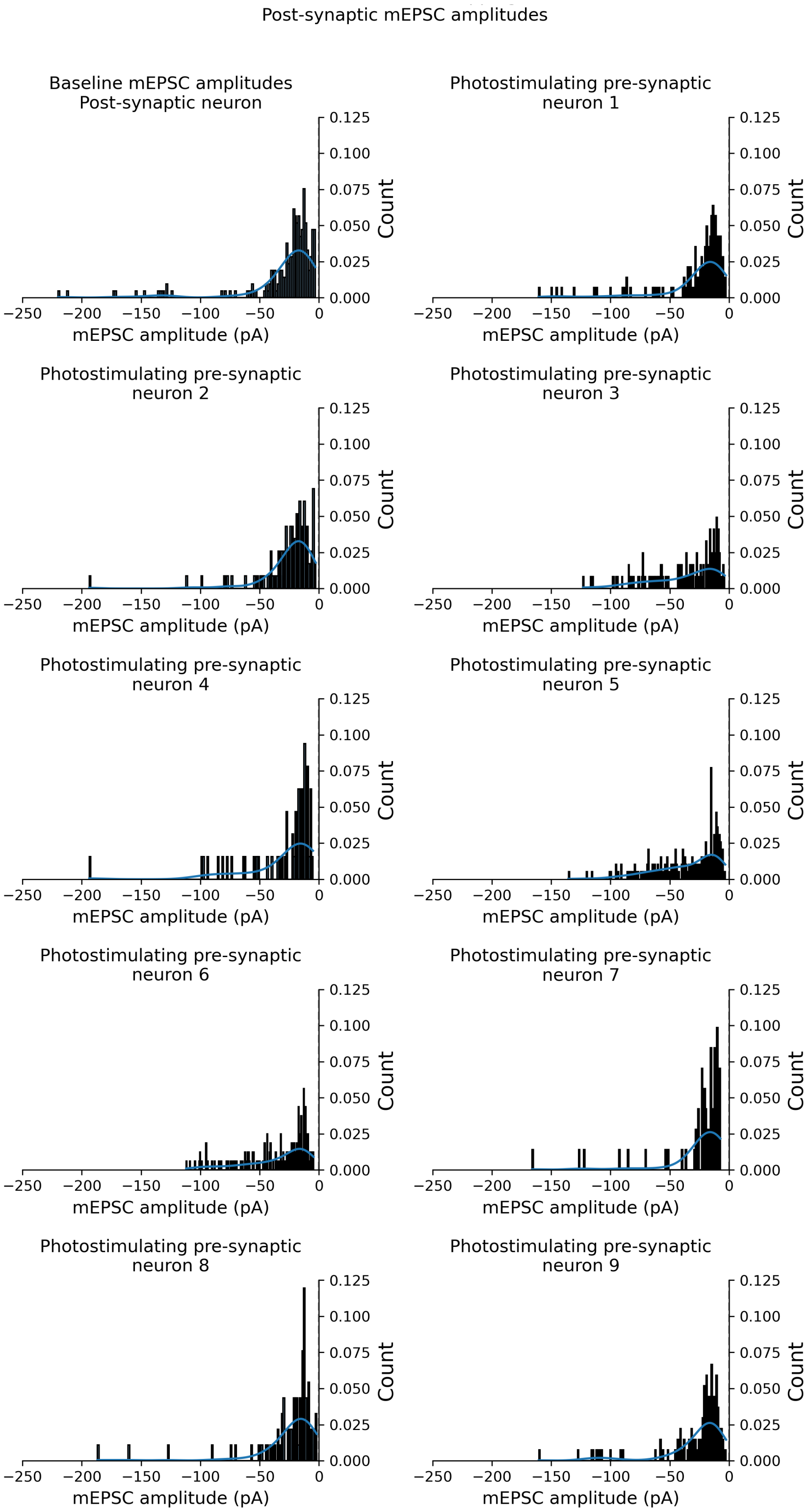

Figure 5-11 normalised mEPSC amplitude distributions recorded in the post-synaptic neuron for each photostimulation epoch*. Distributions are normalised to the recording duration each specific photostimulation epoch, either in the control with no photostimulation or whilst stimulating pre-synaptic neurons 1-9. The blue curves are the Kernel Density Estimates of the respective distribution. Single and average trial overlays for each pre-synaptic neuron photostimulation epoch.*

5.4.10 AREA 2: SINGLE NEURON RESOLUTION CONNECTIVITY MAPPING: POST-SYNAPTIC NEURON mEPSC CROSS-CORRELATIONS

As photostimulation could in principle affect the number of peri-stimulus mEPSC events in the postsynaptic neuron, I conducted a cross-correlation analysis as described in Section 5.3.6. The results are shown in figure 5-12, with each subplot once again showing the results from each photostimulation epoch, as well as the no-stimulation control.

We note that upon qualitative review of the data, there seems to be no difference between each epoch in terms of peri-stimulus event times and occurrences in general; we would expect to see more peri-stimulus events if there was a functionally connected, photostimulated pre-synaptic neuron. In attempt to quantify this, I decided to count the average number of events recorded in the 200 ms window post-stimulus.

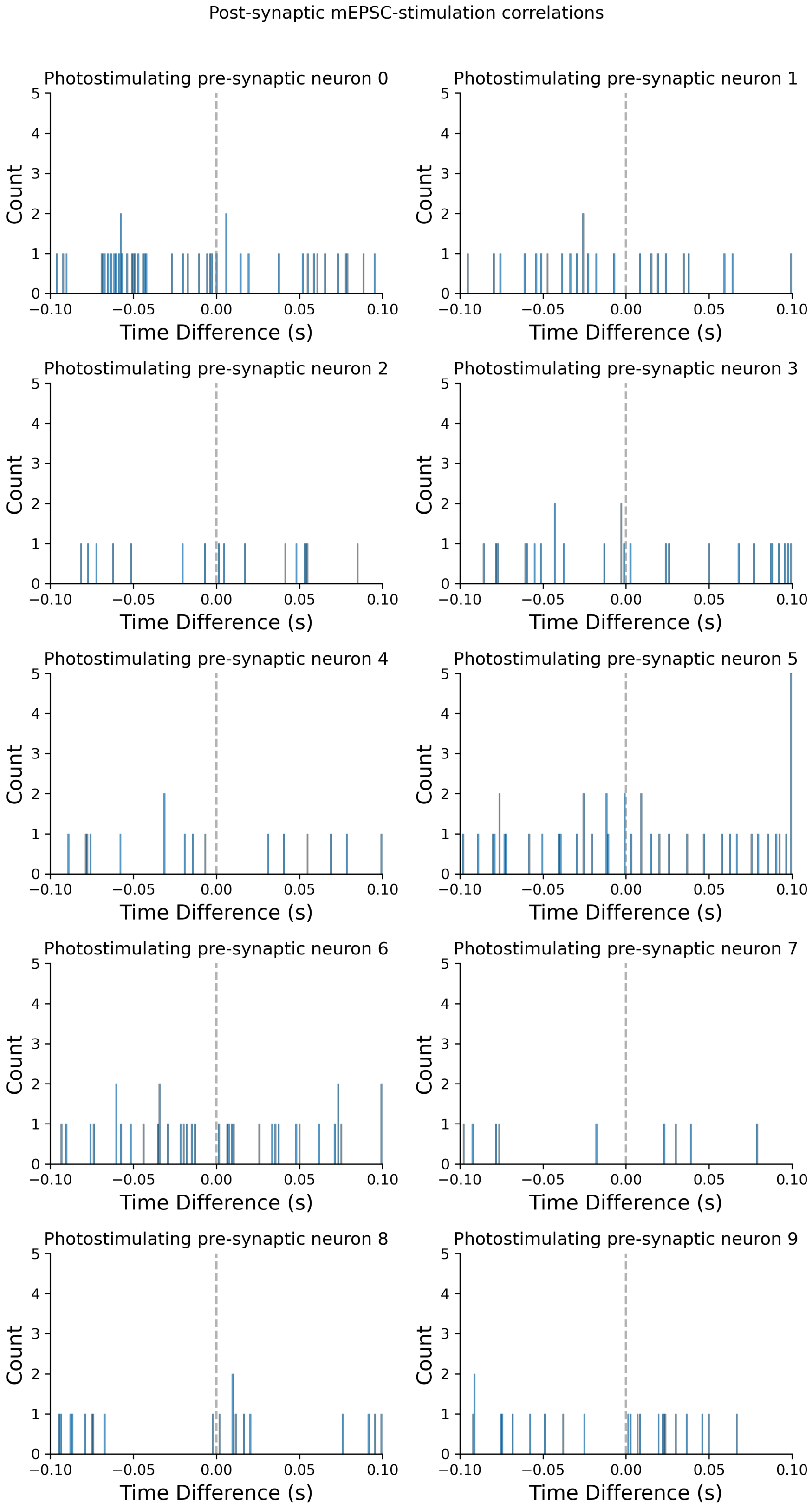

Figure 5-12 Cross-correlation analysis of peri-stimulus mEPSC events*. The dashed grey vertical lines mark the photostimulation time, and the x-axis spans ±100 ms from this time. Each plot is titled with the respective photostimulation epoch.*

5.4.11 AREA 2: NORMALISED NUMBER OF MEPSCS WITHIN 200 MS FROM PHOTOSTIMULATION

The normalised number of mEPSC events recorded in the post-synaptic neuron during each photostimulation epoch are shown below in Figure 5-13.

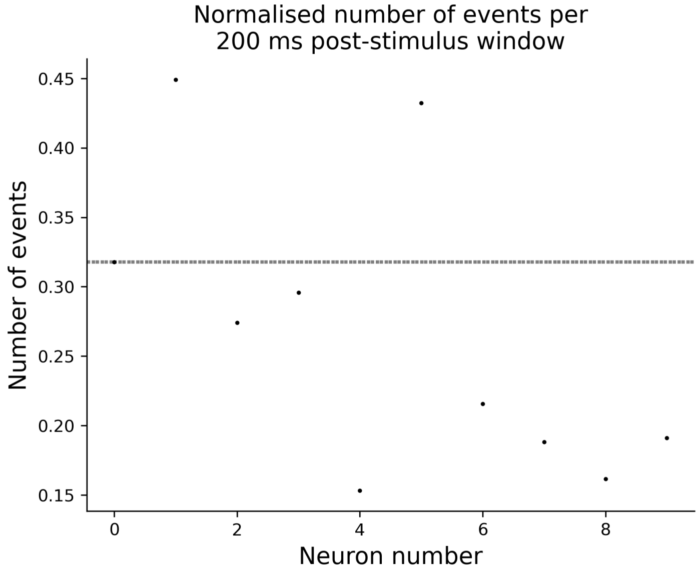

***Figure 5-13 Normalised number of mEPSC events per photostimulation epoch**. Neuron 0 represents the control recording with no photostimulation, and all other neurons are the same labelled putative presynaptic neurons in the preceding data. The horizontal dashed line represents the baseline mEPSC quantity.*

One can interpret figure 5-11 as the average number of mEPSCs recorded across all trials for each particular pre-synaptic neuron photostimulation epoch. We see that in 7 of the 9 epochs there is a smaller number of events recorded relative to the baseline recording.

5.4.12 AREA 2: mEPSC RATE VS. PRE-SYNAPTIC DISTANCE FROM THE POST-SYNAPTIC NEURON

Another parameter which has been shown to effect functional connectivity probability is distance between neurons. As such, I took careful note of these distance when photostimulating pre-synaptic neurons. Figure 5-14 shows the functional connectivity mapping data from area 1 sorted with respected to pre- and post- synaptic neuron distance. Note, the data point at 0 µm belongs to the baseline recording of the post-synaptic neuron itself whilst not photostimulation was happening.

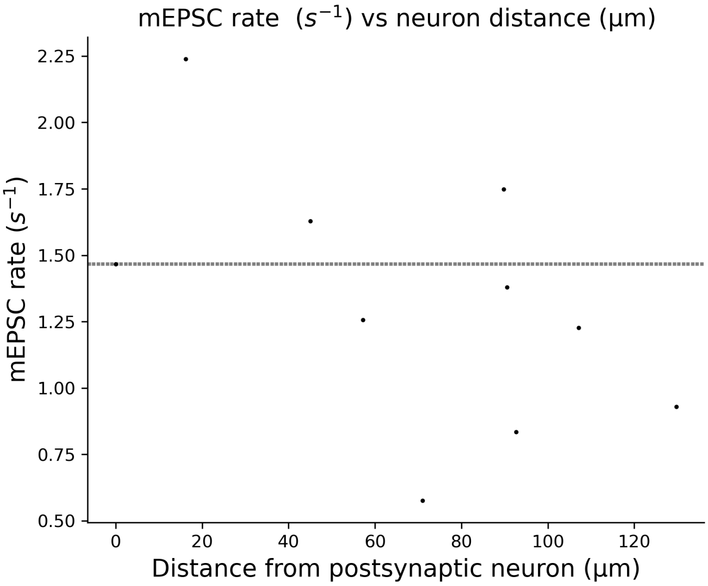

Figure 5-14 mEPSC rate vs. pre-synaptic neuron distance from the post-synaptic neuron. *The dashed horizontal line represents the baseline mEPSC rate whilst no photostimulation is occurring.*

It is seen that there does seem to be a downward trend in mEPSC rate as the distance of photostimulated neuron increases.

5.5 DISCUSSION

5.5.1 REFLECTIONS ON CHAPTER AIMS

I demonstrate local functional connectivity between Inter-Telencephalic and non-Inter Telencephalic neurons

I show using full field of view photostimulation at light power densities surpassing literature stated values for evoking APs in ChR2 expressing neurons that local functional connectivity from IT neurons to non-IT neurons exist. By pharmacologically blocking synaptic input in the post-synaptic patched neuron, I eliminated any photostimulation synchronised events in the non-expressing, postsynaptic neuron (Figure 5-5).

I found no evidence of single neuron precision functional connectivity in the subset of neurons tested

After verifying local functional connectivity in a second area, I attempted to map functional connectivity with single neuron precision. I saw no evidence of single connections between IT neurons and the post-synaptic, non-IT neuron. However, it is important to note that I did not assay every neuron within the microscope FoV hence cannot conclude that there were no single-neuron connections. The full field of view verification step (Figure 5-8) suggests that there were indeed functional synapses present in the field of view- these could in principle come from neurons outside of the tested FoV, or even from neurons which I simply did not test. The reason I did not was for fear of cell death; I deemed it more important to reseal the patched neuron and fix the sample in PFA (methodology in section 4.3.10-12) in the hope of gaining a morphological reconstruction of the neuron and the other putative presynaptic neurons. This way, I could try to get an idea of structural connectivity with the view of marrying structural and functional data, which in the idealistic experimental world would be the goal for all such connectivity mapping experiments.

5.5.2 FUTURE DIRECTIONS AND CONSIDERATIONS

There were 4 key challenges and limitations to the experiments conducted in this chapter, and they all point towards future directions of this work.

1) **No verification of putative pre-synaptic activity upon single neuron precision photostimulation**- be it spiking or subthreshold depolarisations. Without any direct verification of putative presynaptic activity following photostimulation, I was relying on measuring a postsynaptic response or a probabilistic inference of presynaptic activity which derives from a knowledge of photocurrent characteristics as a consequence of specific photostimulation paradigms. However, this methodology could certainly be improved. First, we could scale up the number of neurons patched or move towards an all-optical approach to optically readout pre-synaptic activity. This direction in particular will be discussed in the next chapter. Secondly, we need to gain a larger dataset containing expected photocurrents resulting from the set of photostimulation parameters (spot size, pulse duration, and power density) used, as well as a measure of spiking probability given these parameters. In this way we can start to quantify the likelihood of pre-synaptic response to photostimulation. For instance, if we find that given a specific combination of photostimulation parameters that there is a 90 % chance of evoking an AP in IT neurons using our animal model, and we conducted 100 pairing trials, we could infer that there were 90/100 trials which evoked an AP if the neuron was expressing ChR2 91. Indeed, this was the original plan but unfortunately circumstance dictated otherwise.

2) **It was a many-to-one mapping paradigm**, which doesn't consider bidirectional functional connectivity or many-to-many functional connections. We could scale

up the number of patched cells- even adding one more recording channel could help to rapidly assay functional connectivity in our model. Once again, taking an optical approach could bypass this limitation completely and bring us towards the domain of many-to-many functional mapping paradigms- though this will be discussed in more fully in Section 6.5.2.

3) **Expression variability and cell health**. This factor was perhaps the biggest roadblock faced- we observed variable opsin expression, inconsistent GFP signal, and consistent poor cell health. In terms of GFP signal, it was most often the case that the fluorescent neurons were dead, and non-fluorescent appearing neurons were sometimes ChR2 expressing. This suggests that opsin expression was bad for brain slice and neuron health- perhaps due to excitotoxicity and/or over expression. Furthermore, it became quickly apparent that we couldn't necessarily rely on looking for GFP and hence ChR2 expressing IT neurons for functional mapping experiments. Hence, going forward I suggest two strategies. First, optimising viral injection protocols, to find the optimal viral titre, injection rates, and expression time post-surgery. It could have been that the two-week wait time was too long, and overexpression proved detrimental to neuronal health. Second, we could attempt to slice in the dark with red light sources to guide our dissections. This will minimise, if not stop, actuation of ChR2-mediated currents hence minimising the effects of excitotoxicity arising from stray light.

4) **Poor axial confinement of light spots**. Though this particular limitation was known from the get-go, it was an inherent shortcoming of the illumination strategy. Single photon light sources like the one used for this in microscope have poor axial confinement. This can, however, be either worked around or eliminated as an issue. We could intentionally map the functional connectivity of neurons which have a natural spatial separation- for instance the inter-laminar IT neurons described in Section 5.2.2. Alternatively, we could switch to 2-photon modalities which due to the underlying physics have high axial confinement and optical

sectioning capabilities (discussed in Section 1.4.3). However, this would mean changing the optical system entirely so is perhaps less of a practical route.

Overall, I conclude that while the datasets obtained for this chapter were limited due to many factors, our light patterning system is indeed capable of single neuron precision optical functional mapping of IT neurons in our specific animal model. However, within specific bounds considering the poor axial confinement of our spots, and with room for improvement as discussed above.

CHAPTER 6

ALL-OPTICAL CROSSTALK-FREE MANIPULATION AND READOUT OF CHRONOS EXPRESSING NEURONS

Foreword note: this chapter is minimally adapted from my publication: "All-optical crosstalk-free manipulation and readout of Chronos-expressing neurons" [57]. The publication is permissioned for use under the terms of the Creative Commons Attribution 3.0 licence. The methods and results sections remain largely the same, whilst other sections have been adapted to help fit the narrative of this thesis.

The author contributions for the publication were as follows: experimental planning was conducted by myself (NS) and Dr Foust (AJF); experimental execution was conducted by NS, with exception of the TTX experiments which were conducted by Dr Peter Quicke (PQ); data analysis was conducted by NS, with checks and TTX data analysis by PQ; figure creation was done by NS; manuscript writing was done by NS and AJF. At all stages AJF provided oversight and guidance, along with Prof Simon Schultz.

6.1 ABSTRACT

All-optical neurophysiology allows the manipulation and readout of neural activity with single cell spatial precision and millisecond temporal resolution. Such experimental paradigms are built upon two strategies: optical perturbation of neuronal activity, and optical readout of neuronal activity. For the former, neurons can be made to ectopically express proteins which, upon light absorption, can actuate transmembrane currents. This allows optical control of membrane potential and Action Potential (AP) signalling. For the latter, neurons can be genetically or synthetically labelled with fluorescent reporters of cellular activity including membrane potential, calcium dynamics, or even neurotransmitter release. Combining these two paradigms one can optically assess the functional architectures of neuronal microcircuits.

However, to optically manipulate and readout neural activity in parallel, two spectra are involved: the action spectrum of the actuator, and the absorption spectrum of the fluorescent reporter. Crucially, overlap, or crosstalk, between these spectra can cause unintended artefacts in either direction. At time of writing the paper that this chapter was based upon, previous all-optical approaches had been hindered by unintended photostimulation of neural activity by light intended for activity readout.

Here, we pair the blue-green absorbing optogenetic actuator, Chronos, with a synthetic, deep red-emitting fluorescent calcium reporter CaSiR-1. We show that cultured Chinese hamster ovary cells transfected with Chronos do not exhibit transmembrane currents when illuminated with wavelengths and intensities suitable for exciting one-photon CaSiR-1 fluorescence. We then demonstrate crosstalk-free, high signal- to-noise ratio CaSiR-1 red fluorescence imaging at 100 frames s^{-1} of Chronos-mediated calcium transients evoked in neurons with blue light pulses at rates up to 20 Hz. These results indicate that the spectral separation between red light excited fluorophores, excited efficiently at or above 640 nm, with blue-green absorbing opsins such as Chronos, is sufficient to avoid spurious opsin actuation by the imaging wavelengths and therefore enable crosstalk-free all- optical neuronal manipulation and readout.

6.2 INTRODUCTION

This introduction focusses on the concept of all-optical neurophysiology, the, optical crosstalk, and specific chapter aims. For a more detailed introduction to optogenetics including the underlying science behind optically perturbing and reading out neural activity, please see Section 1.4.

6.2.3 ALL-OPTICAL NEUROPHYSIOLOGY

The ability to optically perturb and read out neural activity offers an incredible opportunity for neuroscience[47,86,119,120]. As discussed in Section 1.4, neurons can be made to ectopically express light-sensitive ion channels or pumps (opsins) to control their activity[49–51]. Furthermore, they can be synthetically[52] or genetically labelled[53,54] with activity reporters that convert biophysical markers of cellular activity such as changes in intracellular calcium concentration[55,56] or membrane potential[53] into a change in fluorescent signal (paragraph adapted from[57]). Combining these two strategies yields a powerful tool for functional connectivity mapping experiments and experimental neuroscience more generally, but there are many engineering challenges to be faced before this potential is fully realised. One such hurdle is optical crosstalk.

6.2.4 OPTICAL CROSSTALK

All-optical neurophysiology requires careful consideration of optical spectra. Both the opsin and the activity reporter are sensitive to specific spectra of light, and if there is an overlap between these spectra this can lead to inadvertent photostimulation by the light intended for activity readout, or optical artefacts appearing on the readout signal. Though the latter can be accounted for and subtracted from activity signals, the former presents a problem as unintended photocurrents could have a real effect on network activity, thereby adding a confounding variable to any optical neurophysiology experiments- for instance in connectivity[104] or plasticity[121] experimental paradigms.

6.2.5 JUSTIFICATION OF OPSIN AND ACTIVITY REPORTER CHOICES

We chose to pair Chronos, highly light sensitive opsin variant, with CaSiR-1. The rational for both are as follows: Chronos is a light efficient opsin able to generate larger photocurrents than other variants[50]. At time of writing this manuscript, it was actually the most light-sensitive opsin reported in literature. This was important as using Chronos meant that one could in principle target more neurons in parallel without increasing illumination light intensities. It also meant that one could follow experimental pathways requiring precise, millisecond control of neuronal activity, for example, Spike Timing Dependent Plasticity (STDP)[14] pairing protocols.

We selected CaSiR-1[122] after a literature review of all available red-light sensitive activity reporters that we could find. The rationale was to select reporters which had excitation and emission spectra red shifted away from Chronos' action spectrum such that exciting the reporter fluorophore would not actuate Chronos. Consideration was also put into reporter kinetics; we wanted to ensure that the calcium indicator did not chelate Calcium for too long (i.e., had a dissociation constant which was small enough such that we could image it's change in fluorescent profile, but large enough such that the reporter would minimally affect natural calcium signalling in tagged neurons. But more on this in the discussion).

6.2.6 SPECIFIC CHAPTER AIMS

Overall, this chapter aimed to demonstrate a strategy for all-optical neurophysiology, free from optical crosstalk between the photostimulation and activity readout channels. We chose to pair Chronos, a sensitive opsin variant with large photocurrents, with CaSiR-1, a synthetic deep-red emitting calcium reporter. The chapter aims can be broken down in to three sections:

1) To design and implement an all-optical neurophysiology system with two separate light paths: one for stimulating Chronos, and one for CaSiR-1 imaging.
2) To demonstrate that red light suitable for CaSiR-1 imaging does not evoke photocurrents in Chronos expressing Chinese Hamster Ovary (CHO) cells.
3) To demonstrate all-optical, crosstalk-free neurophysiology in acute brain slices using our chosen opsin, activity reporter, and optical system.

6.3 MATERIALS AND METHODS

For this chapter, animal and animal care information is detailed in Section 2.1. The mouse transgenic strategy for expressing Chronos in layer 2/3 pyramidal neurons is described in section 2.2.2. Solutions used for CHO electrophysiology is described in 2.5.1, and brain tissue preparation is described in Sections 2.5. Note, the intracellular solution used in this chapter was the K-Gluconate based solution. Further, please note that this methods section is minimally edited from my publication; the original text was written by myself with input and editing by Dr Amanda Foust. Optical designs were by Dr Foust and me.

6.3.1 CHINESE HAMSTER OVARY (CHO) CELL CULTURE AND TRANSFECTION

Chinese Hamster Ovary (CHO) cells were cultured in Dulbecco's modified Eagle medium (DMEM)/F-12 medium (21331020, Thermofisher) with the following additions: 10% (volume/volume) fetal bovine serum (F7524, Sigma-Aldrich), 1% (volume/volume) penicillin/streptomycin (P4333, Sigma-Aldrich), and 2mM L-glutamine (G7513, Sigma-Aldrich).

Before transfection, CHO cells were seeded onto cell culture treated plastic coverslips (174950, Thermonox). Once the seeded cells reached between 50%–80% confluency, they were transfected with the FCK-Chronos-GFP plasmid (1 µg per 120 000 cells) using a lipofectamine LTX reagent (15338030, Thermofisher). The transfection protocol was optimised to maximise transfection efficiency and final cell health, yielding the following ratio of plasmid to transfection reagents: 1 µg plasmid to 1 µl PLUS reagent to 3 µl lipofectamine LTX reagent. For the entirety of the 4h transfection period, the culture medium was replaced by opti-MEM reduced serum medium (31985070, Thermofisher), after which the culture medium was changed back to the full DMEM/F-12 media. During the cell culture and transfection periods, the cells were incubated at 37 °C in a 95%/5% O2/CO2 environment.

Prior to experimentation, we checked the transfection efficiency by imaging the GFP conjugated to Chronos with an inverted immunofluorescence microscope. All electrophysiology (section 2.5.1) and photostimulation experiments (6.3.3) were undertaken 24–48h after transfection to allow enough time for robust Chronos expression.

6.3.2 OPTICAL SYSTEM

Our photostimulation and epifluorescence imaging system integrated spectrally distinct red and blue illumination paths. Figure 6-1 a shows the optical path schematic and figure 6-1 b shows the relevant spectral characteristics for our all-optical approach.

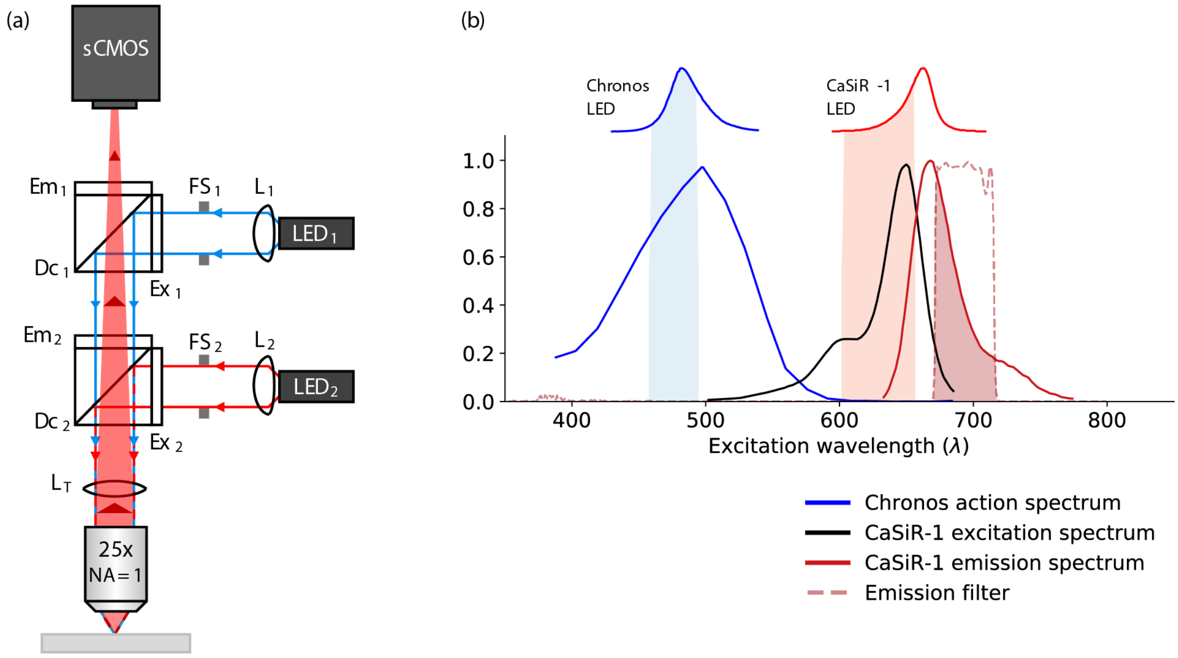

***Figure 6-1 All-optical photostimulation and epifluorescence imaging system**. For photostimulation, a 490 nm light emitting diode (LED, M490L4, Thorlabs) was collimated with an f = 16 mm aspheric con- denser lens (ACL25416U0-A, Thorlabs) and directed into a filter cube containing a 475/28nm excitation filter (FITC-EX01-CLIN-25, Semrock), 515nm long pass emission filter (FF01-515LP, Semrock), and 495 nm long-pass dichroic (FF495-Di03, Semrock). The blue light spectral output of the blue LED is shown in Figure 6-1 **b**, labelled 'Chronos LED'). The peak of this distribution is 482nm, and the expected value is 480nm. This LED was selected as its emission spectrum overlaps with the peak of Chronos' action spectrum. For imaging, a 660 nm LED (M660L4, Thorlabs) was collimated using a second f = 16 mm aspheric lens and directed into a filter cube containing a Cy5 filter set: 628/40nm excitation filter (FF02-628/40-25, Semrock), 692/40nm emission filter (FF01-692/40-25, Semrock), and 660nm long-pass dichroic (FF660-Di02-25x36, Semrock). The red-light spectrum is similarly shown on Figure 6-1 **b**, labelled 'CaSiR-1 LED'. This LED and the excitation filter were selected as they result in efficient excitation of CaSiR-1 fluorescence at its peak whilst avoiding the red tail of Chronos' action spectrum. The sample plane was imaged by a sCMOS camera (512 x 512 pixels with 4 x 4 binning, Orca Flash 4 V2, Hamamatsu). L_T represents a 180 mm tube lens to account for the infinity corrected objective.*

6.3.3 CHO CELL PHOTOSTIMULATION

Healthy CHO cells were identified using transmitted oblique- contrast infrared light (M780LP1 or M850L3, Thorlabs). Cell health was subjectively determined following many attempts at patching the cells; success and failures proved a good heuristic to finding healthy cells. Descriptively, healthy cells were not shrivelled, had no areas of high contrast, and were generally surrounded by other healthy cells. Following this, target cells were exposed to a 5 ms blue LED light pulse to check for GFP and consequently Chronos expression. If the cell was both healthy and Chronos- expressing, it was patch clamped as described in section 2.2.

During voltage-clamp recordings we interleaved sets of red (644nm average wavelength) and blue (480nm average wavelength) photostimulation trials, beginning with a set of blue pulses to check for the presence of photocurrents. LED intensities stepped between 0.28 $^{\mathrm{mW}}/_{mm^2}$ and 11.3 $^{\mathrm{mW}}/_{mm^2}$ were randomised and deployed onto the patched cells, each with a pulse duration of 5 ms. If photocurrents fell to below 90% of the values measured in the first set, this was seen as a marker of declining cell health and/or patch quality, and subsequent trials were excluded from the final analysis. LED control signals and photocurrents were recorded in Spike2 and analysed with custom-written python scripts.

6.3.4 BRAIN TISSUE SLICE PREPARATION AND CASIR-1 DYE LOADING

Following tissue preparation and the 1h resting period describe in section 2.4, brain slices were loaded with CaSiR-1 AM dye. 50 µg of CaSiR-1 AM was dissolved into a 10 µl dimethyl sulfoxide (DMSO) solution to which we had previously added 10% weight/volume Pluronic F-127 (Invitrogen) and 0.5% volume/volume Kolliphor EL (Sigma- Aldrich). This dye-containing solution was then vortexed to ensure proper mixing. Meanwhile, brain slices were placed in to 2ml of aCSF before pipetting the dye-DMSO solution onto the surface of the slices, taking care to aim for the cortex as this was the area with Chronos-expressing neurons. The loaded slices were then incubated at 37 °C for 40min whilst oxygenated by 95%/5% O2/CO2 gas blowing onto the surface of the solution. This effectively oxygenates the slice without bubble formation in the solution. Finally, the dye-loaded slices were removed and put back into a dye-free aCSF, for a resting period of 20 min before photostimulation and imaging experiments.

6.3.5 BRAIN SLICE PHOTOSTIMULATION AND ACTIVITY READ OUT

Acute brain slices that both expressed Chronos and were successfully stained with CaSiR-1 were placed under the microscope system described in section 6.3.2 and submerged in circulating oxygenated aCSF. Layer 2/3 of the cortex was identified and visualised with oblique-contrast infrared imaging. To maximise the signal to noise ratio (S/N) for CaSiR-1 imaging, the camera exposure was set to 10ms, and we increased the red LED intensity to excite fluorescence just below camera saturation in the brightest pixels. To find the subset of cells which were both Chronos-expressing and had taken up CaSiR-1 dye, a 'pinging' light pulse consisting of a 3ms, 1 Hz blue LED pulse with an intensity of 0.063–1.2 $^{\mathrm{mW}}/_{mm^2}$ was flashed on to the brain slice whilst scanning the cortex laterally and axially throughout the FOV and imaging CaSiR-1 fluorescence. Chronos-expressing, CaSiR-1-loaded cells exhibited fluorescence transients time-synced to the blue LED pings. In some cases, the blue light evoked calcium transients were monitored during perfusion of 1 μM tetrodotoxin citrate (TTX, Tocris) in aCSF.

Once Chronos-expressing, CaSiR-loaded cells were identified, we began photostimulation and activity readout trials. Due to the inhomogeneity of the dye loading process, we adjusted the red LED intensity in the range of 0.8–2.26 $^{\mathrm{mW}}/_{mm^2}$ for each FOV to evoke fluorescence that came close to saturating the camera in the brightest pixels at 100 Hz frame rates, corresponding to an exposure time of 10 ms with a rolling shutter and 512 × 512 pixels acquired with 4 × 4 binning. To photostimulate the cells, we reduced the blue LED intensity relative to the pinging signal to find the minimal intensity which still produced calcium responses, which ranged from 0.054 to 1.2 $^{\mathrm{mW}}/_{mm^2}$. We needed to use much higher blue light intensities in slices prepared from younger mice, possibly because the density of Chronos molecules in neurons increased with age. The FOV was then stimulated with three, 3 ms flashes of the blue light, delivered at frequencies of 0.5 Hz, 1 Hz, 2 Hz, 5 Hz, 10 Hz, 15 Hz, and 20 Hz. The red imaging LED was on throughout each trial, and off between trials to avoid excess CaSiR-1 photobleaching. We began the trials at the lower stimulation frequencies and continued to higher frequencies if the cell(s) remained responsive. Finally, for each imaging trial, we interleaved a trial in which the red LED was off whilst deploying blue light onto the brain slice. This was to monitor for imaging artefacts caused by bleed through of the blue light on to the camera, or activation of the CaSiR-1 with the blue photostimulation light. We used these 'blue- only' trials to quantify and subtract such artefacts from our imaging data. We calculated $\Delta F/_F$ using the following formula:

$$\frac{\Delta F}{F} = \frac{F - F_0}{F_0 - F_{dark}} \tag{EQUATION 6-1}$$

Where F was the raw fluorescent signal (in counts), F_0 was the baseline fluorescence taken as the average fluorescence in the epoch preceding photostimulation (counts), and F_{dark} was the signal from the camera in the dark (counts).

The signals were extracted from the imaging trials by manually selecting a ROI over the cell of interest using Image-J. Further analysis was performed in custom written Python code. The signals contained flat averages and remained consistent across analysis of the same cell. To quantify what portion of the ROI peak signal was contributed from surrounding cells, or 'background', we subtracted the average signal from a donut shaped ROI surrounding each cellular ROI. Trials in which and after which the peak cellular ROI signal was equal to background, indicating that the cell was no longer responding, had died, or was bleached, were excluded from cellular response statistics.

6.3.6 SCHEMATICS OF EXPRESSION STRATEGIES AND TIMINGS

The general workflow and timings depicting CHO cell culture, transfection, and experimentation is shown in Figure 6-2. After successful culture, cells are transfected with FCK-Chronos-GFP. 24 hours after transfection, I checked for GFP signal to verify Chronos expression, before experimenting on the CHO cells 24 – 48 hours after transfection.

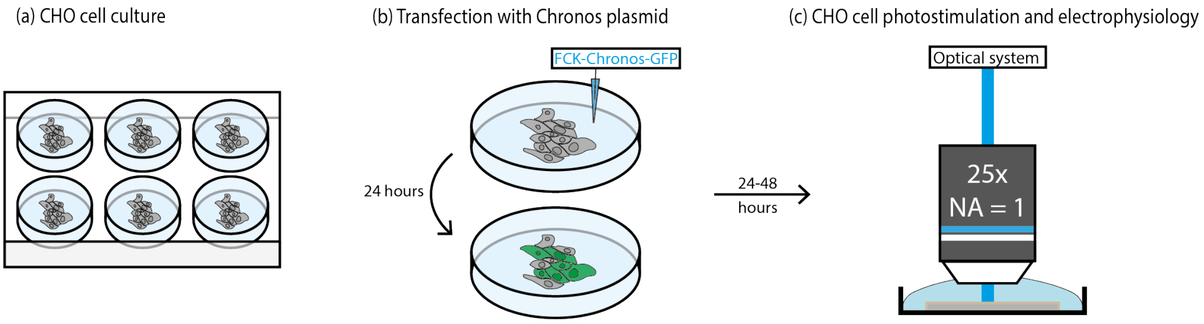

Figure 6-2 Schematic showing CHO cell culture, transfection, and experimentation timelines. ***a*** *After successful culture, cells are transfected with FCK-Chronos-GFP.* ***b*** *24 hours after transfection, I checked for GFP signal to verify Chronos expression, before* ***c*** *experimenting on the CHO cells 24 – 48 hours after transfection.*

6.4 RESULTS

The results of this chapter can be split in to two sections: the first demonstrates that illuminating Chronos expressing CHO cells using red light suitable for CaSiR-1 imaging does not evoke photocurrents in voltage clamped (VC) CHO cells. The second half of the results demonstrate the all-optical neurophysiology approach in acute brain slices, free from optical crosstalk.

6.4.1 WAVELENGTHS SUITABLE FOR CASIR-1 IMAGING DO NOT ACTUATE CHRONOS MEDIATED PHOTOCURRENTS

We measured transmembrane currents in Chronos-transfected CHO cells with whole cell voltage clamp in response to 5 ms red and blue light pulses The results are shown in Figure 6-3. Blue light pulses ranging from 1.1 to 11.3 $^{\mathrm{mW}}/_{mm^2}$ evoked photocurrents which increased with increasing intensity (Figures 6-3 b and d).

The rate of increase in photocurrents decreased with increasing intensity with opsin saturation. Red light pulses, however, evoked no measurable photocurrents (Figures 6-3 c and d), across all measured intensities from 1.1 to 7.8 $^{\mathrm{mW}}/_{mm^2}$. The intensity ranges tested for both blue and red sources exceeded the intensities needed to stimulate and image neuronal activity (Figures 6-3 d) in the following section by several fold. As crosstalk would only increase with intensity, this indicates that imaging with the red light in the subsequent all- optical stimulation and readout of Chronos-expressing brain slices would evoke no spurious photocurrents.

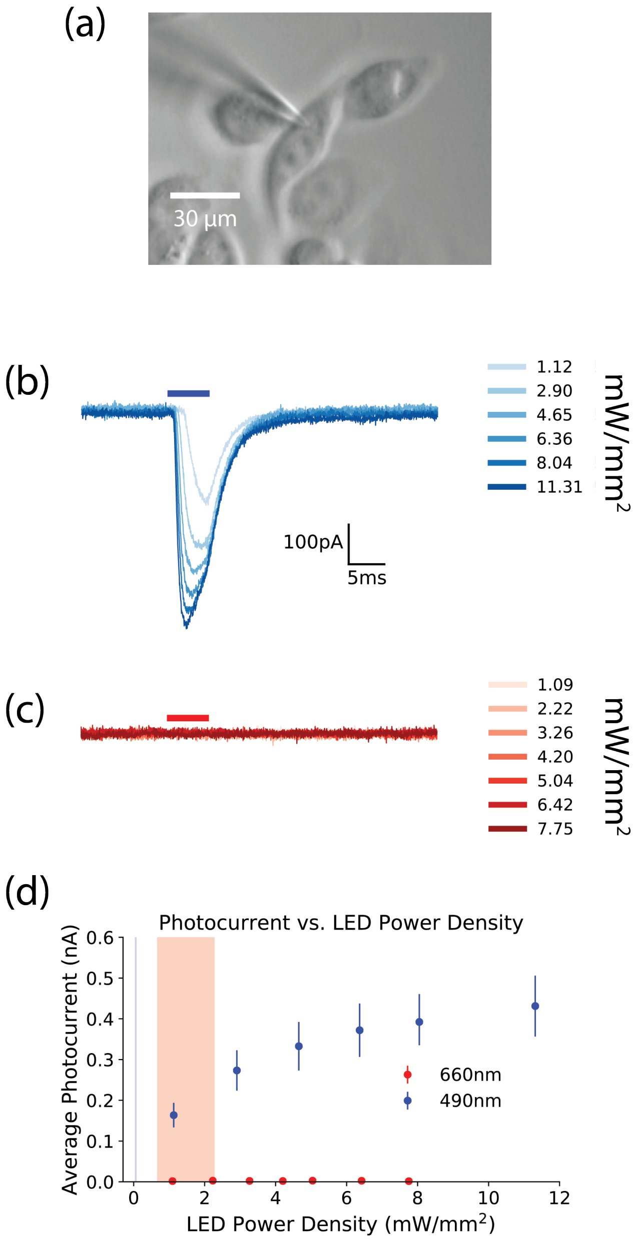

Figure 6-3 Wavelengths suitable for CaSiR-1 imaging do not evoke Chronos-mediated photocurrents. *Blue light pulses evoke photocurrents in Chronos expressing Chinese Hamster Ovary (CHO) cells, but not red light suitable for CaSiR-1 imaging.* ***a*** *Whole cell, voltage clamp recordings of a Chronos-expressing CHO cell when stimulated with* ***b****, blue light and* ***c****, red light- both at increasing illumination power densities. The horizontal blue and red lines above the voltage-clamp traces represent 5 ms long red and blue LED pulses on the targeted patched cell respectively.* ***d*** *The average induced photocurrent of Chronos-expressing cells increased with the blue LED power density but remained zero with increased red LED power density. The graph shows the average currents measured in n = 4 cells, across 16 trials for blue light, and 13 trials for red light. Vertical lines represent the standard error of the mean (S.E.M); S.E.M values for the red-light data series are too small to be seen on this scale. The blue shaded area represents the power densities used to photostimulate Chronos-expressing brain slices; the red shaded area represents the range of power densities used to image CaSiR-1 fluorescence in the brain slice preparations.*

6.4.2 CROSSTALK-FREE READOUT OF CHRONOS-EXPRESSING NEURONS WITH CASIR-1

After determining that illuminating Chronos-expressing CHO cells with red light suitable for CaSiR-1 imaging did not evoke any photocurrents, we demonstrated crosstalk-free functional imaging of Chronos-expressing neurons in acute brain slices. These results are shown in Figure 6-4.

At 100 Hz frame rates, we resolved in single trials calcium transients evoked by 3ms blue light pulses (0.054–1.24 $^{\mathrm{mW}}/_{mm^2}$, shown in Figure 6-3) from five cells in two mice. Calcium transients from these cells could be imaged for between 3 and 90 blue stimulations. We repeated the blue light pulse photostimulation at frequencies ranging from 0.5 to 20 Hz. Even at the highest frequencies, we were able to resolve calcium responses from each individual LED pulse of the trial (Figure 6-3 **b**). We were able to record transients in response to stimulation for up to 50 min in one cell. In 28 trials of 3 blue light stimulations each across five cells in two mice, the peak signal after spatial averaging over 113–227 pixels had a median of 1.56% $^{\Delta F}/_{F}$, with 90th and 10th percentiles of 1.17% and 2.88%. The median noise level was 0.07%, with 90th and 10th percentiles of 0.09% and 0.06%. The median baseline photon flux was 11 461 200 photons pixel^{-1} s^{-1}, with 90th and 10th percentiles of 11772706 and 11163807 photons pixel^{-1} s^{-1} (pixel size 1.04 μm). The median S/N was 22.4, with 90th and 10th percentiles of 43.0 and 14.6. The cellular ROIs bleached an average of 0.036% s^{-1}. $^{\Delta F}/_{F}$, with 90th and 10th percentiles of −0.011% and −0.069% s^{-1}. The peak signal from a donut shaped ROI, or 'background', surrounding the cell after spatially averaging over 1075–1810 pixels had a median of 0.92% $^{\Delta F}/_{F}$, with 90th and 10th percentiles of 1.49% and 0.68%. The background signal was subtracted from that of the cell ROI to give the background subtracted peak response with median of 0.71% $^{\Delta F}/_{F}$, with 90th and 10th percentiles of 1.46% and 0.14%. In this widefield imaging configuration, over half of the median cellular ROI peak signal was contributed by surrounding cells.

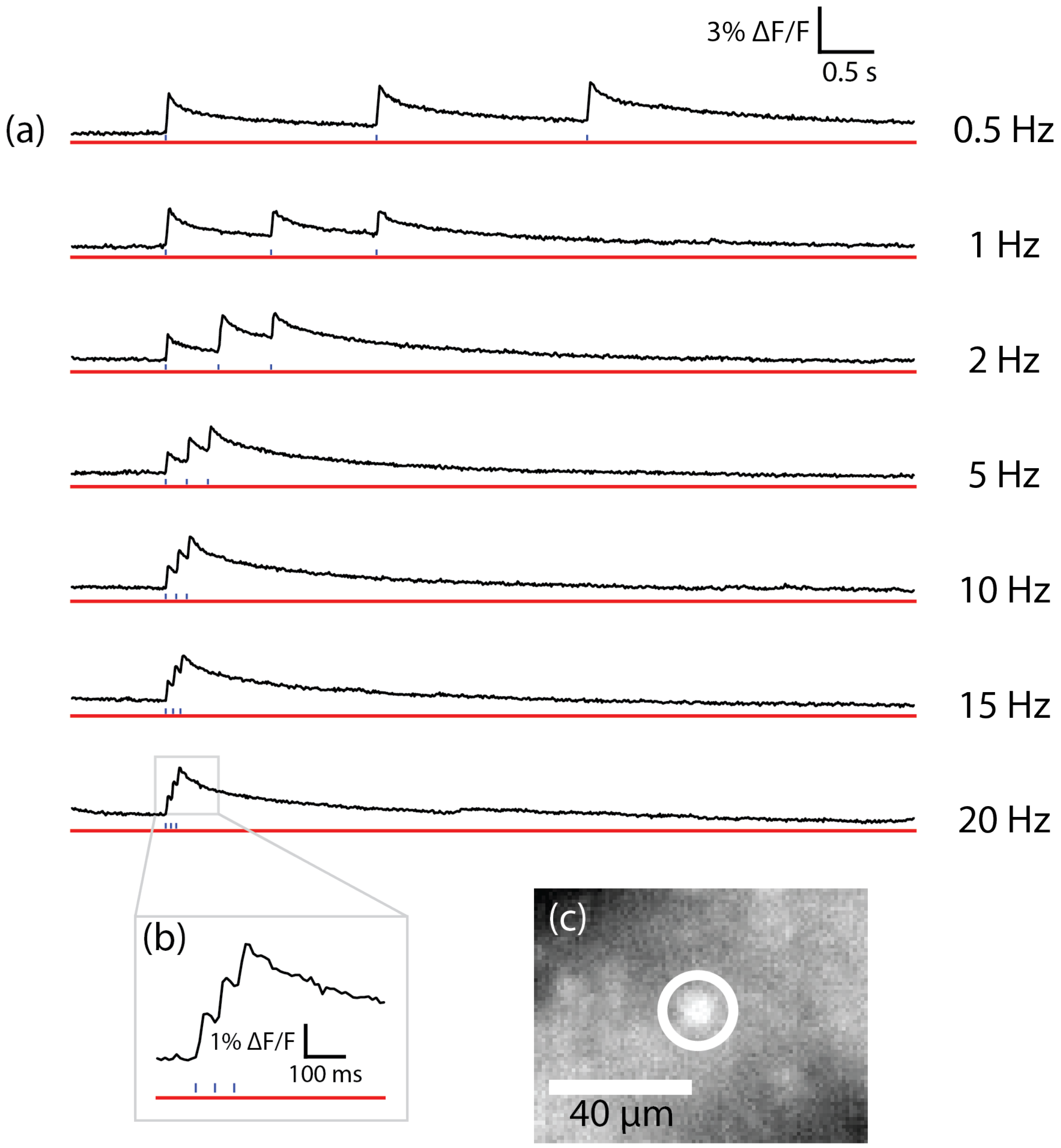

***Figure 6-4 Crosstalk free all-optical neurophysiology**. By staining Chronos-expressing brain slices with the deep-red calcium reporter CaSiR-1, we were able to optically image neuronal activity stimulated up to 20 Hz without crosstalk at 100 frames s−1. **a** A set of CaSiR-1 fluorescence imaging traces recorded from a single cell **c** in single trials. The horizontal red lines represent imaging epochs during which the red LED illumination power density was 1.85 $^{mW}/_{mm^2}$. Vertical blue lines indicate the timing of 3 ms blue LED flashes incident on the CaSiR-1 loaded, Chronos-expressing neurons. Each blue light flash had a power density of 0.063 $^{mW}/_{mm^2}$. **b** A zoomed-in window showing the CaSiR-1 imaging trial whilst photostimulating the brain slice with blue light at 20 Hz. We observed distinct calcium responses for each blue LED light flash. Imaging data were acquired at 100 Hz frame rates. Video of the calcium response is included in the supplementary information. **c** An image showing the cell and ROI (white circle) over which the traces in **a** were averaged. The frame was taken at the peak of fluorescence response of the cell following a blue light flash.*

The slow decay of evoked calcium transients results from a combination of the time for calcium to return to baseline concentrations following an action potential and CaSiR-1 dissociation kinetics. It is important to note that the electrical action potentials causing these calcium rises are brief, lasting ~1 ms. In addition, each blue light pulse may have evoked one or more action potentials, each contributing to the measured calcium transient peak. Bath application of 1 μM TTX reduced the slowly decaying blue light evoked calcium transients after 15 min to brief, small transients, <5% of the peak pre-TTX transient amplitude and lasting only as long as the 3ms blue light pulses. These small residual transients, which were not caused by action potentials, could potentially reflect calcium conductance directly through Chronos channels and/ or low voltage activated calcium channels.

To quantify crosstalk or bleed-through caused by the blue photostimulation light, we acquired trials in which blue light was pulsed onto the sample in the absence of red light, called 'blue only' trials. This crosstalk does not affect cell physiology and appears as increased image counts during blue light on periods. As the stimulation period is known, the artefact can be simply subtracted. Averaged over the entire FOV, these 'blue only' trials revealed artefacts with a median pixel count of 1.7 digital number (DN), with 90th and 10th percentiles of 115 and 0.94 across 105 trials. The cells in the younger mouse required approximately 10 times higher stimulation intensities compared to the older mice, resulting in larger stimulus artefacts. The artefacts in the old mouse corresponded to 3.8% of the average baseline noise (standard deviation) of trials during which the red light was on, and 0.2% of the average peak calcium transient amplitude. In the young mice, the artefacts were around 4 times larger than the RMS noise level of the fluorescent traces. Due to the sCMOS rolling shutter, these artefacts may be underestimated by, at most, a factor of two due to the blue light pulse spanning two adjacent frames. Even if multiplied by two, these artefacts were small relative to the measured calcium transients.

We recorded non-Chronos evoked calcium transients from many cells at a variety of depths. We measured the depths of a subset of active cells (n = 14), and the median was 47.5 μm, with 90th and 10th percentiles of 66.5 and 33.5 μm. We did not record from FOV with multiple blue light-responding cells; however, we did record from areas with up to 30 active cells.

6.5 DISCUSSION

For the discussion of this chapter, I reflect on the chapter aims before relating this work to optical functional connectivity mapping. For a more in-depth discussion on this work with reference to optical crosstalk, I invite the reader to see the discussion section of the manuscript that this chapter is based on [57].

6.5.1 REFLECTION ON CHAPTER AIMS

We designed an optical system capable of all-optical, crosstalk-free neurophysiology

With reference to Figure 6-2, we designed and validated a microscope capable of all-optical, crosstalk-free neurophysiology. By taking in to account the action spectrum and excitation/emission spectrum of Chronos and CaSiR-1 respectively, we strategically selected our filter sets and LEDs to be able to combine the photostimulation and activity reporter light paths.

Red light suitable for CaSiR-1 imaging does note evoke Chronos mediated photocurrents

By transfecting CHO cells with Chronos and illuminating them with red wavelengths used to excite CaSiR-1- at power densities greater than three-fold higher than those needed to image its fluorescence in stained brain slices at 100 frames/s- we observed no evoked photocurrents in voltage-clamped Chronos-expressing CHO cells. This indicates that the red light used to excite CaSiR-1 in brain slices most likely did not evoke spurious Chronos-mediated depolarisations, sub- or supra-threshold. This crosstalk-free readout is made possible by the spectral separation of the Chronos action spectrum from the CaSiR-1 absorption spectrum, which is larger than previously reported pairings of opsins and calcium reporters. Although not shown here, CaSiR-1 could also be used for crosstalk-free one-photon imaging of ChR2 transfected neurons, as ChR2's action spectrum is bluer than Chronos'.

We demonstrate all-optical, crosstalk-free neurophysiology in acute brain slices

By staining triple-transgenic brain slices expressing Chronos in layer 2/3 cortical neurons, we then demonstrate crosstalk-free, high signal- to-noise ratio calcium activity reporting of CaSiR-1 red fluorescence at 100 frames s^{-1}. The Chronos-mediated calcium transients were evoked in neurons with blue light pulses at rates up to 20 Hz. Crucially, this validated our approach to all-optical neurophysiology in acute brain slices.

6.5.2 FUTURE DIRECTIONS IN THE LIGHT OF FUNCTIONAL CONNECTIVITY MAPPING

All-optical neurophysiology has much to offer functional mapping paradigms. Here, I demonstrated a crosstalk-free methodology for all-optical neurophysiology but there are many directions one could take this work when considering functional mapping. First let's revisit some of the limitations of the mapping protocol used in Chapter 5:

1) No verification of putative pre-synaptic activity upon single neuron precision photostimulation- be it spiking or subthreshold depolarisations.
2) It was a many-to-one mapping paradigm, which doesn't consider bidirectional functional connectivity or many-to-many functional connections.
3) Without reliable GFP signal to indicate opsin expression, patching was essentially 'blind'.
4) Mechanical disruption tissue preparations when patch clamping.

All optical strategies have the potential of mitigating all of these:

1) Expressing or staining our tissue preparations with a red calcium or voltage reporter could provide response feedback from pre-synaptic neurons upon photostimulation[123]. The light patterning microscope used for the functional connectivity assays in Chapter 5 already incorporates a red LED into its light path (as described in section 4.2.2). Hence, it would be possible on the engineering front to switch to an all-optical approach avoiding optical crosstalk (though we would need to run a spectroscopic analysis on the Red LED and devise a new filter set for red fluorescent imaging). However, we would not necessarily need to construct a crosstalk-free paradigm. Printz et al.[123] showed that by pairing stCoChR and GCaMP6s which have overlapping action and excitation spectra, one could get a 'free' readout of calcium activity when photostimulating presynaptic neurons- effectively providing a validation of spiking activity. Relating back to our connectivity experiments, we could in principle transfect IT neurons with an activity reporter using the same methodology used for ChR2-GFP expression (Section 2.2.2) hence expressing both ChR2-GFP and an optical reporter of activity- thus opening the door to all-optical connectivity mapping.

2) With larger subsets of neurons reporting their activity via an optical reporter- be it calcium or voltage imaging, one could monitor the fluorescence profile of all neurons within the field of view and correlate this activity with any single neuron precision functional mapping paradigm. This would move the experiment to a many-to-many approach- significantly increasing the efficiency and data yield of functional mapping paradigms.

3) Genetic targeting of an activity reporter, either via a transgenic mouse line or viral injection could provide cell-class information for pre-synaptic neurons. Hence, one could gain a more detailed picture of the functional architectures including IT neurons. How, for instance, are interneurons functionally wired to IT neurons? Practically speaking, one could utilise the same expression strategy we used in

Section 2.2.2 for the IT neurons, but instead of using C57BL/6 mouse line, we could use a transgenic mouse expressing an activity reporter in a specific subset of neurons.

4) All-optical approaches, though fraught with their own difficulties (difficulties in expression methodologies, expression variability, cell health due to ectopic expression of opsins or activity reporters), offer a relatively simple experimental protocol when the slice is actually under the microscope; there is minimal mechanical disruption to tissue without having to patch, and the reality of patching is that it can be riddled with various practical or technical difficulties.

5) To play devil's advocate, a large roadblock I faced for the functional mapping experiments in Chapter 5 was expression variability and cell health. In the interest of not being too much of an all-optical evangelist, I would be remiss if I didn't note in this discussion how all-optical approaches could have these same issues- if not worse. Though the experimental protocol would be relatively more pleasant when the slice is under the objective, getting a healthy, doubly transgenic, or synthetically labelled slice into the recording chamber in the first place would not be straight forward- and likely require a lot of refining and frankly, failure, before it paid off. In a similar vein, optical activity reporting still falls short of patch clamping in a few regards; calcium imaging, while allowing the inference of APs, doesn't necessarily discern single spikes and furthermore filters any subthreshold activity from its signal. Conversely, voltage imaging can retain these sub-threshold activity signals, but are themselves difficult to work with- they are localised on the cell membrane, meaning discerning signal from two neighbouring neurons presents a significant challenge. They also generally have lower signal to noise and are detrimental to cell health- but one can remain hopeful when considering the rapid progress the field is making[66].

CHAPTER 7

CLOSING REMARKS

"To see a World in a Grain of Sand
And a Heaven in a Wild Flower
Hold Infinity in the palm of your hand
And Eternity in an Hour…"
-*William Blake,* Auguries of Innocence

This PhD sought to develop tools to optically map the local functional connectivity of neuronal microcircuits. In the first results chapter I show that in the set of neurons tested, intrinsic conductance and synaptic drive could have an effect on a neuron's Action Potential waveform- which itself can have an effect on functional connectivity assays and downstream information processing in the brain.

In the second results chapter, I develop, characterise, and validate a light patterning system to optically map the local functional connectivity of Inter Telencephalic neurons in the Prefrontal Cortex, concluding that such an experimental goal is possible with our system albeit with a few limitations; results chapter 3 then goes on to attempt these experiments, showing that it is possible- but rather tricky. In the final results chapter, I demonstrate a novel approach to all-optical neurophysiology which is free from optical crosstalk. Indeed, it would be very possible to adapt such an approach for functional connectivity assays in the future.

And finally, I return to Dyson's bird[1]: ascending above the landscape, surveying it with a new set of eyes.

BIBLIOGRAPHY.

1. Dyson, F. J. Birds and frogs in mathematics and physics. *Physics-Uspekhi* **53**, 825–834 (2010).
2. Harris, K. D. & Mrsic-Flogel, T. D. Cortical connectivity and sensory coding. *Nature* **503**, 51–58 (2013).
3. Verkhratsky, A. & Parpura, V. *History of electrophysiology and the patch clamp*. *Methods in Molecular Biology* **1183**, (2014).
4. Denk, W., Briggman, K. L. & Helmstaedter, M. Structural neurobiology: missing link to a mechanistic understanding of neural computation. *Nat. Rev. Neurosci.* (2012). doi:10.1038/nrn3169
5. Swanson, L. W. & Lichtman, J. W. From Cajal to Connectome and beyond. *Annu. Rev. Neurosci.* **39**, 197–216 (2016).
6. Kim, J. *et al.* MGRASP enables mapping mammalian synaptic connectivity with light microscopy. *Nat. Methods* **9**, 96–102 (2012).
7. Helmchen, F. & Denk, W. Deep tissue two-photon microscopy. *Nat. Methods* **2**, 932–940 (2005).
8. Ginger, M., Haberl, M., Conzelmann, K. K., Schwarz, M. K. & Frick, A. Revealing the secrets of neuronal circuits with recombinant rabies virus technology. *Front. Neural Circuits* **7**, 1–15 (2013).
9. Tervo, D. G. R. *et al.* A Designer AAV Variant Permits Efficient Retrograde Access to Projection Neurons. *Neuron* **92**, 372–382 (2016).
10. Poulopoulos, A. *Synapse Development*. *Methods in Molecular Biology* **1538**, (2017).
11. Trachtenberg, J. T. *et al.* Long-term in vivo imaging of experience-dependent synaptic plasticity in adult cortex. *Nature* **420**, 788–794 (2002).
12. Abbott, L. F. & Nelson, S. B. Synaptic plasticity: Taming the beast. *Nat. Neurosci.* **3**, 1178–1183 (2000).
13. Debanne, D. & Poo, M. M. Spike-timing dependent plasticity beyond synapse - pre- and post-synaptic plasticity of intrinsic neuronal excitability. *Front. Synaptic Neurosci.* **2**, 1–6 (2010).
14. Feldman, D. E. The Spike-Timing Dependence of Plasticity. *Neuron* **75**, 556–571 (2012).

15. González-Rueda, A., Pedrosa, V., Feord, R. C., Clopath, C. & Paulsen, O. Activity-Dependent Downscaling of Subthreshold Synaptic Inputs during Slow-Wave-Sleep-like Activity In Vivo. *Neuron* **97**, 1244-1252.e5 (2018).

16. Tye, K. M. & Deisseroth, K. Optogenetic investigation of neural circuits underlying brain disease in animal models. *Nat. Rev. Neurosci.* **13**, 251–266 (2012).

17. Sanchez-Mut, J. V. & Gräff, J. Epigenetic Alterations in Alzheimer's Disease. *Front. Behav. Neurosci.* **9**, 1–17 (2015).

18. Fornito, A., Zalesky, A. & Breakspear, M. The connectomics of brain disorders. *Nat. Rev. Neurosci.* **16**, 159–172 (2015).

19. Matsuzaki, M. *et al.* Dendritic spine geometry is critical for AMPA receptor expression in hippocampal CA1 pyramidal neurons. *Nat. Neurosci.* **4**, 1086–92 (2001).

20. Grover, V. P. B. *et al.* Magnetic Resonance Imaging: Principles and Techniques: Lessons for Clinicians. *J. Clin. Exp. Hepatol.* **5**, 246–255 (2015).

21. O'Donnell, L. J. & Westin, C.-F. An Introduction to Diffusion Tensor Image Analysis. *Neurosurg. Clin. N. Am.* **22**, 185–196 (2011).

22. Al-Sharify, Z. T., Al-Sharify, T. A., Al-Sharify, N. T. & Naser, H. Y. A critical review on medical imaging techniques (CT and PET scans) in the medical field. *IOP Conf. Ser. Mater. Sci. Eng.* **870**, (2020).

23. Glover, G. H. Overview of functional magnetic resonance imaging. *Neurosurg. Clin. N. Am.* **22**, 133–139 (2011).

24. Vaquero, J. J. & Kinahan, P. Positron Emission Tomography: Current Challenges and Opportunities for Technological Advances in Clinical and Preclinical Imaging Systems. *Annu. Rev. Biomed. Eng.* **17**, 385–414 (2015).

25. Cabeza, R., Anderson, N. D., Locantore, J. K. & McIntosh, A. R. Aging gracefully: Compensatory brain activity in high-performing older adults. *Neuroimage* **17**, 1394–1402 (2002).

26. Cabeza, R. *et al.* Maintenance, reserve and compensation: the cognitive neuroscience of healthy ageing. *Nat. Rev. Neurosci.* **19**, 701–710 (2018).

27. Drysdale, A. T. *et al.* Resting-state connectivity biomarkers define neurophysiological subtypes of depression. *Nat. Publ. Gr.* **23**, (2016).

28. Bassett, D. S. & Bullmore, E. T. Human brain networks in health and disease. *Curr. Opin.*

Neurol. **22**, 340–347 (2009).

29. Sjöström, P. J. & Häusser, M. A Cooperative Switch Determines the Sign of Synaptic Plasticity in Distal Dendrites of Neocortical Pyramidal Neurons. *Neuron* **51**, 227–238 (2006).

30. Song, S., Sjöström, P. J., Reigl, M., Nelson, S. & Chklovskii, D. B. Highly nonrandom features of synaptic connectivity in local cortical circuits. *PLoS Biol.* **3**, 0507–0519 (2005).

31. Perin, R., Berger, T. K. & Markram, H. A synaptic organizing principle for cortical neuronal groups. *Proc. Natl. Acad. Sci.* **108**, 5419–5424 (2011).

32. Thomson, A. M. & Lamy, C. Functional Maps of Neocortical Local Circuitry. *Front. Neurosci.* **1**, 19–42 (2007).

33. Harris, K. D. & Shepherd, G. M. G. The neocortical circuit: Themes and variations. *Nat. Neurosci.* **18**, 170–181 (2015).

34. Yoshimura, Y. & Callaway, E. M. Fine-scale specificity of cortical networks depends on inhibitory cell type and connectivity. *Nat. Neurosci.* **8**, 1552–1559 (2005).

35. Jiang, X., Wang, G., Lee, A. J., Stornetta, R. L. & Zhu, J. J. The organization of two new cortical interneuronal circuits. *Nat. Neurosci.* **16**, 210–218 (2013).

36. Jiang, X. *et al.* Principles of connectivity among morphologically defined cell types in adult neocortex. *Science (80-.).* **350**, (2015).

37. Ko, H. *et al.* The emergence of functional microcircuits in visual cortex. *Nature* **496**, 96–100 (2013).

38. Ko, H. *et al.* Functional specificity of local synaptic connections in neocortical networks. *Nature* **473**, 87–91 (2011).

39. Kim, T., Oh, W. C., Choi, J. H. & Kwon, H.-B. Emergence of functional subnetworks in layer 2/3 cortex induced by sequential spikes in vivo. *Proc. Natl. Acad. Sci.* 201513410 (2016). doi:10.1073/pnas.1513410113

40. Brown, S. P. & Hestrin, S. Intracortical circuits of pyramidal neurons reflect their long-range axonal targets. *Nature* **457**, 1133–1136 (2009).

41. Kim, M. H., Znamenskiy, P., Iacaruso, M. F. & Mrsic-Flogel, T. D. Segregated Subnetworks of Intracortical Projection Neurons in Primary Visual Cortex. *Neuron* **100**, 1313-1321.e6 (2018).

42. Kampa, B. M., Letzkus, J. J. & Stuart, G. J. Cortical feed-forward networks for binding

different streams of sensory information. *Nat. Neurosci.* **9**, 1472–1473 (2006).

43. Shulz, D. E. & Jacob, V. Spike-timing-dependent plasticity in the intact brain : counteracting spurious spike coincidences. **2**, 1–10 (2010).

44. Pawlak, V., Greenberg, D. S., Sprekeler, H., Gerstner, W. & Kerr, J. N. D. Changing the responses of cortical neurons from sub- To suprathreshold using single spikes in vivo. *Elife* **2013**, 1–18 (2013).

45. Yizhar, O., Fenno, L. E., Davidson, T. J., Mogri, M. & Deisseroth, K. Optogenetics in Neural Systems. *Neuron* **71**, 9–34 (2011).

46. Deisseroth, K. Optogenetics. *Nat. Methods* **8**, 26–29 (2011).

47. Emiliani, V., Cohen, A. E., Deisseroth, K. & Ha, M. All-Optical Interrogation of Neural Circuits. **35**, 13917–13926 (2015).

48. Abdelfattah, A. *et al.* Neurophotonic Tools for Microscopic Measurements and Manipulation: Status Report. *Neurophotonics* **9**, 1–86 (2022).

49. Boyden, E. S., Zhang, F., Bamberg, E., Nagel, G. & Deisseroth, K. Millisecond-timescale, genetically targeted optical control of neural activity. *Nat. Neurosci.* **8**, 1263–1268 (2005).

50. Klapoetke, N. C. *et al.* Independent optical excitation of distinct neural populations. *Nat. Methods* **11**, 338–46 (2014).

51. Chuong, A. S. *et al.* Noninvasive optical inhibition with a red-shifted microbial rhodopsin. *Nat. Neurosci.* **17**, 1123–1129 (2014).

52. Tada, M., Takeuchi, A., Hashizume, M., Kitamura, K. & Kano, M. A highly sensitive fluorescent indicator dye for calcium imaging of neural activity in vitro and in vivo. **39**, 1720–1728 (2014).

53. Knöpfel, T. Genetically encoded optical indicators for the analysis of neuronal circuits. *Nat. Rev. Neurosci.* **13**, (2012).

54. Madisen, L. *et al.* Transgenic mice for intersectional targeting of neural sensors and effectors with high specificity and performance. *Neuron* **85**, 942–958 (2015).

55. Akerboom, J. *et al.* Optimization of a GCaMP Calcium Indicator for Neural Activity Imaging. *J. Neurosci.* **32**, 13819–13840 (2012).

56. Akerboom, J. *et al.* Genetically encoded calcium indicators for multi-color neural activity imaging and combination with optogenetics. *Front. Mol. Neurosci.* **6**, 1–29 (2013).

57. Soor, N. S. *et al.* All-Optical Crosstalk-Free Manipulation and Readout of Chronos-

expressing Neurons. *J. Phys. D. Appl. Phys.* (2018). doi:10.1088/1361-6463/aaf944

58. Nagel, G. *et al.* Channelrhodopsin-2, a directly light-gated cation-selective membrane channel. *Proc. Natl. Acad. Sci.* **100**, 13940–13945 (2003).

59. Berndt, A., Yizhar, O., Gunaydin, L. A., Hegemann, P. & Deisseroth, K. Bi-stable neural state switches. *Nat. Neurosci.* **12**, 229–234 (2009).

60. Erbguth, K., Prigge, M., Schneider, F., Hegemann, P. & Gottschalk, A. Bimodal Activation of Different Neuron Classes with the Spectrally Red-Shifted Channelrhodopsin Chimera C1V1 in Caenorhabditis elegans. *PLoS One* **7**, (2012).

61. Lin, J. Y., Knutsen, P. M., Muller, A., Kleinfeld, D. & Tsien, R. Y. ReaChR: a red-shifted variant of channelrhodopsin enables deep transcranial optogenetic excitation. *Nat. Neurosci.* **16**, 1499–1508 (2013).

62. Shemesh, O. A. *et al.* Temporally precise single-cell-resolution optogenetics. *Nat. Neurosci.* **20**, 1796–1806 (2017).

63. Mattis, J. *et al.* Principles for applying optogenetic tools derived from direct comparative analysis of microbial opsins. *Nat. Methods* **9**, 159–172 (2011).

64. Kishi, K. E. *et al.* Structural basis for channel conduction in the pump-like channelrhodopsin ChRmine. *Cell* **185**, 672-689.e23 (2022).

65. Piatkevich, K. D. *et al.* A robotic multidimensional directed evolution approach applied to fluorescent voltage reporters. *Nat. Chem. Biol.* **14**, 1 (2018).

66. Piatkevich, K. D. *et al.* Population imaging of neural activity in awake behaving mice. *Nature* **574**, 413–417 (2019).

67. Abdelfattah, A. S. *et al.* BrighAbdelfattah, A. S. et al. (2018) 'Bright and photostablAbdelfattah, A. S. et al. (2018) 'Bright and photostable chemigenetic indicators for extended in vivo voltage imaging'. doi: 10.1101/436840.e chemigenetic indicators for extended in vivo voltage . (2018). doi:10.1101/436840

68. Oron, D., Papagiakoumou, E., Anselmi, F. & Emiliani, V. *Two-photon optogenetics. Progress in Brain Research* **196**, (Elsevier B.V., 2012).

69. Ronzitti, E. *et al.* Recent advances in patterned photostimulation for optogenetics. *J. Opt. (United Kingdom)* **19**, 113001 (2017).

70. Chen, I.-W., Papagiakoumou, E. & Emiliani, V. Towards circuit optogenetics. *Curr. Opin. Neurobiol.* **50**, 179–189 (2018).

71. Oheim, M., Beaurepaire, E., Chaigneau, E., Mertz, J. & Charpak, S. Two-photon microscopy in brain tissue: Parameters influencing the imaging depth. *J. Neurosci. Methods* **111**, 29–37 (2001).

72. Göppert-Mayer, M. Elementary processes with two quantum transitions. *Ann. der Phys.* **18**, 466–479 (2009).

73. Szabo, V., Ventalon, C., DeSars, V., Bradley, J. & Emiliani, V. Spatially selective holographic photoactivation and functional fluorescence imaging in freely behaving mice with a fiberscope. *Neuron* **84**, 1157–1169 (2014).

74. Grossman, N. *et al.* Multi-site optical excitation using ChR2 and micro-LED array. *J. Neural Eng.* **7**, 016004 (2010).

75. Glückstad, J. Phase contrast image synthesis. *Opt. Commun.* **130**, 225–230 (1996).

76. Palima, D. & Glückstad, J. Comparison of generalized phase contrast and computer generated holography for laser image projection. *Opt. Express* **16**, 5338–5349 (2008).

77. Gerchberg, B. R. W. & Saxton, W. O. A Practical Algorithm for the Determination of Phase from Image and Diffraction Plane Pictures. **35**, (1972).

78. Goodman, J. W. *Introduction to Fourier Optics, Third Edition*. *Optical Engineering* (2005). doi:10.1117/1.601121

79. Papagiakoumou, E. *et al.* Scanless two-photon excitation of channelrhodopsin-2. *Nat. Methods* **7**, 848–854 (2010).

80. Oron, D. & Silberberg, Y. Temporal focusing microscopy. *Cold Spring Harb. Protoc.* **2015**, 145–151 (2015).

81. Bègue, A. *et al.* Two-photon excitation in scattering media by spatiotemporally shaped beams and their application in optogenetic stimulation. *Biomed. Opt. Express* **4**, 2869 (2013).

82. Conti, R., Assayag, O., Sars, V. De, Guillon, M. & Emiliani, V. Computer Generated Holography with Intensity-Graded Patterns. **10**, 1–11 (2016).

83. Hernandez, O. *et al.* Three-dimensional spatiotemporal focusing of holographic patterns. *Nat. Commun.* **7**, 11928 (2016).

84. Sun, B. *et al.* Four-dimensional light shaping: Manipulating ultrafast spatiotemporal foci in space and time. *Light Sci. Appl.* **7**, 1–14 (2018).

85. Pégard, N. C. *et al.* Three-dimensional scanless holographic optogenetics with temporal

focusing (3D-SHOT). *Nat. Commun.* **8**, 1–14 (2017).

86. Mardinly, A. R. *et al.* 3D All-optical Control of Functionally Defined Neurons With Cellular Resolution and Sub-millisecond Precision. *Opt. Life Sci. Congr.* **2017**, BrM3B.4 (2017).

87. Bañas, A. & Glückstad, J. Holo-GPC: Holographic Generalized Phase Contrast. *Opt. Commun.* **392**, 190–195 (2017).

88. Accanto, N. *et al.* Multiplexed temporally focused light shaping for high-resolution multi-cell targeting. **in prepara**, 6–13 (2018).

89. Yang, W., Carrillo-reid, L., Bando, Y., Peterka, D. S. & Yuste, R. Simultaneous Two-photon Optogenetics and Imaging of Cortical Circuits in Three Dimensions. doi:10.7554/eLife.32671

90. Mardinly, A. R. *et al.* Precise multimodal optical control of neural ensemble activity. *Nat. Neurosci.* **21**, 881–893 (2018).

91. Anastasiades, P. G., Marques-Smith, A. & Butt, S. J. B. Studies of cortical connectivity using optical circuit mapping methods. *J. Physiol.* **596**, 145–162 (2018).

92. Dantzker, J. L. & Callaway, E. M. Laminar sources of synaptic input to cortical inhibitory interneurons and pyramidal neurons. *Nat. Neurosci.* **3**, 701–707 (2000).

93. Yamawaki, N. & Shepherd, G. M. G. Synaptic circuit organization of motor corticothalamic neurons. *J. Neurosci.* **35**, 2293–2307 (2015).

94. Yamawaki, N., Suter, B. A., Wickersham, I. R. & Shepherd, G. M. G. Combining optogenetics and electrophysiology to analyze projection neuron circuits. *Cold Spring Harb. Protoc.* **2016**, 840–847 (2016).

95. Marques-Smith, A. *et al.* A Transient Translaminar GABAergic Interneuron Circuit Connects Thalamocortical Recipient Layers in Neonatal Somatosensory Cortex. *Neuron* **89**, 536–549 (2016).

96. Hooks, B. M. *et al.* Organization of cortical and thalamic input to pyramidal neurons in mouse motor cortex. *J. Neurosci.* **33**, 748–760 (2013).

97. Ting, J. T., Daigle, T. L., Chen, Q. & Feng, G. Patch-Clamp Methods and Protocols. **1183**, 221–242 (2014).

98. Ting, J. T. *et al.* Preparation of Acute Brain Slices Using an Optimized N-Methyl-D-glucamine Protective Recovery Method. *J. Vis. Exp.* 1–13 (2018). doi:10.3791/53825

99. Bean, B. P. The action potential in mammalian central neurons. *Nat. Rev. Neurosci.* **8**, 451–

465 (2007).

100. Guttman, R. & Barnhill, R. Oscillation and repetitive firing in squid axons: Comparison of experiments with computations. *J. Gen. Physiol.* **55**, 104–118 (1970).

101. Korngreen, A., Kaiser, K. M. M. & Zilberter, Y. Subthreshold inactivation of voltage-gated K+ channels modulates action potentials in neocortical bitufted interneurones from rats. *J. Physiol.* **562**, 421–437 (2005).

102. De Polavieja, G. G., Harsch, A., Kleppe, I., Robinson, H. P. C. & Juusola, M. Stimulus history reliably shapes action potential waveforms of cortical neurons. *J. Neurosci.* **25**, 5657–5665 (2005).

103. Henze, D. A. & Buzsáki, G. Action potential threshold of hippocampal pyramidal cells in vivo is increased by recent spiking activity. *Neuroscience* **105**, 121–130 (2001).

104. Wang, L. Y., Fedchyshyn, M. J. & Yang, Y. M. Action potential evoked transmitter release in central synapses: Insights from the developing calyx of Held. *Mol. Brain* **2**, (2009).

105. Borst, J. G. G. & Sakmann, B. Effect of changes in action potential shape on calcium currents and transmitter release in a calyx-type synapse of the rat auditory brainstem. *Philos. Trans. R. Soc. B Biol. Sci.* **354**, 347–355 (1999).

106. Chao, O. Y. & Yang, Y. M. Timing constraints of action potential evoked Ca 2+ current and transmitter release at a central nerve terminal. *Sci. Rep.* **9**, 1–14 (2019).

107. Geiger, J. R. P. & Jonas, P. Dynamic control of presynaptic Ca2+ inflow by fast-inactivating K+ channels in hippocampal mossy fiber boutons. *Neuron* **28**, 927–939 (2000).

108. Augustine, B. Y. G. J. Biological Angeles,. 343–364 (1990).

109. Ishikawa, T. *et al.* Distinct Roles of Kv1 and Kv3 Potassium Channels at the Calyx of Held Presynaptic Terminal. *J. Neurosci.* **23**, 10445–10453 (2003).

110. Sharp, A. A., O'Neil, M. B., Abbott, L. F. & Marder, E. Dynamic clamp: Computer-generated conductances in real neurons. *J. Neurophysiol.* **69**, 992–995 (1993).

111. Prinz, A. A., Abbott, L. F. & Marder, E. The dynamic clamp comes of age. *Trends Neurosci.* **27**, 218–224 (2004).

112. MacKenzie, G., Franks, N. P. & Brickley, S. G. Two-pore domain potassium channels enable action potential generation in the absence of voltage-gated potassium channels. *Pflugers Arch. Eur. J. Physiol.* **467**, 989–999 (2015).

113. Goldman, B. Y. D. E. IN MEMBRANES (From the Department of] Physiology , College of

Physicians and Surgeons , Columbia University , New York). 37–60 (1943).

114. Hodgkin, A. L. & Horowicz, P. The influence of potassium and chloride ions on the membrane potential of single muscle fibres. *J. Physiol.* **148**, 127–160 (1959).

115. Huang, S., Hong, S. & De Schutter, E. Non-linear leak currents affect mammalian neuron physiology. *Front. Cell. Neurosci.* **9**, 1–10 (2015).

116. Edelstein, A. D. *et al.* Advanced methods of microscope control using μManager software. *J. Biol. Methods* **1**, e10 (2014).

117. Schneider, C. A., Rasband, W. S. & Eliceiri, K. W. NIH Image to ImageJ: 25 years of image analysis. *Nat. Methods* **9**, 671–675 (2012).

118. Park, D. C. & Reuter-Lorenz, P. The Adaptive Brain: Aging and Neurocognitive Scaffolding. *Annu. Rev. Psychol.* **60**, 173–196 (2009).

119. Zhang, Z., Russell, L. E., Packer, A. M., Gauld, O. M. & Häusser, M. Closed-loop all-optical interrogation of neural circuits in vivo. *Nat. Methods* **15**, 1037–1040 (2018).

120. Hochbaum, D. R. *et al.* All-optical electrophysiology in mammalian neurons using engineered microbial rhodopsins. *Nat. Methods* **11**, 825–833 (2014).

121. Clopath, C. & Gerstner, W. Voltage and spike timing interact in STDP - a unified model. *Front. Synaptic Neurosci.* **2**, 1–11 (2010).

122. Egawa, T. *et al.* Development of a far-red to near-infrared fluorescence probe for calcium ion and its application to multicolor neuronal imaging. *J. Am. Chem. Soc.* **133**, 14157–14159 (2011).

123. Printz, Y. *et al.* Determinants of functional synaptic connectivity among amygdala-projecting prefrontal cortical neurons. *bioRxiv* (2021).